

# Pair Production in time-dependent Electric field at Finite times

Deepak Sah<sup>\*1,2</sup> and Manoranjan P. Singh<sup>1,2</sup>

<sup>1</sup>*Theoretical and Computational Physics Section, Theory and Simulations Lab,  
Raja Ramanna Centre for Advanced Technology, Indore-452013, India*

<sup>2</sup>*Homi Bhabha National Institute, Training School Complex,  
Anushakti Nagar, Mumbai 400094, India*

(Dated: April 18, 2025)

## Abstract

We investigate the finite-time behavior of pair production from the vacuum by a time-dependent Sauter pulsed electric field. By examining the temporal behavior of the single-particle distribution function, we observe oscillatory patterns in the longitudinal momentum spectrum of the particles at finite times. These oscillations arise due to quantum interference effects resulting from the various dynamical processes/channels leading to the creation of the (quasi-)particle of a given momentum. Furthermore, we derive an approximate and simplified analytical expression for the distribution function at finite times, allowing us to explain these oscillations' origin and behavior. The role of the vacuum polarization function and its counterterm is also discussed in this regard. The transverse momentum spectrum peaked at the nonzero value of the transverse momentum at finite times, which indicates the role of multiphoton transitions in the creation of quasiparticles.

Keywords: Particle Production, Dynamical Schwinger effect, Strong-Field QED

---

\* Corresponding author.

E-mail address: dsah129@gmail.com(Deepak Sah).

## I. INTRODUCTION

The concept of pair production in an electromagnetic field has its roots in the mid-1920s after the invention of quantum mechanics, with the formulation of the relativistic wave equation for electrons by Paul Dirac in 1928 [1]. The Dirac Sea model was proposed to explain the enigma of negative energy solutions. F. Sauter's work in 1931 demonstrated that strong electric fields can lead to pair creation through tunneling with exponential suppression [2]. This paved the way for quantum field theory, recognizing the vacuum as a polarizable medium influenced by constant fluctuations. In 1935, W. Heisenberg and H. Euler further explored the peculiarities of the Dirac equation, revealing non-linear modifications in Maxwell's equations due to the interaction of electromagnetic fields with the electron vacuum loop[3]. J. Schwinger's groundbreaking work in 1951 precisely calculated the imaginary part of the one-loop effective Lagrangian in the presence of a static electric field [4]. As a result of his seminal work, the phenomenon of vacuum pair creation by electric fields has since become widely known as the Schwinger effect, and it is also famously referred to as the Sauter-Schwinger effect in recognition of F. Sauter's prior work on solving the Dirac equation in the presence of an electric field [5]. Schwinger's pioneering calculation opened up new avenues of research in quantum field theory and has profoundly impacted our understanding of particle physics in the presence of strong fields. This extraordinary property of quantum vacuum producing spontaneous particle-antiparticle pairs has far-reaching implications for understanding the generation of particle-antiparticle pairs in the presence of a strong electric field [6]; particle creation in the expanding universe[7]; black hole evaporation as a result of Hawking radiation [8, 9]; and Unruh radiation, in which particle production is seen by an accelerating observer[10, 11]. The study of generating electron-positron pairs through a spatially constant electrical background field was extended to the electric field with various time dependences. In the 1970s, researchers explored the occurrence of pair production from the vacuum in the presence of an oscillating time-dependent electric field [12, 13]. Their investigations revealed different qualitative behaviors for this process under various interaction regimes. The interaction regimes can be distinguished by the value of the dimensionless Keldysh parameter  $\gamma = \frac{m\omega}{|e|E_0}$  [14], with field amplitude  $E_0$ , field frequency  $\omega$ , electron charge  $e$ , and mass  $m$ . When  $\gamma \gg 1$ , the process probability shows a perturbative power-law scaling with field intensity. Instead, for  $\gamma \ll 1$ , it exhibits a manifestly non-perturbative exponential dependence on  $\frac{1}{E_0}$ , similar to the case of a constant electric field [15]. Particle production in a spatially homogeneous single pulse of an electric field has been explored [16, 17], and methods for tackling particle creation in an arbitrary time-dependent electric field have been developed [16, 18, 19]. Because a single pulse of an electric field is an idealized

form of an electric field created by two colliding laser beams, particle generation in an alternating electric field has been explored for a more realistic scenario [20, 21]. However, it was found that the mass of the created particle, via the Schwinger mechanism, exponentially suppresses the pair generation rate, necessitating a very strong electric field to observe this phenomenon. Therefore, this event has not yet been the subject of any experimental observations. This makes it unclear how well theoretical prediction captures the physics of pair production. Nevertheless, the study of pair production in strong electric fields subject has attracted sustained interest from theoreticians in recent years due to the extraordinary progress in the development of the ultra-intense lasers technique and the strong field QED experimental studies that are planned at upcoming high-intensity laser facilities, such as the European X-Ray Free-Electron Laser [22], the Extreme-Light Infrastructure [23, 24], the Exawatt Center for Extreme Light Studies [25]. The electric field strength is fast getting closer to the critical value  $E_c$ . Additionally, it is suggested that the Schwinger mechanism can be indirectly tested in the condensed matter system of a single monolayer of graphene, where the electrons are roughly characterized by the massless pseudo-relativistic Dirac equation [26–28].

Particle production can be viewed as evolving a quantum system from an initial equilibrium configuration to a new final equilibrium configuration via an intermediate non-equilibrium evolution caused by a strong field background. In intermediate non-equilibrium states, when matter fields interact with a time-dependent external field, the classical Hamiltonian loses its time-translation invariance, leading to the evolution of the vacuum state into a state where mixing between positive and negative energy states occurs. Special care is needed in identifying “positive” and “negative” energy states in the presence of an external electric field. Thus, energy is no longer a good quantum number, and there is no well-defined quantum number to characterize a “particle”. However, the standard way of describing particle creation by an external field involves the asymptotic analysis of particle states in the remote past (or in-states, before the external field is switched on) and the distant future (or out-states, long after the interaction with the external field has ended). This method is well understood using the quantum field operator expression in terms of creation and annihilation operators, which are connected to single-particle states in both the past and the future. Then, by relating the two sets of operators in the past and future, one can derive an equation for the S-matrix of the process. This equation, in turn, determines the number of particles produced in the process. Various methodologies have been developed to investigate pair production in the presence of strong fields. These include the proper-time method [4, 29], the canonical method [30–32], Green’s function techniques [33], semiclassical tunneling [9], the Schrödinger-

functional approach [34], functional techniques [35–37], the Wigner formalism [38–40], mean-field treatments [41], and worldline instanton methods [42, 43]. Studies on pair production in intense laser fields [44, 45] have employed analytical and numerical approaches to predict pair-production rates. However, these investigations primarily focus on pair formation at asymptotic times, which alone is insufficient for fully capturing the dynamical aspects of pair production and its time-dependent effects. Several authors have derived expressions for the number of pairs created after a time  $T$ , where  $T$  extends beyond the duration of the electric field pulse or the point at which the field vanishes [33, 46–49]. These expressions provide a reliable approximation of the actual pair count. Understanding pair production dynamics from the initial to final states requires a framework that accounts for transient and non-equilibrium effects. In this context, the distribution function of quasiparticles, governed by the quantum kinetic equation (QKE), offers an effective description of the time-dependent evolution of pair production [50]. Defining the particle distribution function in the quasiparticle basis is both physically meaningful and intuitive. This approach is grounded in the straightforward physics of how a time-dependent field distorts the time invariance symmetry of the Hamiltonian, leading to mixing between momentum states of positive and negative energies. This method is particularly relevant for exploring the complex dynamical behavior of pair production in spatially uniform, time-dependent electric fields. Specifically, it has been demonstrated that the temporal evolution of the quasiparticle distribution function in momentum space provides insights into the asymptotic states of the quantum field and offers a comprehensive description of the process during the interaction between the matter field and the strong field background [51]. It was shown that the distribution function evolves through three distinct temporal stages: the quasi-electron-positron plasma (QEPP) stage, the transient stage, and finally the residual electron-positron plasma (REPP) stage [52, 53]. In examining the pair production process, both the QEPP stage, where quasi-particles are formed, and the REPP stage, where real particles emerge, are crucial. While the Schwinger mechanism is primarily known for producing elementary particles in a vacuum under external fields, it can also generate quasiparticle excitations in exotic materials such as graphene [26–28, 54, 55], which are experimentally more accessible, and in superconductors [56]. Moreover, while ultracold atoms in optical lattices have been investigated as simulators for the Schwinger mechanism [57, 58], they offer an alternative platform to study these phenomena [59].

In the present work, we consider the production of electron-positron pairs from the vacuum in a time-varying, spatially uniform pulsed electric field given by  $E(t) = E_0 \text{sech}^2\left(\frac{t}{\tau}\right)$ , with amplitude  $E_0$  and pulse duration  $\tau$ . Such background field has received extensive attention in the

literature [16, 27, 33, 60–63], with a focus on the asymptotic behavior of the probability of pair production. To this end, we study the evolution of the single-particle distribution function,  $f(\mathbf{p}, t)$ , which is rigorously derived by canonical quantization of the Dirac field and subsequent Bogoliubov transformation to a quasi-particle representation [64]. The distribution function exhibits three distinct dynamical stages[52, 64–66]. By analyzing the temporal evolution of  $f(\mathbf{p}, t)$ , we find that the emergence and characteristics of these dynamical stages—QEPP, transient, and REPP—are qualitatively and quantitatively influenced by both longitudinal and transverse momentum values. Next, we analyze the longitudinal momentum spectrum (LMS) of the particles at finite times. In the tunneling regime ( $\gamma < 1$ ), we observe oscillatory behavior in the LMS at time  $t > 2\tau$ , and this oscillation pattern continuously changes from  $t > 2\tau$  up to  $t < 6\tau$  for  $\gamma = 0.5$ . This oscillatory behavior at finite times clearly illustrates the quantum interference effects arising from various dynamical processes and channels contributing to the creation of (quasi-)particles with a given momentum. It can also be understood in terms of the vacuum polarization function  $u(\mathbf{p}, t)$  and its counterpart, the depolarization function  $v(\mathbf{p}, t)$ , which encapsulate the underlying particle production dynamics. We emphasize that the oscillations seen in the LMS are not artifacts but rather possess significant physical relevance. In the multi-photon regime, we observe that LMS at finite times near  $t = 3\tau$  exhibits a multi-modal structure. Furthermore, we develop an analytical framework valid for finite times  $t > \tau$ . Specifically, we derive an analytical expression for the single-particle distribution function as a power series in the small parameter  $(1 - y)$ , where  $y = \frac{1}{2}(1 + \tanh(\frac{t}{\tau}))$ . The intriguing dynamical features of the momentum distribution function at finite times arise from a function appearing in this expansion. The finite-time behavior of the momentum spectra can be understood in terms of functions that reveal three distinct phases, which are discussed in detail in the results section. Additionally, we explored how the transverse momentum affects LMS and discovered that the oscillatory behavior depends on the value of  $p_{\perp}$  at that time. Subsequently, we analyzed the temporal progression of transverse momentum spectrum(TMS) of generated pairs, providing valuable insights into the pair production process. At finite times, the transverse momentum spectra reaches its peak at a nonzero value, reflecting the influence of multiphoton transitions in quasiparticle creation.

The preliminary results of this work were presented in Refs. [67, 68]. After seeing the report in Ref. [67], one of the authors of Ref. [69], Kohlfürst, informed us in a private communication about their findings, which exhibit some overlap with the results presented here. In this manuscript, we compare and discuss our findings in relation to those of Ref. [69] whenever applicable.

This article is organized as follows: In Sec.II detailed the theoretical formulation is given. This

largely follows the derivation from [70, 71]. In Sec. III, we present expressions for the particle momentum distribution function using the exact analytical solution for the mode function in the case of a Sauter-pulsed electric field. Results are discussed in Sec. IV. The article is concluded in Sec. V.

Throughout the paper, we use natural units and set  $\hbar = c = m = |e| = 1$ , the electric charge  $e < 0$ , and express all variables in terms of the electron mass unit.

## II. THEORY

In this section, we review the canonical quantization method within the context of a strong electric field, as discussed in [71]. This approach offers valuable insights into pair production phenomena, including detailed information on particle number and momentum distribution at each moment. To begin, we establish solutions for the single-particle scenario governed by the Dirac equation in the presence of such a field. We start by writing the Dirac equation for a particle in an electromagnetic field, which takes the following form:

$$(i\gamma^\mu \partial_\mu - e\gamma^\mu A_\mu - m)\Psi(\mathbf{x}, t) = 0, \quad (1)$$

where  $A^\mu$  is the four-vector potential,  $\Psi(\mathbf{x}, t)$  is the four-component spinor. For  $\gamma$ -matrices we chose the weyl basis [72]

$$\gamma^0 = \begin{pmatrix} \mathbb{I} & 0 \\ 0 & -\mathbb{I} \end{pmatrix}, \gamma^i = \begin{pmatrix} 0 & -\sigma^i \\ \sigma^i & 0 \end{pmatrix}, i = 1, 2, 3, \quad (2)$$

where  $\mathbb{I}$  is the identity matrix and  $\sigma^i$  are the Pauli matrices. The  $\gamma$  matrices satisfy the anti-commutation relations:

$$\{\gamma^\mu, \gamma^\nu\} = 2g^{\mu\nu}, \quad (3)$$

with the metric tensor,

$$g^{\mu\nu} = \text{diag}(1, -1, -1, -1). \quad (4)$$

Four coupled differential equations result from the Dirac equation for the spinor, and it is typically challenging to find precise analytical solutions in the presence of external fields. Feynman and Gell-Mann were able to circumvent this difficulty by taking into account a two-component form

of the Dirac equation [73]. Accordingly, we turn this equation into a second-order differential equation by assuming the existence of a bispinor  $\chi(\mathbf{x}, t)$  such that

$$\Psi(\mathbf{x}, t) = (i\gamma^v \partial_v - e\gamma^v A_v + m)\chi(\mathbf{x}, t). \quad (5)$$

and inserting Eq. (5) into Eq. (1), it follows that  $\chi(\mathbf{x}, t)$  satisfies the quadratic Dirac equation

$$[(i\partial_\mu - eA_\mu)^2 - \frac{e}{2}\sigma^{\mu\nu}\mathcal{F}_{\mu\nu} - m^2]\chi(\mathbf{x}, t) = 0, \quad (6)$$

where  $\mathcal{F}_{\mu\nu} = \partial_\mu A_\nu - \partial_\nu A_\mu$  is the field strength tensor,  $\sigma^{\mu\nu} = \frac{i}{2}[\gamma^\mu, \gamma^\nu]$  and  $\chi(\mathbf{x}, t)$  is a four component spinor.

In general,  $\mathcal{F}_{\mu\nu}$  is space and time dependent. However, to simplify the discussion, we consider the case where the electromagnetic field tensor is  $\mathcal{F}^{\mu 0} = (0, \mathbf{E}(t)) \equiv (0, 0, 0, E(t))$  with  $E(t)$  linearly polarized time-dependent quasi-classical spatially uniform electric field along the  $z$ -axis and the corresponding four-vector potential  $A^\mu(\mathbf{x}, t) = (0, \mathbf{A}(t)) \equiv (0, 0, 0, A(t))$ , with an arbitrary  $A(t)$  such that  $E(t) = -\frac{dA(t)}{dt}$ .

Then, now Eq.(6) can be simplified to

$$[\partial_\mu \partial^\mu + e^2 A^2(t) + 2iA(t)\partial_3 - ie\partial_t A(t)\gamma^0\gamma^3 + m^2]\chi(\mathbf{x}, t) = 0. \quad (7)$$

Spatial homogeneity implies that the solutions can be expressed in the form of

$$\chi(\mathbf{x}, t) = e^{i\mathbf{p}\cdot\mathbf{x}}\chi_{\mathbf{p}}(t), \quad (8)$$

where  $\chi_{\mathbf{p}}(t)$  is independent of the position  $\mathbf{x}$  and we label it by momentum of a particle  $\mathbf{p}$ .

Subsequently, Eq. (7) becomes

$$\left(\partial_t^2 + ieE(t)\gamma^0\gamma^3 + \omega^2(\mathbf{p}, t)\right)\chi_{\mathbf{p}}(t) = 0, \quad (9)$$

where

$$\omega^2(\mathbf{p}, t) = p_\perp^2 + (p_\parallel - eA(t))^2 + m^2 \quad (10)$$

is expressed in terms of the transverse energy  $\epsilon_\perp^2(p_\perp) = m^2 + p_\perp^2$ , longitudinal  $p_\parallel = p_3$  is the momentum component to the field direction and  $p_\perp = \sqrt{p_1^2 + p_2^2}$  is the modulus of the vector  $\mathbf{p}_\perp$  perpendicular to the field.

We now expand the function  $\chi_{\mathbf{p}}(t)$  in the basis of eigenvectors of  $\gamma^0\gamma^3$ . The matrix representation of  $\gamma^0\gamma^3$  is

$$\gamma^0\gamma^3 = \begin{pmatrix} \mathbb{I} & 0 \\ 0 & -\mathbb{I} \end{pmatrix} \begin{pmatrix} 0 & \sigma^3 \\ -\sigma^3 & 0 \end{pmatrix} = \begin{pmatrix} 0 & \sigma^3 \\ \sigma^3 & 0 \end{pmatrix}, \quad (11)$$

making it easy to recognize the eigenvector. They are given by

$$R_1 = \begin{pmatrix} 1 \\ 0 \\ 0 \\ 0 \end{pmatrix}, \quad R_2 = \begin{pmatrix} 0 \\ 0 \\ 0 \\ 1 \end{pmatrix}, \quad R_3 = \begin{pmatrix} 0 \\ 1 \\ 0 \\ 0 \end{pmatrix}, \quad R_4 = \begin{pmatrix} 0 \\ 0 \\ 1 \\ 0 \end{pmatrix}. \quad (12)$$

There are two doubly degenerate eigenvectors for  $\gamma^0\gamma^3$ :  $R_1$  and  $R_2$  with eigenvalue “1”, and  $R_3$  and  $R_4$  with eigenvalue “-1”. However, selecting one from each pair suffices [70]. Now, we will seek the solutions of Eq. (9) in the form

$$\chi_{\mathbf{p}}(t) \equiv \chi_{\mathbf{p}r}(t) = \psi_{\mathbf{p}}(t)R_r, \quad (13)$$

where  $\gamma^0\gamma^3 R_r = R_r$ .

Solving a differential equation for a scalar function  $\psi_{\mathbf{p}}(t)$  simplifies the problem,

$$\left(\partial_t^2 + ieE(t) + \omega^2(\mathbf{p}, t)\right)\psi_{\mathbf{p}}(t) = 0. \quad (14)$$

Let's examine the resulting solutions. According to Eq. (14), in a vanishing electric field as  $t \rightarrow -\infty$ ,  $\omega(\mathbf{p}, t)$  becomes independent of time, denoted  $\omega(\mathbf{p}) = \sqrt{m^2 + \mathbf{p}^2}$ . The scalar function  $\psi(\mathbf{p}, t)$  then satisfies the asymptotic equation,

$$\left(\partial_t^2 + \omega^2(\mathbf{p})\right)\psi_{\mathbf{p}}(t) = 0. \quad (15)$$

There are two linearly independent solutions to this time-dependent harmonic oscillator equation, which correspond to energy  $\pm\omega(\mathbf{p})$ . In what follows, we will label these solutions with superscripts  $\lambda = +$  and  $\lambda = -$ , respectively. The solutions to Eq. (15), are clearly given by plane waves. Therefore,

$$\psi_{\mathbf{p}}^{(\lambda)}(t) \underset{t \rightarrow -\infty}{\sim} e^{-i\lambda\omega(\mathbf{p})t}. \quad (16)$$

These solutions will be interpreted as describing an electron ( $\lambda = +$ ) and its anti-particle, i.e., a



positron ( $\lambda = -$ ).

Finally, the corresponding solutions of Eq. (7) have the form,

$$\chi_{\mathbf{p}r}^{(\lambda)}(\mathbf{x}, t) = e^{i\mathbf{p}\cdot\mathbf{x}}\psi_{\mathbf{p}}^{(\lambda)}(t)R_r, \quad (17)$$

those of the Dirac equation, however, are derived

$$\Psi_{\mathbf{p}r}^{(\lambda)}(\mathbf{x}, t) = \left[ i\gamma^0\partial_t + \gamma^i p_i - e\gamma^3 A(t) + m \right] \psi_{\mathbf{p}}^{(\lambda)}(t)R_r e^{i\mathbf{p}\cdot\mathbf{x}}, \quad (18)$$

where the spinor solutions,  $\Psi_{\mathbf{p}r}^{(\lambda)}(\mathbf{x}, t)$  are normalised according to the product:

$$\int d^3\mathbf{x} [\Psi_{\mathbf{p}r}^{(\lambda)}(\mathbf{x}, t)]^\dagger \Psi_{\mathbf{p}'r'}^{(\lambda')}(\mathbf{x}, t) = (2\pi)^3 \delta(\mathbf{p} - \mathbf{p}') \delta_{rr'} \delta_{\lambda\lambda'}. \quad (19)$$

Hence, the newly constructed eigenstates of the Dirac equation representing an electron or positron in a time-dependent electric field provide a complete and orthonormal relation

$$\sum_{\lambda=\pm} \sum_{r=\pm} \int \frac{d^3\mathbf{p}}{(2\pi)^3} \Psi_{\mathbf{p}r}^{(\lambda)}(\mathbf{x}, t) [\Psi_{\mathbf{p}'r'}^{(\lambda)}(\mathbf{x}', t)]^\dagger = \delta(\mathbf{x} - \mathbf{x}'). \quad (20)$$

The Dirac fermion field operator  $\hat{\Psi}(\mathbf{x}, t)$  in the framework of second quantization is written in the form

$$\hat{\Psi}(\mathbf{x}, t) = \sum_r \int \frac{d^3\mathbf{p}}{(2\pi)^3} \left( \Psi_{\mathbf{p}r}^{(+)}(\mathbf{x}, t) \hat{b}_{\mathbf{p}r} + \Psi_{-\mathbf{p}r}^{(-)}(\mathbf{x}, t) \hat{d}_{\mathbf{p}r}^\dagger \right), \quad (21)$$

where  $\Psi_{\mathbf{p}r}^{(\lambda)}(\mathbf{x}, t)$  are the single-particle solutions of the Dirac equation, whereas  $\hat{b}_{\mathbf{p}r}$  and  $\hat{d}_{\mathbf{p}r}^\dagger$  are the electron annihilation and positron creation operator respectively. The operators satisfy the usual fermionic anti-commutation relations,

$$\{\hat{b}_{\mathbf{p}r}, \hat{b}_{\mathbf{p}'r'}^\dagger\} = \{\hat{d}_{\mathbf{p}r}, \hat{d}_{\mathbf{p}'r'}^\dagger\} = \delta(\mathbf{p} - \mathbf{p}') \delta_{rr'}. \quad (22)$$

Then the  $\hat{\Psi}(\mathbf{x}, t)$  field operator also satisfies the anti-commutation relation,

$$\{\hat{\Psi}_n(\mathbf{x}, t), \hat{\Psi}_m^\dagger(\mathbf{x}', t)\} = (2\pi)^3 \delta(\mathbf{x} - \mathbf{x}') \delta_{mn}. \quad (23)$$

Now, the Hamiltonian can be calculated from the energy-momentum tensor which yields,

$$\hat{H}(t) = i \int \hat{\Psi}^\dagger(\mathbf{x}, t) \dot{\hat{\Psi}}(\mathbf{x}, t) d^3\mathbf{x}, \quad (24)$$

the diagonal and off-diagonal parts of the Hamiltonian are given as

$$\hat{H}_{diag}(t) = i \sum_r \int \frac{d^3 \mathbf{p}}{(2\pi)^3} \left[ \varepsilon_{\mathbf{p}}^{(++)}(t) \hat{b}_{pr}^\dagger \hat{b}_{pr} + \varepsilon_{\mathbf{p}}^{(--)}(t) \hat{d}_{-pr}^\dagger \hat{d}_{-pr} \right], \quad (25)$$

$$\hat{H}_{offdiag}(t) = i \sum_r \int \frac{d^3 \mathbf{p}}{(2\pi)^3} \left[ \varepsilon_{\mathbf{p}}^{(+-)}(t) \hat{b}_{pr}^\dagger \hat{d}_{-pr}^\dagger + \varepsilon_{\mathbf{p}}^{(-+)}(t) \hat{d}_{-pr} \hat{b}_{pr} \right], \quad (26)$$

where the factors  $\varepsilon_{\mathbf{p}}^{(\lambda\lambda')}(t)$  are expressed as

$$\varepsilon_{\mathbf{p}}^{(\lambda\lambda')}(t) = \begin{cases} -(p_{\parallel} - eA(t)) - 2\varepsilon_{\perp}^2(p_{\perp}) \text{Im}([\psi_{\mathbf{p}}^{(\lambda)}(t)]^* \dot{\psi}_{\mathbf{p}}^{(\lambda)}(t)) & \text{if } \lambda = \lambda', \\ i\varepsilon_{\perp}^2(p_{\perp}) ([\psi_{\mathbf{p}}^{(\lambda)}(t)]^* \dot{\psi}_{\mathbf{p}}^{(\lambda')}(t) - [\dot{\psi}_{\mathbf{p}}^{(\lambda)}(t)]^* \psi_{\mathbf{p}}^{(\lambda')}(t)) & \text{if } \lambda \neq \lambda'. \end{cases} \quad (27)$$

As the above Hamiltonian has non-vanishing off-diagonal terms, the positive and negative energy modes mix, and thus, a clear interpretation in terms of particles and antiparticles is difficult.

In order to calculate the spectrum, the Hamiltonian is diagonalized through a basis transformation to the quasi-particle representation using the new time-dependent operators  $\hat{B}_{pr}(t)$  and  $\hat{D}_{pr}(t)$ . The relation between the  $\hat{b}_{pr}$ ,  $\hat{d}_{pr}$  and  $\hat{B}_{pr}(t)$ ,  $\hat{D}_{pr}(t)$  operators is given by the Bogoliubov transformation [71, 74]

$$\hat{B}_{pr}(t) = \alpha_{\mathbf{p}}(t) \hat{b}_{pr} + \beta_{\mathbf{p}}(t) \hat{d}_{-pr}^\dagger, \quad (28)$$

$$\hat{D}_{pr}(t) = \alpha_{-\mathbf{p}}(t) \hat{d}_{pr} - \beta_{-\mathbf{p}}(t) \hat{b}_{-pr}^\dagger. \quad (29)$$

with the condition,

$$|\alpha_{\mathbf{p}}(t)|^2 + |\beta_{\mathbf{p}}(t)|^2 = 1. \quad (30)$$

Here, the operators  $\hat{B}_{pr}(t)$  and  $\hat{D}_{pr}(t)$  describe the creation and annihilation of quasiparticles at time  $t$  with respect to the instantaneous vacuum state. The substitution of Eqs. (28) and (29) into Eq. (21) results in a new representation of the field operator

$$\hat{\Psi}(\mathbf{x}, t) = \sum_r \int \frac{d^3 \mathbf{p}}{(2\pi)^3} \left[ \Phi_{pr}^{(+)}(\mathbf{x}, t) \hat{B}_{pr}(t) + \Phi_{-pr}^{(-)}(\mathbf{x}, t) \hat{D}_{pr}^\dagger(t) \right], \quad (31)$$

with the spinors  $\Phi_{pr}^{(\lambda)}(\mathbf{x}, t)$  such that

$$\Phi_{pr}^{(+)}(\mathbf{x}, t) = \alpha_p^*(t)\Psi_{pr}^{(+)}(\mathbf{x}, t) + \beta_p^*(t)\Psi_{pr}^{(-)}(\mathbf{x}, t), \quad (32)$$

$$\Phi_{pr}^{(-)}(\mathbf{x}, t) = \alpha_p(t)\Psi_{pr}^{(-)}(\mathbf{x}, t) - \beta_p(t)\Psi_{pr}^{(+)}(\mathbf{x}, t). \quad (33)$$

It follows from this that  $\Phi_{pr}^{(\lambda)}(\mathbf{x}, t)$  have a spin structure similar to that of  $\Psi_{pr}^{(\lambda)}(\mathbf{x}, t)$  in Eq. (18),

$$\Phi_{pr}^{(\lambda)}(\mathbf{x}, t) = \left[ i\gamma^0\partial_t - \mathbf{p} \cdot \boldsymbol{\gamma} + eA(t)\gamma^3 + m \right] e^{i\mathbf{p}\cdot\mathbf{x}} \phi_p^{(\lambda)}(t) R_r. \quad (34)$$

The function  $\phi_p^{(\lambda)}(t)$  is the mode function in the quasi-particle representation, chosen according to the ansatz.

$$\phi_p^{(\lambda)}(t) = \frac{e^{-i\lambda\Theta_p(t)}}{\sqrt{2\omega(\mathbf{p}, t)(\omega(\mathbf{p}, t) - \lambda P(p_{\parallel}, t))}}, \quad (35)$$

with the dynamical phase  $\Theta_p(t) = \int_{t_0}^t \omega(\mathbf{p}, t') dt'$ . The functions  $\phi_p^{(\pm)}(t)$  are chosen such that they coincide with the mode functions  $\psi_p^{(\pm)}(t)$  in the case of a vanishing electric field.

Now, combining Eqs. (18), (32) to (34), we obtain that

$$\psi_p^{(+)}(t) = \alpha_p(t)\phi_p^{(+)}(t) - \beta_p^*(t)\phi_p^{(-)}(t), \quad (36)$$

$$\psi_p^{(-)}(t) = \beta_p(t)\phi_p^{(+)}(t) + \alpha_p^*(t)\phi_p^{(-)}(t). \quad (37)$$

and the coefficients  $\alpha_p(t)$  and  $\beta_p(t)$  are given by

$$\alpha_p(t) = i\phi_p^{(-)}(t)\epsilon_{\perp}(p_{\perp})(\partial_t - i\omega(\mathbf{p}, t))\psi_p^{(+)}(t), \quad (38)$$

$$\beta_p(t) = -i\phi_p^{(+)}(t)\epsilon_{\perp}(p_{\perp})(\partial_t + i\omega(\mathbf{p}, t))\psi_p^{(+)}(t). \quad (39)$$

From the above equations, if we know  $\psi_p(t)$  from a solution of differential Eq. (14) for a specific electric field, we can find out the Bogolyubov transformation coefficients.

We now define the occupation number of electrons in the given eigenmode  $pr$  of the fermionic field using the time-dependent creation and annihilation operators for the initial vacuum state is defined as

$$f_r(\mathbf{p}, t) = \langle 0_{in} | \hat{B}_{pr}^{\dagger}(t) \hat{B}_{pr}(t) | 0_{in} \rangle \quad (40)$$

Similarly, the occupation number of the positron is given by

$$\bar{f}_r(-\mathbf{p}, t) = \langle 0_{in} | \hat{D}_{-pr}^\dagger(t) \hat{D}_{-pr}(t) | 0_{in} \rangle \quad (41)$$

Because of the charge conjugation invariance,

$$f_r(\mathbf{p}, t) = \bar{f}_r(-\mathbf{p}, t) \quad (42)$$

In the quasi-particle representation,  $f_r(\mathbf{p}, t)$  and  $\bar{f}_r(-\mathbf{p}, t)$  will act as single-particle distribution functions [74]. Since the Hamiltonian Eq.(24) does not have any spin-dependent terms, the spin index( $r$ ) is dropped, and the distribution function

$$f(\mathbf{p}, t) = 2|\beta_p(t)|^2 \quad (43)$$

where the factor “2” corresponds to the spin degree of freedom. One approach to find  $f(\mathbf{p}, t)$  involves solving Eq. (14) for  $\psi_p(t)$  and subsequently using it to determine the Bogoliubov coefficients, which are essential for obtaining the single-particle distribution function.

### III. PAIR PRODUCTION IN SAUTER-PULSE ELECTRIC FIELD

A spatially uniform external background is a common approximation of the electromagnetic field near the focal region of two counter-propagating laser pulses along the z-axis, generating a standing wave [75, 76]. In general, the pair-production process takes place close to the electric field maximum (comparable to the critical field limit), where the magnetic field vanishes. Despite the fact that laser fields typically include many optical cycles, in this case, we examine a relatively simple model of the external field made up of the Sauter profile, which can be thought of as an extremely short laser pulse.

$$E(t) = E_0 \text{sech}^2\left(\frac{t}{\tau}\right), \quad (44)$$

where  $\tau$  is the duration of pulse and  $E_0$  is field strength. This electric field exponentially goes to zero for  $|t| \gg \tau$ . In the limit of  $\tau \rightarrow \infty$  the electric field becomes homogeneous in time. We can choose a gauge in which  $A_0 = 0$  and the vector potential associated with the electric field is  $(0, 0, A(t) = -\int dt E(t))$ . After the integration, we find the Sauter-type gauge potential,

$$A(t) = -E_0 \tau \tanh\left(\frac{t}{\tau}\right). \quad (45)$$

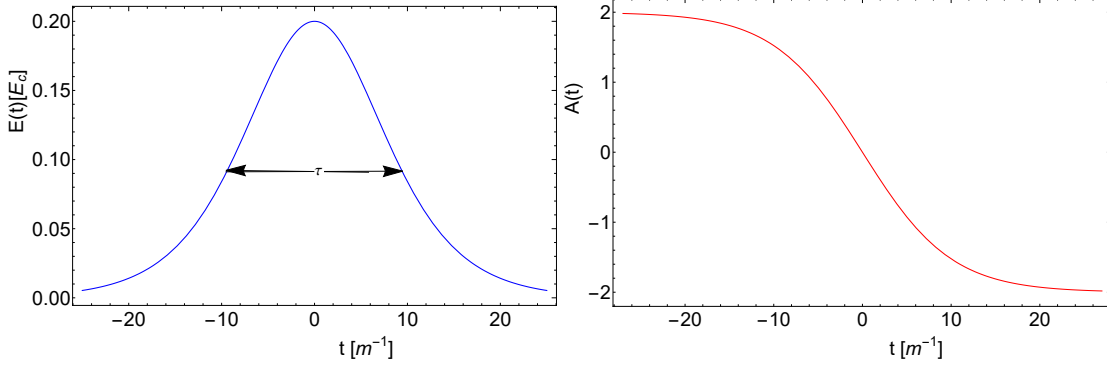


Figure 1: Temporal profile of the electric field (left) and the associated vector potential with the choice  $A(t = 0) = 0$ (right). The field parameters are  $E_0 = 0.2E_c$  and  $\tau = 10[m^{-1}]$  and all the units are taken in the electron mass unit.

with  $A(t = 0) = 0$ . The left panel of figure 1 shows the temporal profile of the electric field given by Eq.(44). Its peak height is attained at  $t = 0$ , its half height is reached at  $t = \pm 0.81\tau$ , and at  $t = \pm\tau$ , the pulse amplitude has already dropped to 41% of its peak height, followed by a further dramatic reduction well below 10% at  $t = \pm 2\tau$ .

Originally, Sauter explored the Dirac equation within an inhomogeneous scalar potential  $V(z) = V_0 \text{sech}\left(\frac{z}{d}\right)^2$  [5]. Since the problem is essentially reduced to solving a one-dimensional differential equation, the potential can also be addressed with a similar functional dependence on time, as given by Eq. (44). In 1970, the vacuum instability in a time-dependent Sauter-like electric field was initially examined by N. B. Narozhny et al. [16]. Subsequently, many researchers revisited this topic, finding it practical to test various approaches, including approximate methods, in the specific context being considered. Examples include Refs.[77–81], and the references therein. However, for the sake of completeness, we reproduce the essential steps and find out the expression for the single-particle distribution function,  $f(\mathbf{p}, t)$ , utilizing the solution of the differential equation.

Now, in the presence of external electric field Eq. (44) equation of motion for mode function Eq. (14) reads

$$\left(\partial_t^2 + iE_0 \text{sech}^2\left(\frac{t}{\tau}\right) + \omega^2(\mathbf{p}, t)\right)\psi_{\mathbf{p}}(t) = 0. \quad (46)$$

where we have skipped the irrelevant index  $\lambda$  of the mode function  $\psi_{\mathbf{p}}(t)$ . This equation is solved analytically by converting it into a hypergeometric differential equation. By changing the time variable to

$$y = \frac{1}{2} \left(1 + \tanh\left(\frac{t}{\tau}\right)\right). \quad (47)$$

Additionally, we compute

$$\partial_t = (\partial_t y) \partial_y = \frac{2}{\tau} y(1-y) \partial_y \quad (48)$$

$$\partial_t^2 = \frac{4}{\tau^2} y(1-y) \partial_y y(1-y) \quad (49)$$

Now, Eq.(46) can be rewritten as

$$\left( \frac{4}{\tau^2} y(1-y) \partial_y y(1-y) \partial_y + \omega^2(\mathbf{p}, y) + 4iE_0 y(1-y) \right) \psi_{\mathbf{p}}(y) = 0. \quad (50)$$

Further, by using the following ansatz

$$\psi_{\mathbf{p}}(y) = y^k (1-y)^l \eta_{\mathbf{p}}(y) \quad (51)$$

with,  $k = \frac{-i\tau\omega_0}{2}$ ,  $l = \frac{i\tau\omega_1}{2}$ ,  $\omega_0 = \sqrt{\epsilon_{\perp}^2 + P_0^2}$ ,  $\omega_1 = \sqrt{\epsilon_{\perp}^2 + P_1^2}$ ,  $P_0 = (p_{\parallel} - eE_0\tau)$ ,  $P_1 = (p_{\parallel} + eE_0\tau)$ , in Eq. (50), we have  $\eta_{\mathbf{p}}(y)$  satisfying the following hypergeometric differential equation [82]

$$\left( y(1-y) \partial_y^2 + (c - (a+b+1)y) \partial_y - ab \right) \eta_{\mathbf{p}}(y) = 0. \quad (52)$$

Here,

$$\begin{aligned} a &= -iE_0\tau^2 - \frac{i\tau\omega_0}{2} + \frac{i\tau\omega_1}{2} = i\zeta_1 \\ b &= 1 + iE_0\tau^2 - \frac{i\tau\omega_0}{2} + \frac{i\tau\omega_1}{2} = 1 + i\zeta_2, \\ c &= 1 - i\tau\omega_0 = 1 + i\zeta_3. \end{aligned} \quad (53)$$

The two linearly independent solutions of Eq.(52) are

$$\eta_{\mathbf{p}}^{(+)}(y) = {}_2\mathcal{F}_1(a, b, c; y), \quad (54)$$

$$\eta_{\mathbf{p}}^{(-)}(y) = y^{1-c} (1-y)^{c-a-b} {}_2\mathcal{F}_1(1-a, 1-b, 2-c; y). \quad (55)$$

with  ${}_2\mathcal{F}_1(a, b, c; y)$  denoting the Gauss-hypergeometric function[82].

To get the mode functions  $\psi_{\mathbf{p}}^{(\pm)}(y)$  we have to resubstitute  $\eta_{\mathbf{p}}^{(\pm)}(y)$  in our ansatz Eq.(51)

$$\psi_{\mathbf{p}}^{(+)}(y) = N^{(+)}(\mathbf{p})y^k (1-y)^l {}_2\mathcal{F}_1(a, b, c; y), \quad (56)$$

$$\psi_{\mathbf{p}}^{(-)}(y) = N^{(-)}(\mathbf{p})y^{-k} (1-y)^{-l} {}_2\mathcal{F}_1(1-a, 1-b, 2-c; y), \quad (57)$$

where  $N^{(\pm)}(\mathbf{p})$  as normalization constants (see appendix A 1 for detailed calculations).

### A. Particle distribution function

To obtain the single-particle distribution function using the function  $\beta(\mathbf{p}, t)$  in terms of the new time variable  $y$ . This transformation yields

$$|\beta(\mathbf{p}, y)|^2 = \frac{\epsilon_{\perp}^2(p_{\perp})}{2\omega(\mathbf{p}, y)(\omega(\mathbf{p}, y) - P(p_{\parallel}, y))} \left| \left( \frac{2}{\tau} y(1-y) \partial_y + i\omega(\mathbf{p}, y) \right) \psi^{(+)}(\mathbf{p}, y) \right|^2. \quad (58)$$

Using Eq. (57), the analytical expression for the single-particle distribution function in terms of the transformed time variable  $y$  can be written as

$$f(\mathbf{p}, y) = |N^{+}(\mathbf{p})|^2 \left( \frac{\omega(\mathbf{p}, y) + P(p_{\parallel}, y)}{\omega(\mathbf{p}, y)} \right) \left| \frac{2}{\tau} y(1-y) \frac{ab}{c} f_1 + i(\omega(\mathbf{p}, y) - (1-y)\omega_0 - y\omega_1) f_2 \right|^2, \quad (59)$$

where  $f_1 = {}_2\mathcal{F}_1(1+a, 1+b, 1+c; y)$ ,  $f_2 = {}_2\mathcal{F}_1(a, b, c; y)$ . This expression for the time-dependent single-particle distribution function gives information about the pair production at the various dynamical stages[52, 83]. In this context, we focus on analyzing the evolution of the distribution function from the initial QEPP stage to the final REPP stage, passing through the transient stage. Within this formalism, the distribution function encodes the spectral information of produced particles, and its behavior is examined in detail in Sec. IV. Additionally, in Sec. III C, we derive a simple approximate expression for the distribution function, valid for  $t \gg \tau$ .

Furthermore, in order to analyze the characteristics of the vacuum polarization effect during the formation of pairs, we derive vacuum polarization and depolarization functions using the analytical expression of Bogoliubov coefficients in the proceeding section III B.

## B. Correlation function

Quantum Vacuum in the presence of an external electric field may be described by a complex correlation function [52, 53]. It is defined as,

$$C(\mathbf{p}, t) = \langle 0_{in} | \hat{D}_{-pr}^\dagger(t) \hat{B}_{pr}^\dagger(t) | 0_{in} \rangle = 2\alpha_{\mathbf{p}}^*(t)\beta_{\mathbf{p}}(t), \quad (60)$$

$$C^*(\mathbf{p}, t) = \langle 0_{in} | \hat{D}_{-pr}(t) \hat{B}_{pr}(t) | 0_{in} \rangle = 2\beta_{\mathbf{p}}^*(t)\alpha_{\mathbf{p}}(t). \quad (61)$$

As can easily be seen, this function  $C(\mathbf{p}, t)$ , consisting of creation operators for a particle and an anti-particle with the opposite momentum describes the process of production of  $e^-e^+$  pair. In several research articles [51–53, 74, 84], the particle-antiparticle correlation function is redefined by incorporating the slowly varying component of the time-dependent creation and annihilation operators in adiabatic number basis.

$$\hat{\mathcal{B}}_{pr}(t) = \hat{B}_{pr}(t)e^{-i\Theta_{\mathbf{p}}(t)}, \quad (62)$$

$$\hat{\mathcal{D}}_{-pr}(t) = \hat{D}_{-pr}(t)e^{-i\Theta_{\mathbf{p}}(t)}. \quad (63)$$

So that,

$$\begin{aligned} C(\mathbf{p}, t) &= \langle 0_{in} | \hat{\mathcal{D}}_{-pr}^\dagger(t) \hat{\mathcal{B}}_{pr}^\dagger(t) | 0_{in} \rangle, \\ &= e^{2i\Theta_{\mathbf{p}}(t)} \langle 0_{in} | \hat{D}_{-pr}^\dagger(t) \hat{B}_{pr}^\dagger(t) | 0_{in} \rangle, \\ &= 2\alpha_{\mathbf{p}}^*(t)\beta_{\mathbf{p}}(t)e^{2i\Theta_{\mathbf{p}}(t)}. \end{aligned} \quad (64)$$

Now, using the above relation for the pair correlation function in terms of the transformed time variable  $y$ , we proceed similarly to the derivation of the single-particle distribution function  $f(\mathbf{p}, t)$ .

$$\begin{aligned} C(\mathbf{p}, t) &= |N^+(\mathbf{p})|^2 \frac{\epsilon_{\perp}^2(\mathbf{p}_{\perp})}{\omega(\mathbf{p}, y)} \left[ \frac{4}{\tau^2} y^2 (1-y)^2 \left| \frac{ab}{c} \right|^2 |f_1|^2 - (\omega^2(\mathbf{p}, y) - (y\omega_1 + (1-y)\omega_0)^2) |f_2|^2 \right. \\ &\quad \left. - 2y(1-y)(\omega_1 - \omega_0 - 2E_0\tau) \left( (y\omega_1 + (1-y)\omega_0) \Re\left(\frac{b}{c} f_1 f_2^*\right) + i\omega(\mathbf{p}, y) \Im\left(\frac{b}{c} f_1 f_2^*\right) \right) \right] \end{aligned} \quad (65)$$



As we know, the vacuum polarization effects play a crucial role in the process of pair production. This effect is defined through the functions  $u(\mathbf{p}, t) = \Re(C(\mathbf{p}, t))$  and  $v(\mathbf{p}, t) = \Im(C(\mathbf{p}, t))$ [53].

$$u(\mathbf{p}, t) = |N^+(\mathbf{p})|^2 \frac{\epsilon_{\perp}^2(p_{\perp})}{\omega(\mathbf{p}, y)} \left( \frac{4}{\tau^2} y^2 (1-y)^2 \left| \frac{ab}{c} \right|^2 |f_1|^2 - (\omega^2(\mathbf{p}, y) - (y\omega_1 + (1-y)\omega_0)^2) |f_2|^2 \right. \\ \left. - 2y(1-y)(\omega_1 - \omega_0 - 2E_0\tau)(y\omega_1 + (1-y)\omega_0) \Re\left(\frac{b}{c} f_1 f_2^*\right) \right) \quad (66)$$

$$v(\mathbf{p}, t) = |N^+(\mathbf{p})|^2 2iy(1-y)(2E_0\tau + \omega_0 - \omega_1) \Im\left(\frac{b}{c} f_1 f_2^*\right) \quad (67)$$

The function  $u(\mathbf{p}, t)$  depicts vacuum polarization effects and pair production phenomena. The function  $v(\mathbf{p}, t)$  serves as counterterm to pair production, effectively representing pair annihilation in the vacuum excitation process. A comprehensive discussion of these insights is presented in detail in Sec. IV C.

### C. Approximate analytical expression for $f(\mathbf{p}, t)$ at finite time

To investigate the behavior of the distribution functions in the limit  $t > \tau$ , we employ approximations based on the suitable expressions of the Gamma and the Gauss-hypergeometric functions. These approximations enable us to deduce a simplified analytical expression for particle distribution functions. First, we start with approximating the Gauss-hypergeometric function as  $y \rightarrow 1$ . It is crucial to ensure smooth convergence towards the limit of  ${}_2\mathcal{F}_1(a, b, c; y \rightarrow 1)$ . This task is complicated by the intricate nature of the parameters  $a$ ,  $b$ , and  $c$  in this specific context, which makes it essential to exercise caution when dealing with this limit. Therefore, it is beneficial to transform the argument by substituting  $y$  with  $(1 - y)$ . This transition can be achieved using the following mathematical identity.

$${}_2\mathcal{F}_1(a, b, c; z) = \frac{\Gamma(c)\Gamma(c-a-b)}{\Gamma(c-a)\Gamma(c-b)} {}_2\mathcal{F}_1(a, b, a+b-c+1; 1-z) \\ + (1-z)^{c-a-b} \frac{\Gamma(c)\Gamma(a+b-c)}{\Gamma(a)\Gamma(b)} {}_2\mathcal{F}_1(c-a, c-b, c-a-b+1; 1-z). \quad |\arg(1-z)| < \pi \quad (68)$$

In general Gauss-hypergeometric function,

$${}_2F_1(a, b, c; z) = 1 + \frac{ab}{c}z + \frac{a(a+1)b(b+1)}{c(c+1)}\frac{z^2}{2!} + \frac{a(a+1)(a+2)b(b+1)(b+2)}{c(c+1)(c+2)}\frac{z^3}{3!} + \dots \quad (69)$$

The series continues with additional terms involving higher powers of  $z$ . Each term in the series involves the parameters  $a, b$ , and  $c$  as well as the variable  $z$  raised to a specific power.

Using the above relations Eq. (68) and (69), we approximate the Gauss-hypergeometric functions  $f_1$  and  $f_2$  present in the relation of the particle distribution function (see Eq.(59)) as follows:

$$\begin{aligned} f_1 = & \left( \frac{c\Gamma(c)\Gamma(c-a-b-1)}{\Gamma(c-a)\Gamma(c-b)} \right) \left( 1 + \frac{(a+1)(b+1)}{(2+a+b-c)}(1-y) \right. \\ & \left. + \frac{(a+1)(a+2)(b+1)(b+2)}{(2+a+b-c)(2+a+b-c+1)}\frac{(1-y)^2}{2!} + \dots \right) \\ & + (1-y)^{(c-a-b-1)}(a+b-c) \left( \frac{c\Gamma(c)\Gamma(a+b-c)}{a\Gamma(a)b\Gamma(b)} \right) \left( 1 + \frac{(c-a)(c-b)}{(c-a-b)}(1-y) \right. \\ & \left. + \frac{(c-a)(c-a+1)(c-b)(c-b+1)}{(c-a-b)(c-a-b+1)}\frac{(1-y)^2}{2!} + \dots \right) \end{aligned} \quad (70)$$

Similarly,

$$\begin{aligned} f_2 = & \frac{\Gamma(c)\Gamma(c-a-b)}{\Gamma(c-a)\Gamma(c-b)} \left( 1 + \frac{ab}{1+a+b-c}(1-y) + \dots \right) \\ & + (1-y)^{(c-a-b)} \frac{\Gamma(c)\Gamma(a+b-c)}{\Gamma(a)\Gamma(b)} \left( 1 + \frac{(c-a)(c-b)}{(1+c-a-b)}(1-y) + \dots \right) \end{aligned} \quad (71)$$

Here,  $y$  is a variable that changes with time according to Eq. (47). As time progresses, especially in the case with significant time intervals such as  $t > \tau$ , it becomes evident that  $(1-y)$  approaches zero. Consequently, the dominant contribution to the particle distribution function as  $y \rightarrow 1$  originates from the zeroth-order term, which is independent of  $(1-y)$ . As discussed in many literature for deriving the asymptotic expression for the particle distribution function, the Gauss-hypergeometric functions are truncated up to zeroth order only[33, 77].

Building on the earlier discussion (see Sec. III A), our focus is primarily on understanding the dynamics of particle distribution function over finite time rather than just its asymptotic trends. We want to examine the distribution function,  $f(\mathbf{p}, y)$ , in the vicinity of  $y \rightarrow 1$ . In that case, it is necessary to incorporate other higher-order terms in the expression of the asymptotic particle distribution function. It means expanding the time-dependent particle distribution function defined

in Eq. (59) as a power series in the variable  $(1 - y)$  as:

$$f(\mathbf{p}, y) \simeq C_0(\mathbf{p}, y) + (1 - y)C_1(\mathbf{p}, y) + (1 - y)^2C_2(\mathbf{p}, y) + \dots + (1 - y)^nC_n(\mathbf{p}, y). \quad (72)$$

To compute an approximate expression for the particle distribution function that depends on finite time, we can truncate the power series of the Gauss-hypergeometric functions  $f_1$  and  $f_2$  given by Eqs. (70) and (71) respectively, up to a specific order. The order of truncation will depend on the desired accuracy and the characteristics of the finite-time behavior under consideration.

Let's start by approximating the different terms present in the particle distribution Eq. (70) and (71), considering only up to the second-order terms and neglecting higher-order terms.

Therefore,

$$\begin{aligned} \frac{2y}{\tau}(1 - y)\frac{ab}{c}f_1 \approx & \frac{2}{\tau}y(a + b - c)\Gamma_2(1 - y)^{(c-a-b)} + (1 - y)\frac{2y}{\tau}\left(ab\Gamma_1 - (c - a)(c - b)\Gamma_2(1 - y)^{(c-a-b)}\right) \\ & + (1 - y)^2\frac{2y}{\tau}\left(\Gamma_1\frac{a(1 + a)b(1 + b)}{(2 + a + b - c)} + \Gamma_2(1 - y)^{(c-a-b)}\frac{(c - a)(c - b)(c - a + 1)(c - b + 1)}{(a + b - c - 1)}\right), \end{aligned} \quad (73)$$

where we have used

$$\Gamma_1 = \frac{\Gamma(c)\Gamma(c - a - b - 1)}{\Gamma(c - a)\Gamma(c - b)}, \quad (74)$$

$$\Gamma_2 = \frac{\Gamma(c)\Gamma(a + b - c)}{\Gamma(a)\Gamma(b)}. \quad (75)$$

Similarly,

$$\begin{aligned} (\omega(\mathbf{p}, y) - (1 - y)\omega_0 - y\omega_1)f_2 \approx & (1 - y)\left((\omega_1 - \omega_0) - \frac{2E_0\tau}{\omega_1}P_1\right)\left(\Gamma_1(c - a - b - 1) + e^{-i\tau\omega_1 \ln(1-y)}\Gamma_2\right) \\ & + (1 - y)^2\left(\Gamma_1(c - a - b - 1)\left(\frac{2E_0^2\tau^2\epsilon_1^2}{\omega_1^3} + \frac{ab(\omega_1(\omega_1 - \omega_0) - 2P_1E_0\tau)}{\omega_1(1 + a + b - c)}\right)\right. \\ & \left. + \Gamma_2e^{-i\tau\omega_1 \ln(1-y)}\left(\frac{2E_0^2\tau^2\epsilon_1^2}{\omega_1^3} + \left((\omega_1 - \omega_0) - \frac{2E_0\tau}{\omega_1}P_1\right)\frac{(c - a)(c - b)}{(1 + c - a - b)}\right)\right). \end{aligned} \quad (76)$$

Therefore, the approximate expression for the particle distribution function :

$$\begin{aligned}
f(\mathbf{p}, y) \approx & |N^+(\mathbf{p})|^2 \left[ \frac{2}{\tau} y(a+b-c) \Gamma_2 e^{-i\tau\omega_1 \ln(1-y)} + (1-y) \left[ \Gamma_1 \left( \frac{2}{\tau} yab + i \frac{(c-a-b-1)}{\omega_1} (\omega_1^2 - \omega_1\omega_0 - 2E_0\tau P_1) \right) \right. \right. \\
& \left. \left. + \Gamma_2 e^{-i\tau\omega_1 \ln(1-y)} \left( \frac{2}{\tau} y(c-a)(b-c) + \frac{i}{\omega_1} (\omega_1^2 - \omega_1\omega_0 - 2E_0\tau P_1) \right) \right] + (1-y)^2 \left[ \Gamma_1 \left( \frac{2}{\tau} yab \frac{(1+a)(1+b)}{(2+a+b-c)} \right) \right. \right. \\
& \left. \left. + \frac{i}{\omega_1} \left( \frac{2E_0^2\tau^2\epsilon_\perp^2}{\omega_1^2} (c-a-b-1) - ab(\omega_1^2 - \omega_1\omega_0 - 2E_0\tau P_1) \right) \right] + \Gamma_2 e^{-i\tau\omega_1 \ln(1-y)} \left( \frac{2E_0^2\tau^2\epsilon_\perp^2}{\omega_1^3} + \frac{(c-a)(c-b)}{\omega_1(a+b-c-1)} \right) \right. \\
& \left. \left. \left( \frac{2y}{\tau} \omega_1(c-a+1)(c-b+1) - (\omega_1^2 - \omega_1\omega_0 - 2E_0\tau P_1) \right) \right] \right]^2 \left( \Omega_0 + (1-y)\Omega_1 + (1-y)^2\Omega_2 \right)
\end{aligned} \tag{77}$$

To explore the behavior of the particle distribution function at finite times ( $t > \tau$ ), we aim to express  $f(\mathbf{p}, y)$  in a series involving  $(1-y)$ , as discussed previously (refer to Eq. (72)). We can then consider truncating higher-order terms to simplify the analysis while still capturing essential features. In this context, we focus exclusively on terms up to order  $(1-y)^2$ , disregarding higher-order terms in Eq. (77). This approach is sufficient to explain the interesting results discussed later.

After performing extensive calculations, we derive a simplified expression for the particle distribution function in terms of the small parameter  $(1-y)$ , up to second order. A more detailed evaluation of  $f(\mathbf{p}, y)$  for better clarity is provided in Appendix A 2. This expression is given by:

$$f(\mathbf{p}, y) \approx |N^+(\mathbf{p})|^2 \left( C_0(\mathbf{p}, y) + (1-y)C_1(\mathbf{p}, y) + (1-y)^2C_2(\mathbf{p}, y) \right) \tag{78}$$

where

$$C_0(\mathbf{p}, y) = 4\Omega_0\omega_1^2y^2|\Gamma_2|^2, \tag{79}$$

$$C_1(\mathbf{p}, y) = 4y\Omega_0|\Gamma_1\bar{\Gamma}_2|E_0\tau(P_1 - \omega_1) \cos(\Upsilon) + 4y|\Gamma_2|^2(2\Omega_0(\omega_1^2 - \omega_0\omega_1 + (\omega_1 - P_1)E_0\tau) + \Omega_1\omega_1^2y), \tag{80}$$

$$\begin{aligned}
C_2(\mathbf{p}, y) = & \frac{4E_0^2\tau^2}{\omega_1^2} \Omega_0(P_1 - \omega_1)^2 |\Gamma_1|^2 + |\Gamma_2|^2 \left[ 8\Omega_1y(2E_0\tau(\omega_1 - P_1) - \omega_0\omega_1 + \omega_1^2) \right. \\
& \left. + 4\Omega_2y^2\omega_1^2 + \frac{\Omega_0}{4\omega_1^2(1 + \tau^2\omega_1^2)} \sigma_0 \right] + \frac{|\Gamma_1\bar{\Gamma}_2|(\cos(\Upsilon)\sigma_1 + \sin(\Upsilon)\sigma_2)}{2\omega_1^2(4 + \omega_1^2\tau^2)}
\end{aligned} \tag{81}$$

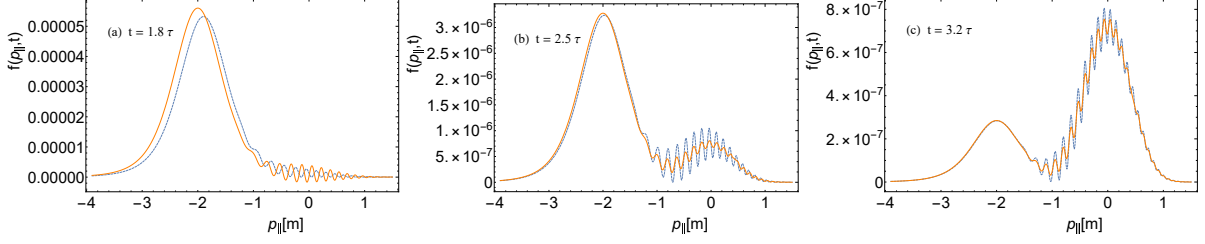


Figure 2: Particle momentum distribution function,  $f(p_{\parallel}, p_{\perp} = 0, t)$ , as a function of  $p_{\parallel}$  for different times with the field parameter  $E_0 = 0.2E_c$  and  $\tau = 10[m^{-1}]$ . Here, the dashed blue line represents the exact result, while the solid orange line is from the approximate calculation. All units are in electron mass units.

Here,  $\Upsilon = \varrho + \tau\omega_1 \ln(1 - y)$ . Also note that  $C_0(\mathbf{p}, y)$ ,  $C_1(\mathbf{p}, y)$ , and  $C_2(\mathbf{p}, y)$  are independent of the function of  $(1 - y)$ .

Next, to verify the accuracy of the approximate expression of the particle distribution function Eq. (78), we will directly compare it with the exact relation (59). For this purpose, we plot the approximate relation (78) against the exact one for  $t > \tau$ , as shown in Fig.2. This comparison is crucial for analytically investigating the momentum spectra at finite time (see Sec. IV B 1). In Fig. 2(a), we observe a small discrepancy between the exact and approximate results, which appears to depend on  $t$ . Consequently, the approximate result provides a highly accurate prediction for  $t \geq 2\tau$ , as shown in Fig. 2. The mean relative error of the approximate result remains below 0.2% at  $t = 2.5\tau$  (see Fig. 2(b)). As time progresses, both approaches yield nearly identical results, as illustrated in Fig. 2(c) for  $t = 3.2\tau$ . Based on the Eq. (78), we analyze the approximate momentum distribution function for longitudinal and transverse momentum, expressed in terms of elementary functions (see sections IV B and IV E).

## IV. RESULTS AND DISCUSSION

### A. Temporal evolution of particle distribution

Quantum vacuum becomes unstable under the action of the external electric field. As a consequence, virtual particle-antiparticle pairs are created in an off-shell mass configuration. These virtual charged particles are accelerated by the electric field to enough energy to become real particles in an on-shell mass configuration. During the action of the external force, pair annihilation process occur simultaneously with the pair creation, giving rise to a dynamical quasiparticle plasma [50]. This results in different states of in and out-vacuum. The most complete description of vacuum pair creation from in-state to out-state is given by the single-particle distribution

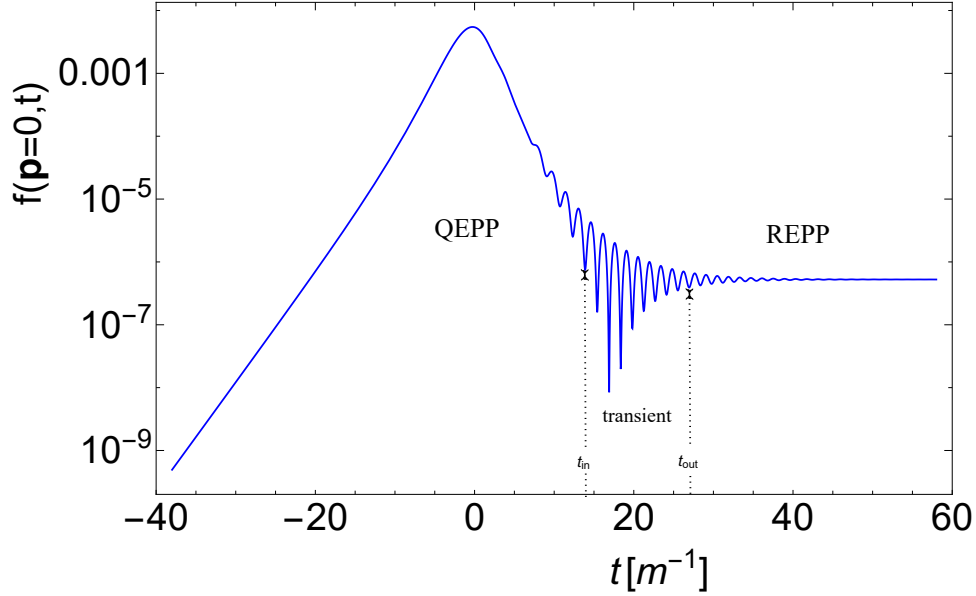


Figure 3: Time evolution of the quasi-particle distribution function for a Sauter-pulsed field for longitudinal momentum  $p_{\parallel} = 0$  and transverse momentum  $p_{\perp} = 0$ . The field parameters are  $E_0 = 0.2E_c$  and  $\tau = 10[m^{-1}]$ , and all the measurements are taken in electron mass units.

function. The time evolution of the single-particle distribution function shows that virtual particle-antiparticle (electron-positron plasma(EPP)) excited from vacuum passes through three different temporal stages: the QEPP stage, the transient stage, and the final REPP in the out-state as pointed by authors of [52, 83] see figure 3. The initial stage QEPP and the final REPP stage are separated by the fast oscillation of EPP by the transient stage. The transient stage is considered to begin at time  $t_{in}$ , where the oscillation of  $f(\mathbf{p}, t)$  first reaches the REPP level. The time  $t_{out}$ , marking the end of the transient stage, is defined as when the average level of the oscillating  $f(\mathbf{p}, t)$  hits the REPP level. After this point, the REPP stage begins. At the REPP stage, quasi-particles become independent, and real particle-antiparticles are observed with a lesser value off than that at the electric field maximum at  $t = 0$ . Each of the three stages contributes to various physical effects, including vacuum polarization effects [85], the emission of annihilation photons from the focal point of colliding laser beams [83, 86–88], birefringence effects [89], and other secondary phenomena. To accurately estimate the contributions of these stages to observable effects, a detailed analysis of each period of the EPP’s evolution is quite helpful. Additionally, due to the uncertainty principle, the description of the system in terms of the time-dependent quasienergy,  $\omega(\mathbf{p}, t)$  is conditional and gains physical significance only in the asymptotic limit as  $t \rightarrow \infty$ . Consequently, the distribution function itself remains somewhat conventional. This feature of the quasiparticle approach has been noted in the literature (see, for example, [52, 65, 90, 91]). However, under certain conditions—such as in sys-

tems confined within a finite spatial region, the evolution of a macroscopic quantum field system in time-dependent external conditions can be monitored at any moment through various means, including radiation into the external region or responses to weak external probes. Examples include experiments on graphene samples under optical excitation [86, 92, 93] and planned experiments to detect an  $e^-e^+$  plasma in the focal spot of high-intensity laser beams [91, 94–96]. In such cases, macroscopic averages are obtained by taking expectation values with initial states and integrating the dynamic characteristics of quasiparticles over momentum space, with the distribution function  $f(\mathbf{p}, t)$  providing statistical weighting. This function acts as a time-dependent bridge between quasiparticle dynamics and physical observables [97]. Therefore, understanding the evolution of the particle distribution function is essential for capturing the underlying dynamical processes.

Since the particle distribution function depends on momentum  $p_{\parallel} = p_3$  parallel to the direction of the electric field and the modulus of the transverse momentum  $p_{\perp} = \sqrt{p_1^2 + p_2^2}$ . Due to the rotation symmetry of the problem about the field axis, one may parameterize the momentum vector as  $\mathbf{p} = (p_1, 0, p_3)$  with the transverse component,  $p_{\perp} = p_1$ , and longitudinal component  $p_{\parallel} = p_3$ . Furthermore, the quasienergy  $\omega(p_{\parallel}, p_{\perp}, t)$ , the transverse energy  $\epsilon_{\perp}(p_{\perp})$  and the longitudinal quasi-momentum  $P(p_{\parallel}, t)$  are defined as

$$\omega(p_{\parallel}, p_{\perp}, t) = \sqrt{\epsilon_{\perp}^2(p_{\perp}) + P^2(p_{\parallel}, t)}, \quad (82)$$

$$\epsilon_{\perp}(p_{\perp}) = \sqrt{m^2 + p_{\perp}^2}, \quad (83)$$

$$P(p_{\parallel}, t) = (p_{\parallel} - eA(t)). \quad (84)$$

Figure 4 illustrates how temporal evolution of the distribution function depends on the momentum value. As depicted in the left panel of Fig. 4, the particle distribution function demonstrates a consistent increase over time within the region of QEPP. Notably, it showcases a higher value for negative longitudinal momentum than positive longitudinal momentum. On closer inspection, it becomes evident that the distribution function reaches its peak precisely when the longitudinal quasi-momentum  $P(p_{\parallel}, t) = 0$ . This particular peak occurrence is influenced by the specific choice of  $p_{\parallel}$  value. After  $t = 0[m^{-1}]$ , where the electric field reaches its maximum value distribution function decreases. After decreasing to a certain value, it shows rapid oscillations and thus transitions from QEPP to the transient region. One observes a gradual narrowing and a disappearance of the fluctuations in the transient regime for higher  $p_{\parallel}$ - value. The transient region appears later for a higher  $p_{\parallel}$ - value. We confirm this by quantifying the period of the transient stage,  $t_{in}$  and  $t_{out}$  as shown in Table 1. The transient stage starts nearly after  $t \approx \tau$  (see Table 1). Afterward, it enters the

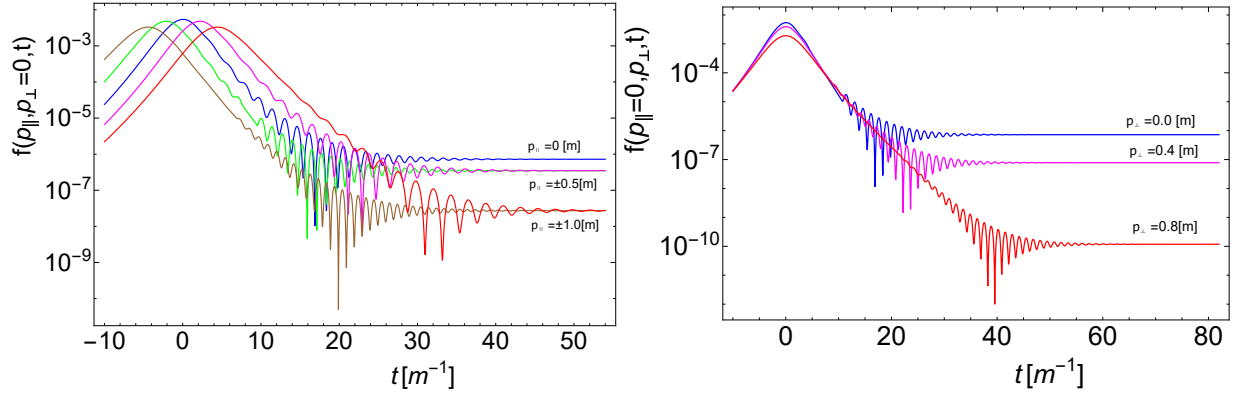


Figure 4: The relationship between momentum and the transient domain's time of occurrence. **Left panel:** for longitudinal momentum. **Right panel:** for transverse momentum. The field parameters are  $E_0 = 0.2E_c$  and  $\tau = 10[m^{-1}]$ . All units are in electron mass units.

REPP stage, during which the distribution function  $f_{out}$  becomes constant.  $f_{out}$  reaches its maximum when  $p_{\parallel} = 0$  and remains the same for positive and negative values of  $p_{\parallel}$ . Next, we examine

$p_{\parallel}[m]$	$t_{in}[m^{-1}]$	$f(p_{\parallel}, t_{in})$	$t_{out}[m^{-1}]$	$f(p_{\parallel}, t_{out})$
0.0	12.57	$7.203 \times 10^{-7}$	24.038	$3.309 \times 10^{-7}$
0.25	13.37	$5.576 \times 10^{-7}$	24.803	$3.112 \times 10^{-7}$
0.50	13.78	$2.242 \times 10^{-7}$	24.320	$1.599 \times 10^{-7}$
0.75	14.53	$7.769 \times 10^{-8}$	25.799	$7.033 \times 10^{-8}$
1.00	16.76	$1.748 \times 10^{-8}$	26.866	$1.082 \times 10^{-8}$

Table I: Transient region time labeled by longitudinal momentum  $p_{\parallel}$ . The time interval during which a strong oscillation emerges in the evolution of the distribution function is referred to as  $t_{in}$ , and  $t_{out}$  marks the point where this vigorous oscillation diminishes, leading to a residual distribution function. The value of transverse momentum is taken to be zero, and all the units are taken in electron mass unit. The field parameters are  $E_0 = 0.2E_c$  and  $\tau = 10[m^{-1}]$ .

the influence of transverse momentum on temporal stages, as depicted in the right panel of Fig. 4. We observe intriguing behavior where the distribution function slowly approaches the REPP stage with a residual value  $f(p_{\parallel} = 0, p_{\perp}, t > t_{out})$ , which is lowest compared to small transverse momentum values  $p_{\perp}$ . The behavior of these stages is primarily determined by the double quasi-energy  $2\omega(p_{\parallel}, p_{\perp}, t)$ . Increasing the transverse momentum value, and thus the transverse energy  $\epsilon_{\perp}(p_{\perp})$ , increases the dynamical energy gap  $2\omega(p_{\parallel}, p_{\perp}, t)$ . Consequently, achieving the on-shell mass configuration takes a longer time, see the right panel of Fig. 4.



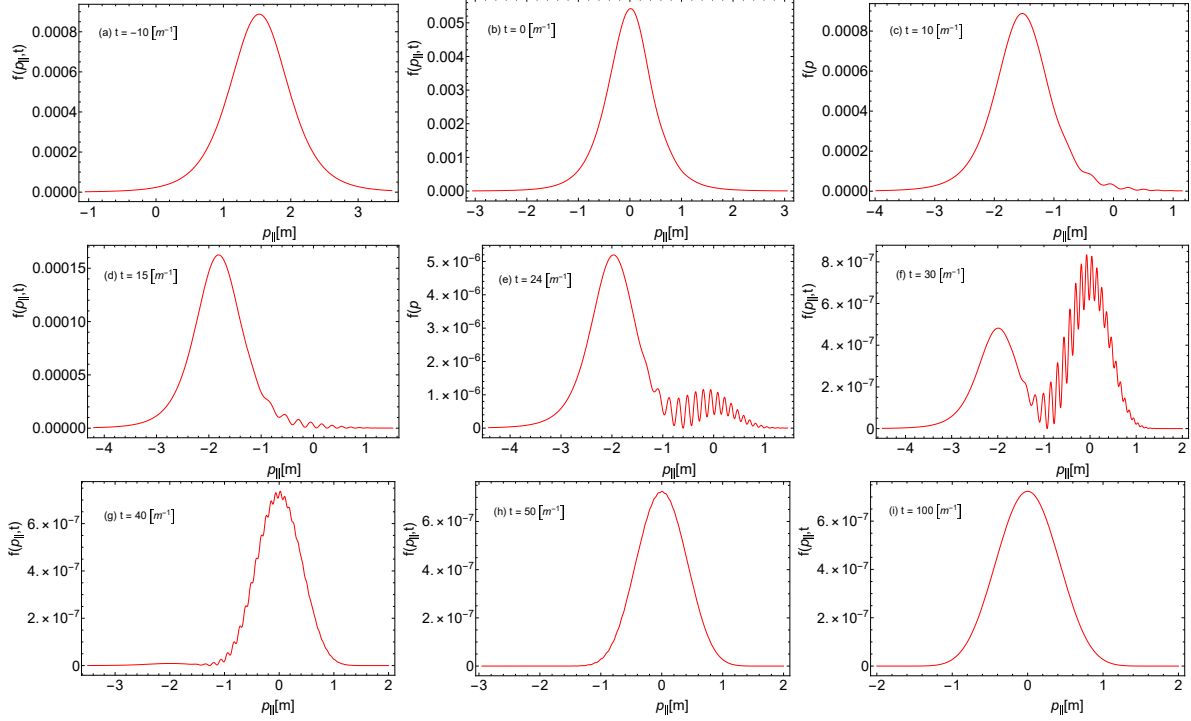


Figure 5: LMS of created particles at different times. The value of transverse momentum is considered to be zero, and all units are in the electron mass unit. The field parameters are  $E_0 = 0.2E_c$  and  $\tau = 10[m^{-1}]$ .

## B. Longitudinal Momentum Spectrum

In this subsection, we discuss the momentum distribution function as defined in Eq. (59). Specifically, we focus on the longitudinal momentum spectra by setting  $p_{\perp} = 0$  and denote the longitudinal momentum distribution function of the produced pairs at any time as  $f(p_{\parallel}, t)$ .

From Figure 5, we see how particle creation proceeds. At early times,  $t = -10[m^{-1}]$  in the QEPP region, when the electric field is increasing, the created particle shows a smooth unimodal-like structure of momentum spectrum with a peak at  $p_{\parallel} \sim 2[m]$ . The electric field propels the newly created particles towards the negative  $z$ -direction. The movement of the distribution function's peak from  $p_{\parallel} = +2$  ( $+eE_0\tau$ ) to  $-2$  ( $-eE_0\tau$ ) can be understood through the concept of longitudinal quasi-momentum,  $P(p_{\parallel}, t)$  as depicted in the time evolution shown in Figs. 5(a) to (c). This phenomenon implies that the longitudinal momentum distribution of the generated particles is expected to span a range of  $\Delta p_{\parallel} = 2$ , with the spread determined by the electric field parameters. At time  $t = 0[m^{-1}]$  where the electric field is maximum, magnitude of the momentum distribution function,  $f(p_{\parallel} = 0, t = 0) \approx 5 \times 10^{-3}$  that follows the tendency  $E^2(t)/8$  [98]. For  $t > 0$ , a reduction in the field strength with a decrease in an intriguing longitudinal momentum distribution function. It rapidly drops to 99.2% of its maximum value, driven by its reliance on the strength of the elec-

tric field at  $t = 10[m^{-1}]$ , as illustrated in Fig. 5(c). Within a narrow range of  $-1 < p_{\parallel} < 1$ , the typically smooth unimodal profile of the longitudinal momentum spectra is disrupted, as depicted in Fig.5(d). Near  $t \approx 2\tau$ , when the electric field's magnitude decreases to approximately 93% of its maximum, a secondary peak appears in the LMS. This peak emerges around  $p_{\parallel} = 0$  and is accompanied by oscillations within a confined range of  $p_{\parallel}$ , as shown in Fig. 5(e). Over time, as the electric field weakens, this secondary peak grows near  $p_{\parallel} = 0$ , while simultaneously, the dominant peak begins to diminish.

At  $t = 3\tau$ , the small peak becomes dominant and exhibits oscillatory behavior near the beginning of the REPP stage, as shown in Fig. 5(f). In this stage, oscillations occur within a narrow range of longitudinal momentum as the electric field decreases to approximately one-hundredth of its maximum magnitude. Intriguingly, these oscillations exhibit asymmetry, with their amplitude more pronounced for negative longitudinal momentum compared to positive longitudinal momentum. Within Fig.5(f), the Gaussian bump centered around  $p_{\parallel} \approx -2[m]$  arises from particles generated during the early stages of the process. Conversely, the dominant peak, characterized by the onset of oscillations, comprises particles formed at later instances, which have encountered relatively less acceleration since their inception. The oscillations in the LMS originate from quantum interference effects, which arise due to the interplay of dynamical processes (or channels) leading to the creation of particles with a given momentum. These time-evolving processes involve inter-band dynamics within the particle momentum representation. To understand this, one can consider multiple channels within momentum space that facilitate particle tunneling [68]. As time progresses, distinct scenarios emerge: (i) At time  $t$ , a particle can tunnel directly, acquiring a momentum  $p'_{\parallel}$ . (ii) In the early stages, a particle with lower momentum ( $p_{\parallel} < p'_{\parallel}$ ) can tunnel first and subsequently accelerate to reach  $p'_{\parallel}$ . (iii) Conversely, a particle initially possessing higher momentum ( $p_{\parallel} > p'_{\parallel}$ ) can tunnel at time  $t_1$  and then decelerate to reach  $p'_{\parallel}$ . When the probability amplitudes of these processes are summed, they exhibit quantum interference effects at time  $t$ .

Around  $t \approx 4\tau$ , a minor peak at  $p_{\parallel} = -2[m]$  is nearly diminished. Only the dominant peak at  $p_{\parallel} = 0$  persists, with a faint onset of oscillatory behavior superimposed on a Gaussian-like structure, as depicted in Figs. 5(g) to (h). The oscillations gradually fade away by  $t = 50[m^{-1}]$ .

In the asymptotic region ( $t = 10\tau$ ), the LMS lacks oscillatory structure for a Sauter pulse, instead forming a single-peaked unimodal structure were reported in [52, 99]. This holds true at asymptotic times ( $t \rightarrow \infty$ ), consistent with Fig. 5(i). To the best of our knowledge, the evolution of the momentum spectrum has only been discussed in the work by Banerjee et al. However, in Ref. [52], the pulse duration of the Sauter pulse was significantly longer than what is considered here.

Due to this larger pulse duration, the quantum interference effects on the momentum spectrum at finite times were not evident in their study. These interference effects were explicitly analyzed only in a recent paper by Diez et al.[69]. In Ref. [69], the authors identified the formation time scale based on quantum interference signatures in the spectra for the field parameters  $E_0 = 0.4E_c$  and  $\tau = 40[m^{-1}]$ . However, we present results on the dynamical aspects of pair production, providing a broader perspective on the time evolution of the process. Additionally, we discuss the phenomenon in the multiphoton region, which is further explored later in section IV B 2.

Certainly, we can identify specific time scales associated with the quantum signature that manifests as oscillations within the LMS of created pairs. Drawing from the emergence of a secondary peak, we define three distinct time scales: (i)  $t_{cp}$  (central peak formation): This time scale is characterized by the emergence of the secondary peak and the beginning of its development, (ii)  $t_{sep}$  (peak separation): At this time, the central peak becomes dominant or the time after the two peaks become distinctly separated, (iii)  $t_{dis}$  (disappearance of oscillation): This indicates the time when the oscillations within the central peak fade away or the time after the primary peak (or the left-side peak) ceases to exist. By identifying and quantifying these time scales, we can better characterize the intricate quantum dynamics reflected in the LMS during the REPP stage. The time scales

$E_0[E_c]$	$t_{cp}[m^{-1}]$	$t_{sep}[m^{-1}]$	$t_{dis.}[m^{-1}]$
0.1	47	57	70
0.2	22	30	50
0.3	15	20	35
0.4	9	15	28
0.5	6	12	23

Table II: The effect of electric field strength  $E_0$  on time scale related to the formation of a central peak. The time scale  $t_{cp}$  appearance of a central peak,  $t_{sep}[m^{-1}]$  when two peaks become distinctly separated, and  $t_{dis.}$  disappearance of the oscillation in LMS.

governing the process are influenced by the electric field strength  $E_0$ , as shown in Table II. A clear pattern emerges—these time scales consistently follow a specific trend as  $E_0$  increases. Notably, for a fixed pulse duration  $\tau$ , key events occur earlier in time with increasing  $E_0$ . In general, these time scales can be quantified in terms of the electric field parameters, specifically  $E_0$  and  $\tau$ . Although a detailed analysis of time scales is beyond the scope of this paper, they can be expressed as:

$$t_{cp} = 0.1698 \tau^{1.102} E_0^{-1.478}, t_{sep} = 0.456 \tau^{1.065} E_0^{-1.059}, t_{dis} = 1.831 \tau^{0.871} E_0^{-0.830}. \quad (85)$$

These relations highlight the nonlinear dependence of each timescale on both the pulse duration and the electric field strength. Our analysis is specifically applicable to Sauter pulsed electric fields

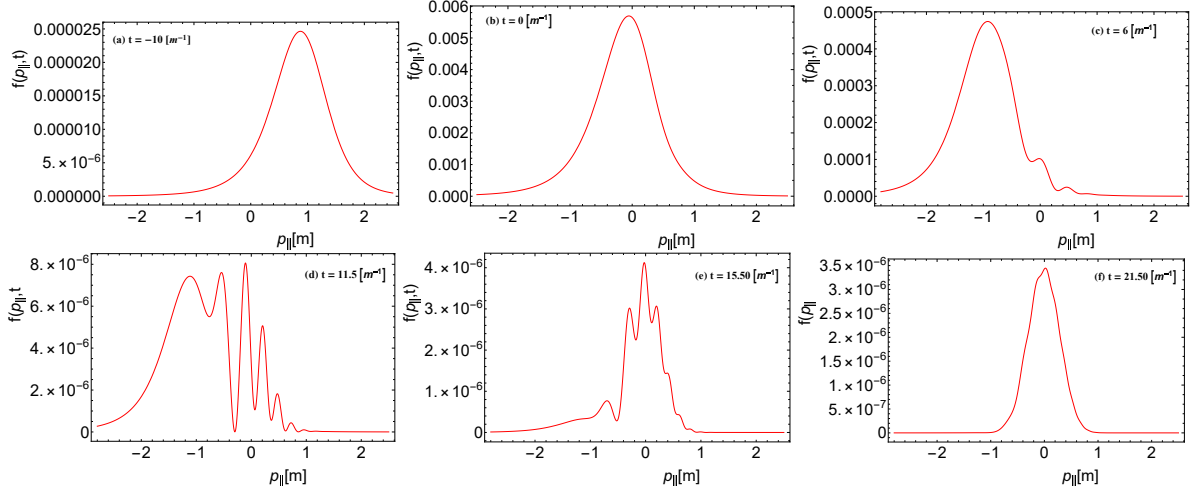


Figure 6: LMS of created particles at different times. The value of transverse momentum is considered to be zero, and all units are in the electron mass unit. The field parameters are  $E_0 = 0.2E_c$  and  $\tau = 5[m^{-1}]$ .

within the range  $5 < \tau < 30$  and  $0.1 < E_0 < 0.5$ . The time scales found in ref. [69] differ from the scaling we have identified in our analysis.

We have not yet discussed the Keldysh parameter,  $\gamma$ , which classifies the pair production process as either a multi-photon or tunneling mechanism. Additionally, we are investigating whether the oscillatory behavior explicitly depends on  $\gamma$ . For this study, we select two different combinations of  $E_0$  and  $\tau$  to vary  $\gamma$  and examine its behavior over a finite time interval. Specifically, we set  $\gamma = 1$ , corresponding to two distinct parameter configurations  $(E_0, \tau)$  associated with the Sauter pulse electric field. It is known that  $\gamma = 1$  represents an intermediate regime involving both tunneling and multi-photon processes, which are inherently nonperturbative [100]. This approach allows us to demonstrate how the same  $\gamma$  value can lead to qualitatively different outcomes in the time evolution of the pair production process.

Figure 6 shows LMS for the Sauter pulse electric field with  $E_0 = 0.2E_c$  and  $\tau = 5[m^{-1}]$ , while Fig.7 shows LMS for field parameter  $E_0 = 0.1E_c$  and  $\tau = 10[m^{-1}]$ . From Figs. 6 (a) to (c) we can see that due to the electric field smooth unimodal peaked profile accelerated towards negative  $z$ -direction and after the pulse duration  $t = 6[m^{-1}]$  we observed smooth profile becomes deformed near the region  $-0.5 < p_{\parallel} < 0.5$ . At  $t = 11.5[m^{-1}]$ , the interference effect is observed, due to which the smooth unimodal peak structure becomes a multi-modal structure as shown in Figs.6(d) and 6(e). That interference effect nearly disappears at  $t \approx 4\tau$ . Comparing Figs. 6(d), (e) and 7(d), (e), clear structural differences emerge. These differences give rise to two qualitatively distinct behaviors at finite times under the condition  $\gamma = 1$ . Notably, the primary factor influencing this behavior at finite times is the pulse duration  $\tau$ .

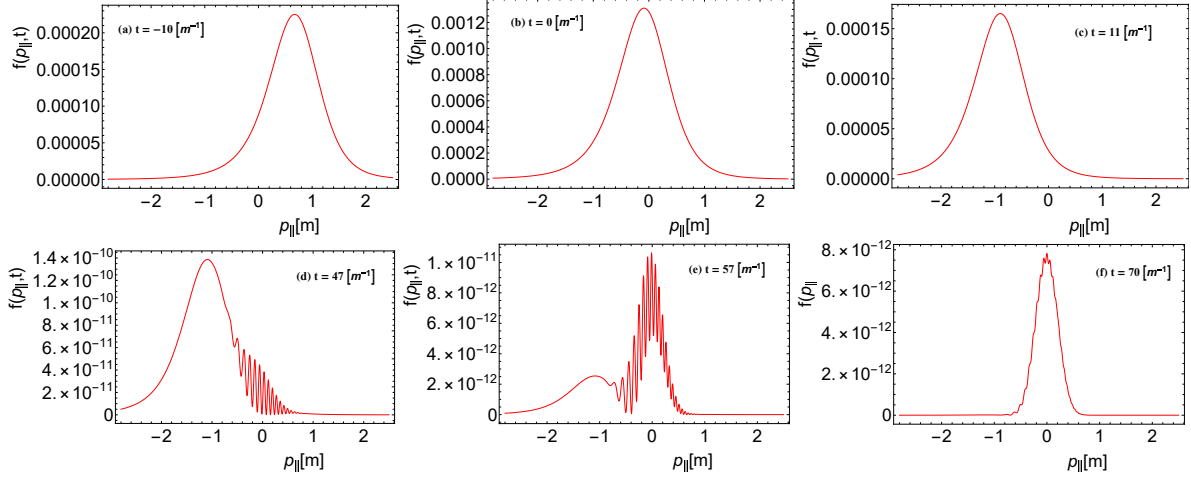


Figure 7: LMS of created particles at different times. The value of transverse momentum is considered to be zero, and all units are in the electron mass unit. The field parameters are  $E_0 = 0.1E_c$  and  $\tau = 10[m^{-1}]$ .

### 1. Approximate expression for longitudinal momentum distribution function

In this subsection, we aim to analyze the oscillatory behavior of the LMS in the late-time limit, specifically for  $t > 2\tau$ . We utilize the previously derived approximate analytical expression for the momentum distribution function Eq.(78). By setting  $p_{\perp} = 0$ , we derive an approximate expression that depends solely on the longitudinal momentum. We express the longitudinal momentum distribution function  $f(p_{\parallel}, y)$  as a series in terms of  $(1 - y)$  up to the second order and neglecting higher orders:

$$f(p_{\parallel}, y) = |N^+(p_{\parallel})|^2 \left( C_0(p_{\parallel}, y) + (1 - y)C_1(p_{\parallel}, y) + (1 - y)^2 C_2(p_{\parallel}, y) \right). \quad (86)$$

Following Eqs. (79), (80), and (81), it is evident that for  $t \gg 2\tau$ , the coefficients of  $(1 - y)$  and  $(1 - y)^2$  can be further approximated by retaining only the dominant contributions and disregarding the others, as follows:

$$C_0(p_{\parallel}, y) \approx 4\omega_1 y^2 (\omega_1 + P_1) |\Gamma_1|^2, \quad (87)$$

$$C_1(p_{\parallel}, y) \approx -4y |\Gamma_1 \overline{\Gamma_2}| \frac{E_0 \tau}{\omega_1} \cos(\Upsilon), \quad (88)$$

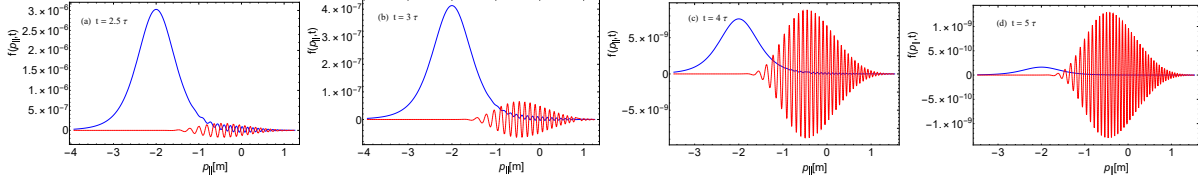


Figure 8: Time evolution of the first and second terms present in the longitudinal momentum distribution function  $f(p_{\parallel}, t)$  (see Eq.(86)) as a function of  $p_{\parallel}$ . Red curve:  $(1-y)C_1$  and Blue curve:  $(1-y)^2C_2$ . The field parameters are  $E_0 = 0.1E_c$  and  $\tau = 10 [m^{-1}]$ .

$$C_2(p_{\parallel}, y) \approx \frac{4E_0^2\tau^2(\omega_1 - P_1)}{\omega_1^2} |\Gamma_1|^2 + 4|\Gamma_1\bar{\Gamma}_2| \cos(\Upsilon) \left[ \omega_0(1 + 3P_1(\omega_1 + P_1)) - \omega_1(3P_1(1 + \omega_1) + 1) \right. \\ \left. + 3E_0\tau((\omega_1 + P_1)^2 - 1) + 2E_0\tau^2 \frac{(\tau\omega_1^4 - 2E_0P_1(4 + 3\tau^2\omega_1^2))}{\omega_1^3(4 + \tau^2\omega_1^2)} \right]. \quad (89)$$

In Figure 8, we illustrate the first-order term  $(1-y)C_1(p_{\parallel}, y)$  and the second-order term  $(1-y)^2C_2(p_{\parallel}, y)$ , derived from the longitudinal momentum distribution function given by Eq. (86). These terms are plotted as functions of longitudinal momentum at different times, allowing for a comparison of their behavior over time. Fig. 8(a), we observe that during earlier times, the term  $(1-y)^2C_2(p_{\parallel}, y)$  is more pronounced compared to  $(1-y)C_1(p_{\parallel}, y)$ . The profile of  $(1-y)^2C_2(p_{\parallel}, y)$  shows a prominent peak around  $p_{\parallel} \simeq -2[m]$ , largely influenced by  $|\Gamma_1|^2$  (refer to Eq. (89)), which peaks near  $p_{\parallel} \simeq -E_0\tau$  depending on parameters  $E_0$  and  $\tau$ . The oscillations observed within  $-1 < p_{\parallel} < 1$  stem from the  $\cos(\Upsilon)$  in the expression for  $(1-y)^2C_2(p_{\parallel}, y)$ , contributing to this oscillatory pattern. Over time, the influence of the first-order term  $(1-y)C_1(p_{\parallel}, y)$  gradually increases compared to earlier times. This term exhibits oscillations within a Gaussian envelope, with the oscillations decaying away from  $p_{\parallel} \approx 0$  (see Figs. 8(b) and (c)). To understand the oscillations and their dependence on  $p_{\parallel}$ -value and the time variable  $y$ , the argument  $\Upsilon$  of the cosine function is approximated as follows:

$$\cos(\Upsilon) = \cos(K_0 + (p_{\parallel} + E_0\tau)(K_1 + K_2(p_{\parallel} + E_0\tau))), \quad (90)$$

where we define

$$K_0 = \pi - \tan^{-1}(\tau) - 2\tau \ln(2) + \tau \ln(1-y) \\ + \frac{1}{2}\tau \left( \ln[-16E_0^2\tau^2] + \sqrt{1 + 4E_0^2\tau^2} + 2E_0\tau \ln[-4E_0\tau] \right), \quad (91)$$

$$K_1 = \frac{E_0 \tau^2}{\sqrt{1 + 4E_0^2 \tau^2}} \ln \left[ \frac{\sqrt{1 + 4E_0^2 \tau^2} - 1}{\sqrt{1 + 4E_0^2 \tau^2} + 1} \right], \quad (92)$$

$$K_2 = \frac{\tau}{4} \left( 2 - \frac{2}{1 + \tau^2} - \frac{2}{1 + 4E_0^2 \tau^2} + 2 \ln [E_0 \tau] + 2 \ln (1 - y) + \frac{1}{(1 + 4E_0^2 \tau^2)^{3/2}} \ln \left[ \frac{\sqrt{1 + 4E_0^2 \tau^2} - 1}{\sqrt{1 + 4E_0^2 \tau^2} + 1} \right] \right), \quad (93)$$

up to quadratic term and neglecting other higher-order.

According to Eq. (90), the oscillation frequency depends on  $p_{\parallel}$ , time variable  $(1 - y)$ , and the field parameters  $(E_0, \tau)$ . Near  $p_{\parallel} = -E_0 \tau$ , the cosine oscillation flattens out, and its behavior near this point changes over time. However, regular oscillations occur at other points (see Fig. 9).

In addition to the cosine function within  $C_1(p_{\parallel}, y)$ , the coefficient function  $A_{C1}(p_{\parallel})$  also significantly influences the observed oscillatory effect

$$A_{C1}(p_{\parallel}) = \frac{4|\Gamma_1 \bar{\Gamma}_2| E_0 \tau}{\sqrt{1 + (p_{\parallel} + E_0 \tau)^2}} \quad (94)$$

The combined effect of  $\cos(\Upsilon)$  and  $A_{C1}(p_{\parallel})$  is observed in the spectra, we compare their behaviors by plotting them for the late-time limit, as shown in Fig.9. The function  $A_{C1}(p_{\parallel})$  can be approximated as a Gaussian-like profile:

$$A_{C1}(p_{\parallel}) \approx \frac{2E_0 \tau e^{\frac{\pi x}{2}(2E_0 \tau - \sqrt{1+(p_{\parallel}-E_0 \tau)^2} - \sqrt{1+(p_{\parallel}+E_0 \tau)^2})}}{(1 + (p_{\parallel} + E_0 \tau)^2) \sqrt{1 + \tau^2(1 + (p_{\parallel} + E_0 \tau)^2)}} \left( 1 + (p_{\parallel} - E_0 \tau)^2 + \sqrt{1 + (p_{\parallel} - E_0 \tau)^2} (-p_{\parallel} + E_0 \tau) \right) \quad (95)$$

$$\left. \frac{\partial A_{C1}}{\partial p_{\parallel}} \right|_{E_0=0.2, \tau=10} = 0 \quad (96)$$

This leads us to find that the maxima occur at approximately  $p_{\parallel} \approx -0.6[m]$ . The function exhibits a nearly Gaussian-like structure. Figure 9 illustrates that the function  $C_1(p_{\parallel}, y)$  combines a smooth Gaussian-like envelope,  $A_{C1}(p_{\parallel})$ , with an oscillatory function,  $\cos(\Upsilon)$ . This function displays a clear pattern where the amplitude decreases smoothly as one moves away from the peak of the Gaussian envelope. The Gaussian envelope,  $A_{C1}(p_{\parallel})$ , ensures a gradual decline in the function's

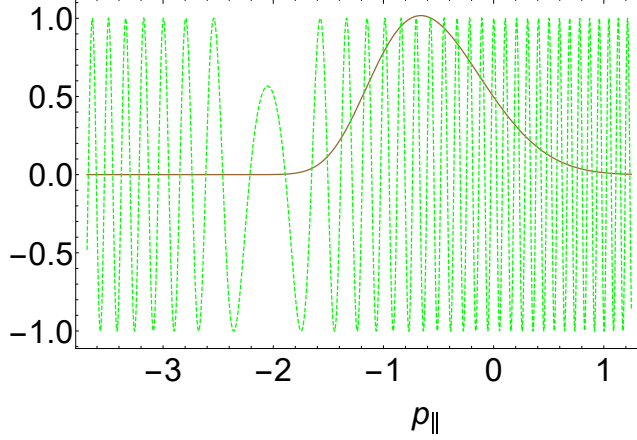


Figure 9: The individual components of  $C_1(p_{\parallel}, y)$  as defined in (88), as a function of longitudinal momentum, depicted for  $y \simeq 1$ ,  $E_0 = 0.2E_c$ , and  $\tau = 10[m^{-1}]$ . The green dashed curve represents  $\cos(\Upsilon)$ , and the brown curve represents the amplitude function ( $A_{C1}$ ).

amplitude, while the oscillatory component introduces periodic variations. The frequency and amplitude of these oscillations depend on field parameters ( $E_0, \tau$ ), and  $p_{\parallel}$ .

At  $t = 4\tau$ , the magnitude of the first-order term  $(1-y)C_1(p_{\parallel}, y)$  dominates over the second-order term  $(1-y)^2C_2(p_{\parallel}, y)$  as seen in Fig.8(c). The second-order term diminishes at  $t = 5\tau$  (see Fig.8(d)). It's worth noting that both orders have a  $(1-y)$  factor, which contributes to the distribution function. However, this contribution gradually decreases as time progresses, becoming less important in the late-time limit  $y \simeq 1$ . At  $t \gg 2\tau$ , the onset of oscillations in the Gaussian-like structure can be explained by the zeroth and first-order terms of the power series expansion of  $f(p_{\parallel}, y)$ .

In figure 10, the comparison of  $C_1(p_{\parallel}, y)$ ,  $C_0(p_{\parallel}, y)$ , and  $C_0(p_{\parallel}, y) + (1-y)C_1(p_{\parallel}, y)$  is shown to identify which order is responsible for the oscillatory features of LMS at  $t \geq 3\tau$ . At  $t = 3\tau$ ,  $C_0(p_{\parallel}, y)$  exhibits a smooth single peak located at  $p_{\parallel} = 0$ , while  $(1-y)C_1(p_{\parallel}, y)$  shows oscillatory behavior within the small range  $-1 < p_{\parallel} < 1$ . The combined behavior resembles a smooth Gaussian structure with onset oscillations contributing to the distribution function, as confirmed by Fig. 10(a). As time progresses, the oscillation amplitude decreases due to the presence of the  $(1-y)$  factor in the first-order term, reducing its impact (see Fig. 10(b)). Eventually,  $C_0(p_{\parallel}, y)$  dominates and explains the distribution function's behavior at asymptotic times as shown in Fig.10(c). On careful examination of the individual components of the longitudinal momentum distribution function (86), we observe that during electron-positron formation at  $t > 2\tau$ , the second-order term  $((1-y)^2C_2(p_{\parallel}, y))$  is responsible for the primary peak located at  $p_{\parallel} \approx -2[m]$  (see Fig.5). As time progresses, this primary peak diminishes, and a secondary peak at  $p_{\parallel} = 0$  starts to build up due to the first-order term  $((1-y)C_1(p_{\parallel}, y))$  and zeroth-order term  $C_0(p_{\parallel}, y)$ , which are responsible



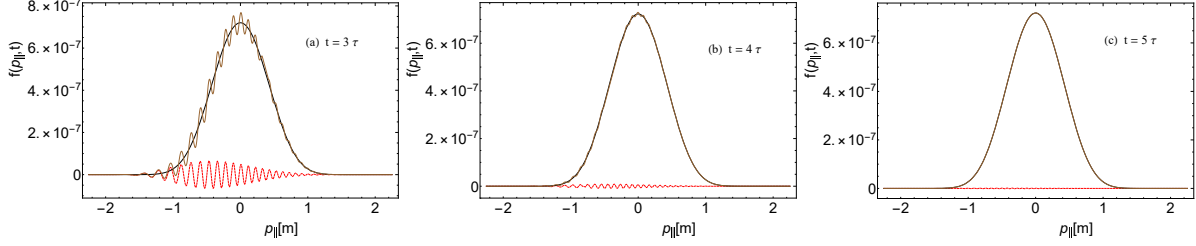


Figure 10: The zeroth and first-order terms defined in Eq.(86) as a function of the longitudinal momentum at different times. Black curve:  $C_0(p_{\parallel}, y)$  and Red curve :  $(1 - y)C_1(p_{\parallel}, y)$ , Brown curve:  $(C_0(p_{\parallel}, y) + (1 - y)C_1(p_{\parallel}, y))$ . The field parameters are  $E_0 = 0.2E_c$  and  $\tau = 10[m^{-1}]$ .

for the onset oscillation on that peak. As time progresses towards infinity,  $C_1(p_{\parallel}, y)$  leads to suppression. Consequently, we observe only a secondary peak due to the dominance of the  $C_0(p_{\parallel}, y)$  zeroth-order term( see Fig.5). Since the component  $(1 - y)C_1(p_{\parallel}, y)$  represents an oscillatory finite function whose magnitude depends on  $t$ , the magnitude of this function plays a crucial role in determining the dynamics of  $f(p_{\parallel}, t)$  in  $p_{\parallel}$ -space at finite times.

Now, we find out an asymptotic expression for the distribution function in the limit  $y \approx 1$ . At this stage, the second and first-order terms become negligible, leaving only the zeroth-order term  $C_0(p_{\parallel}, y \rightarrow 1)$  surviving:

$$\begin{aligned} f(p_{\parallel}, y \rightarrow 1) &= |N^+(p_{\parallel})|^2 C_0(p_{\parallel}, y \rightarrow 1) \\ &= 4\omega_1 |N^+(p_{\parallel})|^2 (\omega_1 + P_1) |\Gamma_1|^2 \end{aligned} \quad (97)$$

We can write the expression for the distribution function at asymptotic times as follows:

$$f(p_{\parallel}, y \rightarrow 1) = \frac{2 \sinh\left(\frac{\pi\tau(2E_0\tau + \omega_0 - \omega_1)}{2}\right) \sinh\left(\frac{\pi\tau(2E_0\tau - \omega_0 + \omega_1)}{2}\right)}{\sinh(\pi\tau\omega_0) \sinh(\pi\tau\omega_1)}. \quad (98)$$

The function  $f(p_{\parallel}, y \rightarrow 1)$  aligns with earlier findings on the asymptotic particle distribution function [81, 101]. By approximating the  $\omega_1$  and  $\omega_0$  as series expansions around  $p_{\parallel} = 0$  up to quadratic order and neglecting higher order and further simplifying, we get

$$f(p_{\parallel}) \approx 2e^{2\pi\tau(E_0\tau - \sqrt{1+E_0^2\tau^2})} \exp\left\{-\pi \frac{p_{\parallel}^2 \tau}{(1 + E_0^2\tau^2)^{3/2}}\right\}. \quad (99)$$

Next, we analyze the qualitative picture of LMS at finite time for the Keldysh parameter  $\gamma = 1$ , as discussed in the previous subsection. This analysis uses two different configurations of parameters,  $E_0$  and  $\tau$ , to illustrate their impact on the finite-time behavior of LMS. We observe that LMS

exhibits multi-peaks for  $\tau = 5 [m^{-1}]$  and a bimodal Gaussian-like profile with onset oscillations for  $\tau = 8 [m^{-1}]$ , as depicted in Fig. 7. This trend can be understood through the presence of  $\cos(\Upsilon)$  in the first and second-order terms of the approximate distribution function relation (86). We approximate the argument  $\Upsilon$  using a series expansion around  $p_{\parallel} = 0$  as follows:

$$\begin{aligned} \Upsilon \approx & \pi - \tan^{-1}\left(\frac{\tau}{\gamma} \sqrt{1 + \gamma^2}\right) + \frac{\tau}{\gamma} \ln\left(\frac{\sqrt{1 + \gamma^2} + 1}{\sqrt{1 + \gamma^2} - 1}\right) + \sqrt{1 + \gamma^2} \ln\left(\frac{\gamma^2(1 - y)}{1 + \gamma^2}\right) \\ & + p_{\parallel} \frac{\tau}{\sqrt{1 + \gamma^2}(\tau^2 + \gamma^2(1 + \tau^2))} \left( \ln\left(\frac{(1 - y)}{1 + \gamma^2}\right) (\gamma^2(1 + \tau^2) + \tau^2) - \gamma^2 \right) \\ & + p_{\parallel}^2 \sqrt{1 + \gamma^2} \gamma \tau \left( \frac{\gamma^2 \tau^2 (2 + \gamma^2 - \gamma^4) - \gamma^6}{(\gamma^2(1 + \tau^2) + \tau^2)^2} - 2 + \frac{\gamma^2}{2(1 + \gamma^2)} \ln\left(\frac{\gamma^2(1 - y)}{1 + \gamma^2}\right) \right). \end{aligned} \quad (100)$$

Eq. (100) indicates that the cosine function's argument depends on the pulse duration  $\tau$  and the Keldysh parameter  $\gamma$ . When  $\gamma$  is fixed, the frequency of momentum oscillations is determined by  $\tau$  alone. As  $\tau$  decreases, these oscillations occur less frequently, leading to visible patterns in the momentum spectrum, as illustrated in Fig. 6. According to Eq. (100), reducing  $\tau$  results in fewer oscillations, which manifests as a multi-peak structure in the spectrum.

## 2. LMS in the multi-photon regime

In this subsection, we explored the LMS of the created particle in the multiphoton regime. We choose the parameters of the laser pulse in such a way that the Keldysh parameter,  $\gamma \gg 1$ . Figure 11 shows LMS for short pulse-duration  $\tau = 4 [m^{-1}]$  and  $E_0 = 0.1 E_c$ . The Keldysh parameter, in this case, is close to 2.5, i.e.,  $\gamma \gg 1$  corresponds to  $n^{\text{th}}$  order perturbation theory, with  $n$  being the minimum number of photons to be absorbed in order to overcome the threshold energy for pair creation  $n\omega > 2m$ . In the early time of the creation of pairs at  $t = -4 [m^{-1}]$  spectrum has a unimodal Gaussian-like profile peak at  $p_{\parallel} \simeq -0.4 [m]$ , and as time proceeds, we see shifting of peak  $p_{\parallel} \simeq -eE_0\tau$  to  $p_{\parallel} \simeq eE_0\tau$  due to the action of force and its peak value shows the maximum value for  $t = 0$ , i.e.,  $f(p_{\parallel} = 0, t = 0) = 1.4 \times 10^{-3}$  as seen in figure 11 (a-c). However, the previously smooth and unimodal spectrum now exhibits slight modulation at  $t = 9 [m^{-1}]$ . However, at  $t = 12 [m^{-1}]$  spectrum has a quad-modal profile, as seen in Fig.11(e). The central peak, which is located at  $p_{\parallel} = 0$ , is much more prominent than the two unequal peaks at  $p_{\parallel} \simeq \pm 0.4 [m]$  and another very small peak at  $p_{\parallel} \simeq 0.7 [m]$ . Fig. 11(f-g) shows the merging of those multimodal peaks as a result of the fading of different peaks that occur and the single smooth Gaussian peaks observed at  $t > 5\tau$  as shown in figure 11 (h-i).

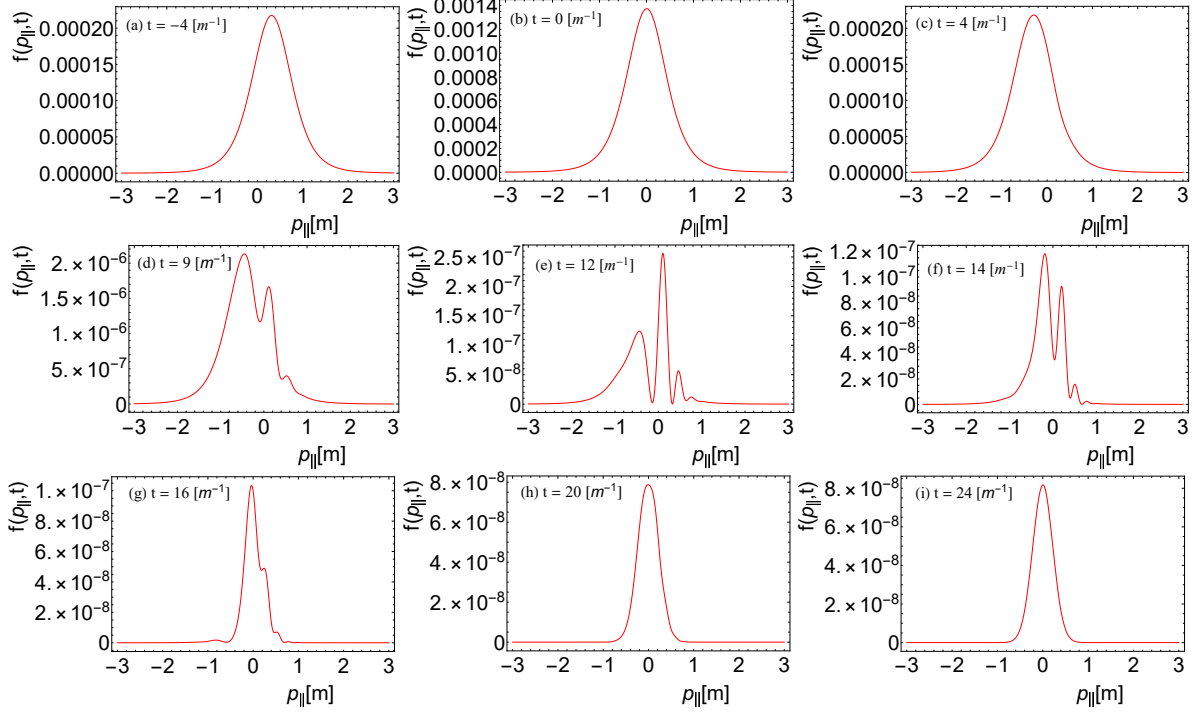


Figure 11: LMS of created particles at different times. The value of transverse momentum is considered to be zero, and all units are in the electron mass unit. The field parameters are  $E_0 = 0.1E_c$  and  $\tau = 4[m^{-1}]$ .

An interesting qualitative contrast becomes evident when comparing the previous scenario with  $\gamma = 0.5$  to the current situation. The presented figure illustrates this distinct behavior. Notably, a multi-modal pattern emerges at a specific moment, characterized by the presence of more than two peaks, occurring approximately at  $3\tau$ . As discussed in the previous section, the characteristic features of the LMS can be mathematically explained using a simple approximate distribution function, as shown in Eq. (86). A similar analysis can help us understand the behavior of the multiple peaks observed in the LMS at finite time. In the multi-photon case, where  $E_0\tau < 1$ , the first-order term becomes

$$C_1(p_{\parallel}, y) \approx A_{C1}(p_{\parallel}) \cos(Y), \quad (101)$$

with,

$$A_{C1}(p_{\parallel}) \approx \frac{1}{2} e^{\frac{\pi}{2}(E_0\tau(2-E_0\tau)-2)} e^{p_{\parallel}^2(1-E_0^2\tau^2)} (4 + 2E_0\tau(2 - E_0\tau - 2E_0^2\tau^2)) + p_{\parallel}^2(-2 + E_0\tau(12 + 57E_0\tau)) + 2p_{\parallel}(-2 - 10E_0\tau - 6E_0^2\tau^2 + 15E_0^3\tau^3) \quad (102)$$

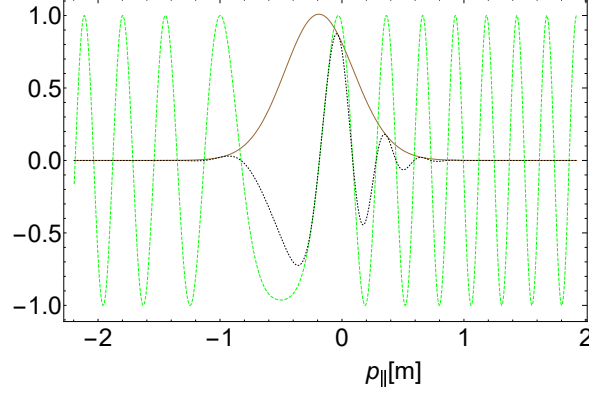


Figure 12: The first order term,  $C_1(p_{\parallel}, y)$ , and its individual components as defined in Eq.(101), as a function of longitudinal momentum, depicted for  $y \simeq 1$ ,  $E_0 = 0.1E_c$ , and  $\tau = 4[m^{-1}]$ . The green dashed curve represents  $\cos(\Upsilon)$ , the brown curve represents the amplitude function ( $A_{C_1}$ ), and the black dotted curve represents  $C_1(p_{\parallel}, y)$ .

$$\begin{aligned} \Upsilon \approx & E_0\tau^2 \ln\left(\frac{E_0\tau + \sqrt{1 + E_0^2\tau^2}}{-E_0\tau + \sqrt{1 + E_0^2\tau^2}}\right) + \tau\sqrt{1 + E_0^2\tau^2} \ln\left(\frac{(1-y)}{1 + E_0^2\tau^2}\right) \\ & + p_{\parallel} \frac{E_0\tau^2}{\sqrt{1 + E_0^2\tau^2}} \ln\left(\frac{E_0^2\tau^2(1-y)}{(1 + E_0^2\tau^2)}\right) + \frac{p_{\parallel}^2\tau}{2(1 + E_0^2\tau^2)^{3/2}} \left(-2E_0^2\tau^2 + \ln\left(\frac{(1-y)}{(1 + E_0^2\tau^2)}\right)\right) \end{aligned} \quad (103)$$

In Fig. 12, for the given field parameters, a decrease in the oscillation frequency of the  $\cos(\Upsilon)$  function is observed compared to the previous case with  $\gamma = 0.5$ . As the oscillation frequency decreases for smaller values of  $\tau$ , this is reflected in the momentum Spectrum. Near  $p_{\parallel} = -E_0\tau$ , the cosine function behaves irregularly, flattening out and oscillating regularly away from this point. The function  $A_{C_1}(p_{\parallel})$  plays a crucial role here, resembling a Gaussian single-peak structure with its peak located at  $p_{\parallel} = -0.1[m]$ , as represented by the brown curve in Fig. 12. The width of the Gaussian envelope and its peak location affect the overall behavior of  $C_1(p_{\parallel}, y)$ . Since the field parameters ( $E_0, \tau$ ) influence the occurrence of the peak in the function  $A_{C_1}$ , they also affect the behavior of the  $\cos(\Upsilon)$  function. Consequently, the presence of oscillations within the envelope depends on the field parameters. The appearance of multiple peaks in the spectrum is the combined effect of the oscillation of the cosine function and the function  $A_{C_1}(p_{\parallel})$ . As seen in Fig. 12, the black dotted curve represents  $C_1(p_{\parallel}, y)$ , which shows fewer irregular oscillations. In the long-time limit, the first-order term contribution becomes suppressed, and only the zeroth-order term,  $C_0(p_{\parallel}, y)$ , becomes dominant and governs  $f(p_{\parallel}, y \rightarrow 1)$ . As a result, the multi-modal pattern gradually dissipates, eventually leading to a singular smooth peak above  $t > 5\tau$ .

### C. Vacuum Polarisation and depolarisation function

For a better understanding of the phenomenon of particle creation under a strong electric field, we will also trace the evolution of the vacuum polarization function  $u(p_{\parallel}, t)$ , and its counterterm  $v(p_{\parallel}, t)$ , which governs the depolarization. Figure 13 shows the time evolution of  $u(p_{\parallel}, t)$  and  $v(p_{\parallel}, t)$  for different values of  $p_{\parallel}$  at zero transverse momentum. Due to pair annihilation being stronger than pair creation in the early times, the depolarisation function  $v(p_{\parallel}, t)$  dominates over  $u(p_{\parallel}, t)$  [Figs. 13(a) and (c)]. It appears that in the polarization function, there is a sinusoidal function behavior. On the other hand, the depolarization function  $v(p_{\parallel}, t)$  shows an unimodal Gaussian peak structure in its temporal evolution. Both  $u(p_{\parallel}, t)$  and  $v(p_{\parallel}, t)$  show oscillations with varying amplitudes during the initial transient stage. These oscillations are particularly pronounced when  $p_{\parallel} = 0[m]$ , as evident from Figs. 13(a) and (c). As time progresses, irregular oscillations are observed in the transient stage. However, the oscillations become regular and stable as the system enters the REPP stage. Both  $u(p_{\parallel}, t)$  and  $v(p_{\parallel}, t)$  now exhibit regular oscillations centered around the zero value. Moreover, as the momentum value  $p_{\parallel}$  increases, the amplitudes of these oscillations diminish, as shown in Fig. 13(b) and (d). During the REPP stage, one interesting finding is that  $u(p_{\parallel}, t)$  and  $v(p_{\parallel}, t)$  demonstrate balancing behavior characterized by similar oscillatory patterns. This balance results from the formation of real electron-positron pairs.

#### 1. Momentum Spectra of $u(p_{\parallel}, t)$ and $v(p_{\parallel}, t)$

The longitudinal momentum significantly impacts the vacuum polarization function's qualitative traits. To understand its dependence on  $p_{\parallel}$ , we comprehensively analyze the momentum spectra of both  $u(p_{\parallel}, t)$  and its associated counter term  $v(p_{\parallel}, t)$ . Figure 14 shows the momentum spectra of  $u(p_{\parallel}, t)$  and  $v(p_{\parallel}, t)$ . In the initial stages of particle formation, specifically at  $t < 0$ ,  $u(p_{\parallel}, t)$  and  $v(p_{\parallel}, t)$  display asymmetric Gaussian peaks with roughly similar profiles. During this time,  $v(p_{\parallel}, t)$  dominates over  $u(p_{\parallel}, t)$ . Upon closer examination, it becomes evident that the peaks occur at different positions around  $p_{\parallel} \approx 1[m]$ , as illustrated in Fig. 14(a). At  $t = 0[m^{-1}]$ , the initial Gaussian-like structure of  $u(p_{\parallel}, t)$  deformed, becoming bi-modal asymmetric structure. The spectrum  $u(p_{\parallel}, t)$  exhibits a peak at  $p_{\parallel} \approx -0.35[m]$  and a dip at  $p_{\parallel} \approx +0.35[m]$ . This indicates a significant asymmetry in the function. On the other hand, the  $v(p_{\parallel}, t)$  spectrum maintains its Gaussian-like unimodal profile, with a peak at  $p_{\parallel} = 0$ . During this stage, while the shape of  $u(p_{\parallel}, t)$  undergoes considerable changes and becomes asymmetric, the overall form of  $v(p_{\parallel}, t)$  remains unchanged. Due to the force factor “ $eE(t)$ ” and corresponding longitudinal quasi-momentum  $P(p_{\parallel}, t) = (p_{\parallel} - eA(t))$ , the

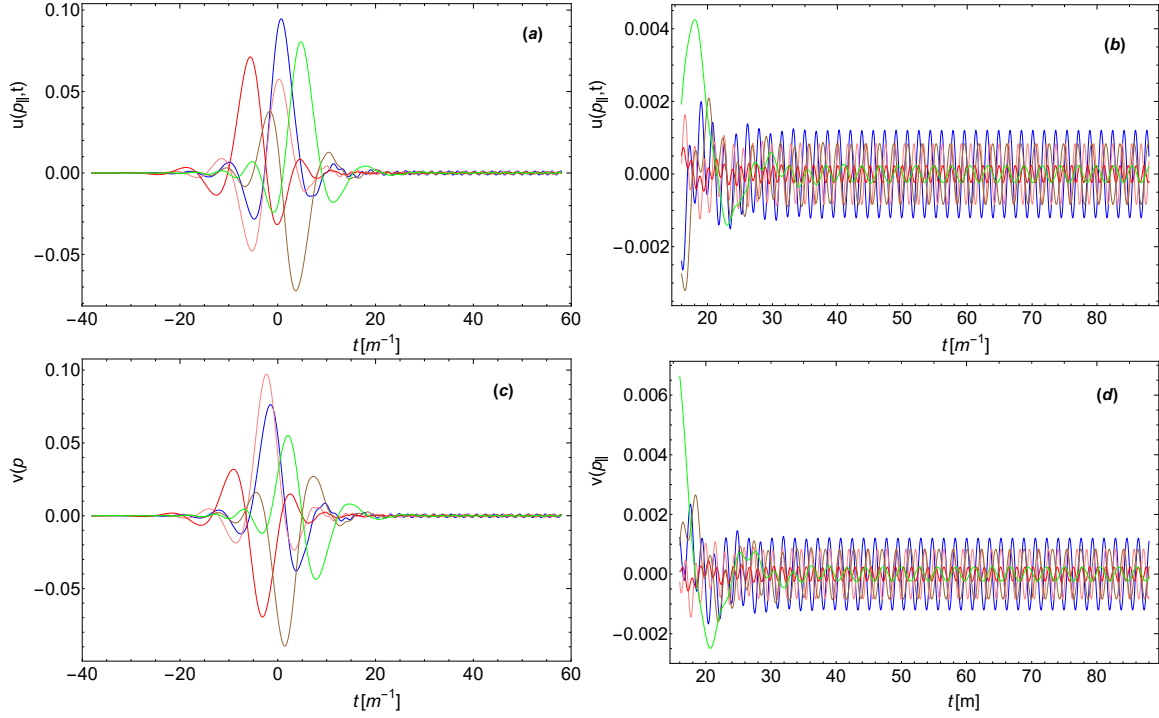


Figure 13: Evolution of  $u(p_{\parallel}, t)$  and  $v(p_{\parallel}, t)$  for  $p_{\parallel} = 0$  (blue),  $0.5$  (pink),  $-0.5$  (brown),  $1$  (red), and  $-1$  (green) with  $p_{\perp} = 0$ ,  $E_0 = 0.2E_c$ , and  $\tau = 10 [m^{-1}]$ . All the measurements are taken in electron mass units.

spectrum moved to the left side of the origin, and its peak now located at  $p_{\parallel} \approx -2[m]$  for  $v(p_{\parallel}, t)$  whereas small dip for  $u(p_{\parallel}, t)$  with some disruption in the tail ( $-1 < p_{\parallel} < 1$ ) as shown in the Figs.14(c-d) near to the transient stage. At  $t = 24 [m^{-1}]$ , we observe two distinct structures in the polarization and depolarization functions. The first structure appears at  $p_{\parallel} = -2 [m]$  due to earlier particle creation and annihilation events. The second structure, within  $-1 < p_{\parallel} < 1$ , exhibits varying amplitude oscillations, with the maximum occurring at zero longitudinal momentum. At this stage,  $u(p_{\parallel}, t)$  and  $v(p_{\parallel}, t)$  compete, as shown in Fig.14(d) and (e). As we approach the REPP stage,  $u(p_{\parallel}, t)$  and  $v(p_{\parallel}, t)$  exhibit a single oscillating structure resembling a sine or cosine function with varying amplitude. The maximum now appears near  $p_{\parallel} = 0$ , dominating compared to the secondary peak (and dip for  $u(p_{\parallel}, t)$ ) previously present at  $p_{\parallel} \approx -2 [m]$ . As time progresses further, this left-side structure slowly vanishes, as shown in Figs. 14(e) and (f). Eventually, as  $A(t)$  reaches a constant value, a balance is achieved between the processes of particle creation and annihilation, as depicted in Fig.14(g). In the late REPP stage, where the particle distribution function  $f(p_{\parallel}, t)$  is constant, the polarization function  $u(p_{\parallel}, t)$  is balanced by its counterpart  $v(p_{\parallel}, t)$ . This results in very regular and rapid oscillations with varying amplitude within the Gaussian envelope, as explicitly shown in Figs. 14(h-i). The overall behavior observed in both  $u(p_{\parallel}, t)$  and  $v(p_{\parallel}, t)$  during this process provides valuable insights into the complex dynamics of particle-antiparticle pair creation

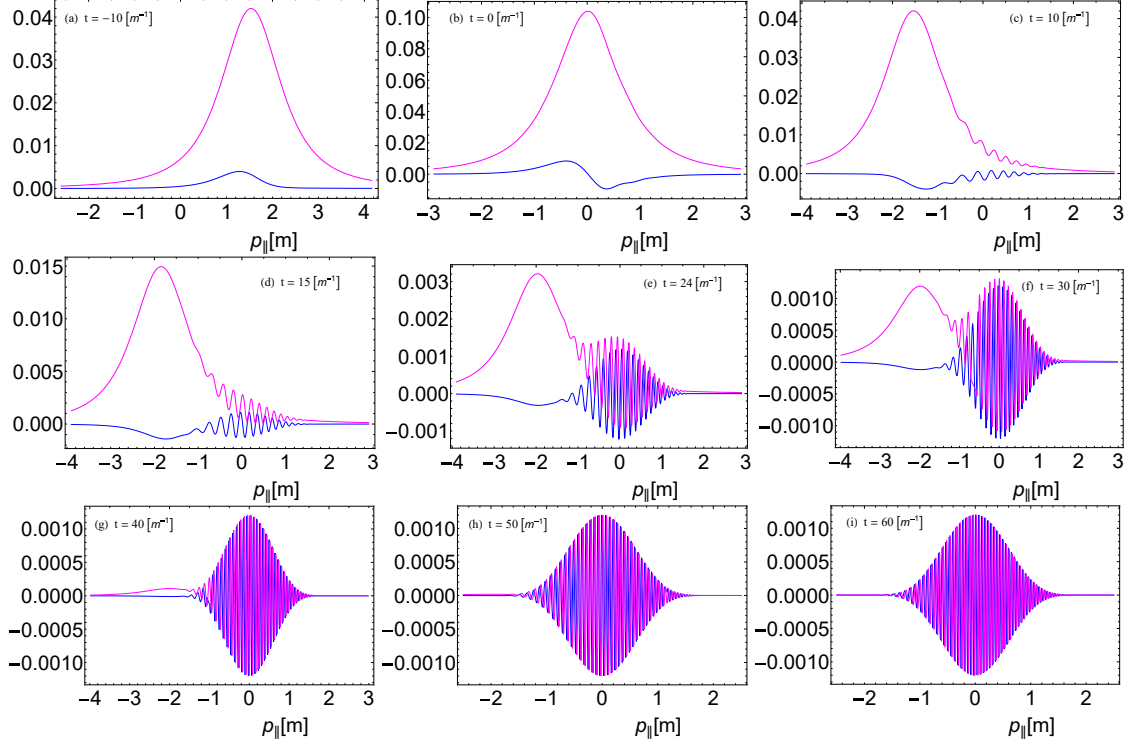


Figure 14: Momentum spectrum at finite time. Blue curve: polarization function ( $u(p_{\parallel}, t)$ ) and Magenta curve: de-polarization function ( $v(p_{\parallel}, t)$ ). The transverse momentum is considered zero, and all units are in electron mass units. The field parameters are  $E_0 = 0.2E_c$  and  $\tau = 10 [m^{-1}]$ .

and annihilation under the influence of the electric field.

## 2. Examining quantum interference effect in LMS of $f(p_{\parallel}, t)$ : Role of Vacuum Polarization and Depolarization Functions

During the formation of electron-positron pairs from the quantum vacuum, several processes can take place. Electrons are predominantly created and annihilated simultaneously, resulting in electron acceleration and deceleration throughout the formation of real  $e^-e^+$  independent pairs from the virtual  $e^-e^+$  pairs. In these scenarios, the polarization functions  $u(p_{\parallel}, t)$  and its counterpart  $v(p_{\parallel}, t)$  are responsible for the acceleration and deceleration of electrons, respectively. In this context, an electron is typically created in the direction of the external field with positive momentum and is subsequently decelerated. As soon as  $p_{\parallel} < 0$ , the electron may be annihilated again. These processes can be understood in terms of  $u(p_{\parallel}, t)$  and  $v(p_{\parallel}, t)$ , which represent the acceleration and deceleration of electrons, respectively.

In quasi-momentum space, there are many possibilities that particles can find with specific momentum  $p_0$  with time  $t_0$ . Suppose particles at a lower momentum level with  $(p_0 - \delta p_0)$  in earlier

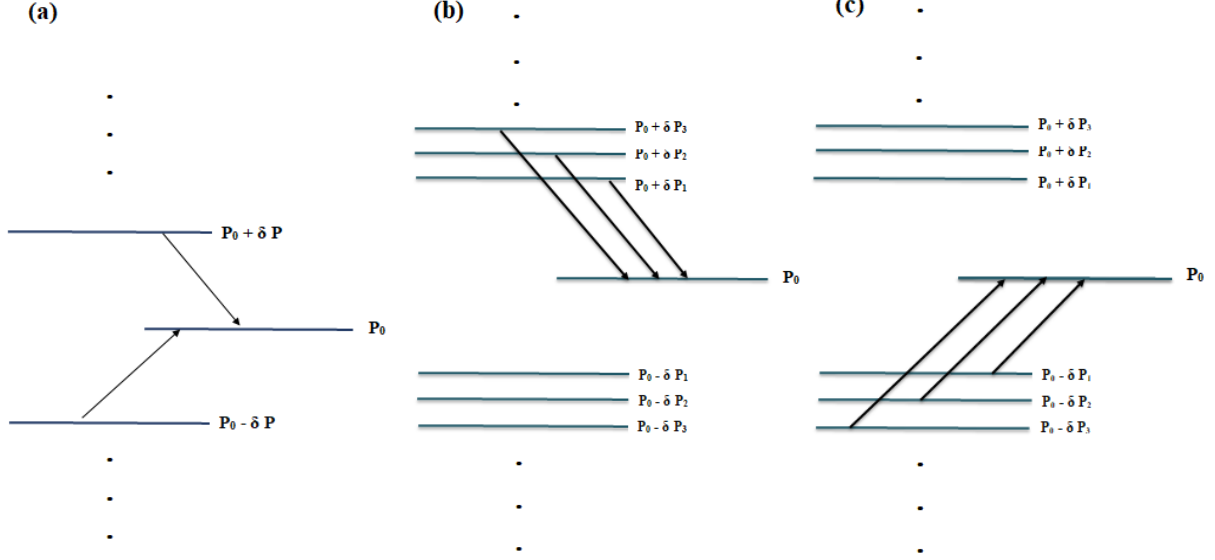


Figure 15: A schematic representation of particles occupying different momentum states in various scenarios during particle creation events.

time reach momentum value  $p_0$  by acceleration process showed by  $u(p_{\parallel}, t)$  and it is also possible that particles at higher momentum level with  $(p_0 + \delta p_0)$  followed by deceleration process  $(p_0 - \delta p_0)$  and finally come to momentum value  $p_0$  (as shown in figure 15). At a specific time  $t_0$ , two possible events can give rise to the quantum interference effect. This expectation is explicitly confirmed in the middle panel of Fig. 5, where onset-oscillations are observed in a bell-shaped profile in LMS  $t \approx 3\tau$ . These oscillations in the LMS are observed for a very short duration, during which coherence is maintained in the LMS of  $u(p_{\parallel}, t)$  and  $v(p_{\parallel}, t)$ , as evident from Figs. 14(e-f). However, these oscillations slowly fade away in the late REPP region around  $t = 4\tau$ . The disappearance of oscillations in the particle LMS can be understood in terms of the loss of coherence that was maintained in the LMS of  $u(p_{\parallel}, t)$  and  $v(p_{\parallel}, t)$ . After the loss of coherence, the LMS of  $u(p_{\parallel}, t)$  and  $v(p_{\parallel}, t)$  become identical at  $t = 6\tau$  (see Fig. 14 (i)). The envelope of the Gaussian with a cosine or sine behavior results in a smooth unimodal structure particle momentum distribution.

#### D. Dependence on Transverse momentum

In this subsection, we extensively investigate the effect of transverse momentum on longitudinal momentum distribution function in dynamical stages of pair production by plotting the time evolution of the LMS for different fixed values of  $p_{\perp}$ , and the result is displayed in Figure 16. The spectra exhibit a smooth unimodal structure during the initial stages, as depicted in Fig. 16(a). Notably, the peak's location shifts, as illustrated in Fig. 16(b), accordingly with the  $(p_{\parallel} - eA(t)) = 0$  as



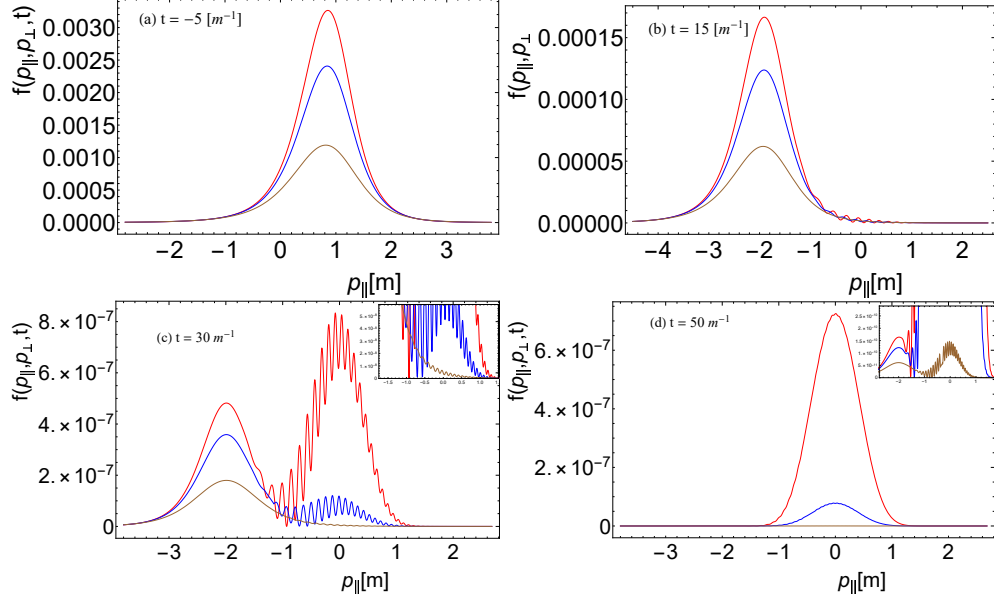


Figure 16: LMS of created particles for different values of the transverse momentum  $p_{\perp}$  ( $p_{\perp} = 0$  (red),  $p_{\perp} = 0.4$  (blue), and  $p_{\perp} = 0.8$  (brown)). The field parameters are  $E_0 = 0.2E_c$  and  $\tau = 10[m^{-1}]$ .

explained in section IV B. Within a narrow spectral region for  $-1 < p_{\parallel} < 1$ , some irregular oscillating structure is observed. Furthermore, these figures indicate that the peak value of the spectra decreases with the increase in the value of transverse momentum. Fig. 16 (c), at  $t = 30[m^{-1}]$  spectra shows bimodal distribution. The central peak structure with onset oscillation located at  $p_{\parallel} = 0$  dominates over another peak at  $p_{\parallel} = -2[m]$  for a small value of  $p_{\perp}$ . One interesting fact observed that the central peak magnitude diminished very rapidly compared to other peaks and that oscillating structure does not exist for high transverse momentum at this time. The existence of oscillation in the central peak depends on what time the particle reaches the on-shell configuration from the initial off-shell mass configuration, which critically depends on both transverse as well as longitudinal momentum values explained in section IV A.

$p_{\perp}[m]$	$t_{cp}[m^{-1}]$	$t_{sep}[m^{-1}]$	$t_{dis.}[m^{-1}]$
0.00	22	30	50
0.25	24	32	53
0.50	31	38	63
0.75	39	47	71
1.00	53	60	83

Table III: Effect of transverse mode on different time scale. The time scale  $t_{cp}$  appearance of a central peak,  $t_{sep}[m^{-1}]$  when two peaks become distinctly separated, and  $t_{dis.}$  disappearance of the oscillation in LMS.

Overall, we know that from section IV A increasing the momentum value particle takes a longer time to reach in REPP stage. So, depending upon the value of  $(p_{\parallel}, p_{\perp})$ , we can say that different

portions of the spectra point to different dynamical stages. The insets of Fig. 16 (c) shows only an irregular oscillatory structure in the tail region of the spectra for  $p_{\perp} = 0.8[m]$ , and the central peak structure is not observed. This absence is attributed to the fact that particles are in the QEPP stage for higher transverse values. At  $t = 50[m^{-1}]$ , for  $p_{\perp} = 0$ , that oscillation is nearly smooth, but for high transverse value,  $p_{\perp} = 0.8[m]$  magnitude of peak diminished see Fig.16 (d), however as shown in insert figure that onset oscillation still observed only magnitude get decreased. From this observation, we can say that the central peak structure does not show the same behavior for a higher value of  $p_{\perp}$ . This is exactly what is implied by Fig. 16 (d). As we see that for higher transverse momentum, we still see that central peak with onset oscillation, which means it just reaches the REPP region. We also observe that for a higher value of  $p_{\perp}$  width of the spectra,  $\Delta p_{\parallel}$  gets decreased, see insert Fig. 16 (d).

Although a detailed analysis is beyond the scope of the present manuscript, the time scales are modified in the presence of transverse momentum  $p_{\perp}$  as follows ( the data not shown):

$$t_{cp} = 0.4606\tau^{1.141}E_0^{-1.273}p_{\perp}^{0.648}, \quad (104)$$

$$t_{sep} = 0.7808\tau^{1.125}E_0^{-1.048}p_{\perp}^{0.536841}, \quad (105)$$

$$t_{dis} = 2.929\tau^{0.85365}E_0^{-0.830}p_{\perp}^{0.3182}. \quad (106)$$

These equations highlight how the time scales are influenced by the electric field strength  $E_0$ , the pulse duration  $\tau$ , and the transverse momentum  $p_{\perp}$ . The time scales found in Ref. [69] differ from the scaling we have identified. In our analysis, we demonstrate that these time scales also depend on the transverse momentum  $p_{\perp}$ , a dependence that was absent in Ref. [69].

### E. Transverse Momentum Spectrum

Following our exploration of the impact of transverse momentum on the longitudinal momentum distribution function, we now shift our attention to the transverse momentum distribution function. Figure 17 shows the time evolution of the TMS for created particles at different times. At the initial time  $t = -5 [m^{-1}]$ , TMS exhibits a smooth, unimodal structure with a peak at  $p_{\perp} = 0[m]$ , where the electric field is at 75% of its maximum strength. As the electric field reaches its maximum value at  $t = 0 [m^{-1}]$ , the spectrum undergoes a dramatic change: both the peak height and width of the spectrum significantly shift, although the peak remains at  $p_{\perp} = 0[m]$ . After the peak reaches its maximum height, it rapidly decreases as the electric field weakens.

The single peak structure initially observed at  $p_{\perp} = 0$  has disappeared, and new peaks have emerged at  $p_{\perp} \approx \pm 0.46 [m]$  in TMS. As an example, at  $t = 7 [m^{-1}]$ , TMS exhibits a bimodal profile, as shown in Fig. 17(c). As time progresses, the peaks at  $p_{\perp} \approx \pm 0.46 [m]$  tend to merge, leading to the formation of a peak at  $p_{\perp} = 0 [m]$  with two weakly pronounced peaks, as illustrated in Fig. 17(d). Those weakly pronounced peaks grow over time, while the height of the central peak decreases. As a result, TMS again exhibits a multi-modal structure, and  $f(p_{\perp}, t)$  reaches its maximum value at non-zero transverse momentum, specifically at  $p_{\perp} \approx \pm 0.65 [m]$  at  $t = 12 [m^{-1}]$ , with a small peak still present at  $p_{\perp} = 0 [m]$ , as shown in Fig. 17(e). Overall, TMS displays a substructure profile where the dominant peak is governed by non-zero values of  $p_{\perp}$ . Upon closer inspection, TMS reveals that the peak at  $p_{\perp} = 0$  becomes invisible again, and the locations of the dominant side peaks undergo slight modulation at  $t = 14 [m^{-1}]$ . Specifically, the dominant peak at  $p_{\perp} = 0.67 [m]$  splits into two weakly pronounced peaks: one at  $p_{\perp} = 0.45 [m]$  and the other at  $p_{\perp} = 0.94 [m]$ , as depicted in Fig. 17(f). As time progresses, the maximum peak at zero transverse momentum reappears. Although this central peak stands out, there are also side peaks (not shown in the figure). These side peaks eventually dominate as the central peak fades, just like in the earlier stages. In this way, the side peaks and the central peak reach the same height, as shown in the figure at  $t = 16.6 [m^{-1}]$ , and the spectrum shows a three-peak pattern.

We can say that the spectrum of created particles at a given time exhibits key features, indicating that the spectrum undergoes continuous changes and reveals two distinct structures. One scenario shows a maximum peak at  $p_{\perp} = 0 [m]$ , suggesting particles with no transverse momentum. The other case displays a maximum peak of the spectrum at a non-zero  $p_{\perp}$  value. In both cases, there are multiple peaks, showing the complex behavior of the spectrum over time, as seen in figure 17(a)-(h).

The effect of created pairs tends to have a peak in the momentum distribution function at non-zero transverse momentum, as discussed by Krajewska et al. [102]. It is demonstrated that the transverse momentum distribution of real pairs exhibits an off-axis maximum above the one-photon threshold frequency (or high frequency); otherwise, the maximum for the transverse distribution function occurs at  $p_{\perp} = 0 [m]$  in the presence of an oscillating time-dependent electric field. This study gives the clue that our case of off-axis maxima or multi-modal structure may also be observed due to multiphoton transition processes. To confirm this, we analyze the probability of pair production by calculating the amplitude in the two-level equivalent formalism [102]. We decompose the time-dependent electric field  $E(t)$  via the Fourier transformation into cosine and sine components. This decomposition isolates individual frequency components of the field, allowing

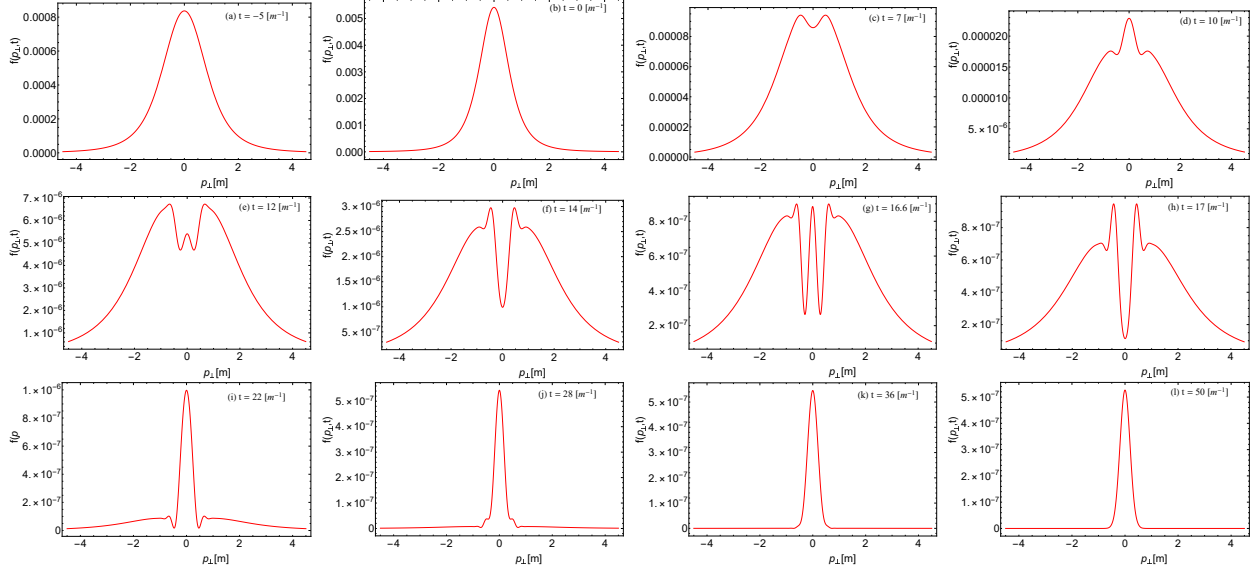


Figure 17: TMS of created particles in the presence of time-dependent Sauter pulse at different times. The longitudinal momentum is considered to be zero, and all the units are taken in the electron mass units. The field parameters are  $E_0 = 0.2E_c$  and  $\tau = 10[m^{-1}]$ .

us to study their effects on pair production at finite times. For a given frequency  $\nu$ , the corresponding electric field amplitude  $\tilde{E}(\nu)$  facilitates the evaluation of the particle production spectrum at a specific finite time  $t$ . The spectrum exhibits multiple peaks, forming a multimodal profile. Each peak corresponds to distinct energy or momentum exchanges between the field and the particle pairs, characteristic of multi-photon absorption. By considering different frequencies  $\nu$  and their respective field amplitudes, we compute the pair production probability for each case. The total probability is obtained by summing the probabilities across different frequencies and then squaring the sum to derive the final result. The resulting spectrum features distinct peaks at various transverse momenta  $p_\perp$ . The peaks appear at non-zero transverse momenta, with their height and position dependent on the specific parameters of the electric field and the timing of the spectrum evaluation (see appendix A 4). The Fourier decomposition approach not only elucidates the origin of multiple peaks in the momentum spectrum but also establishes a connection between these features and the multi-photon process.

After time  $t > 2\tau$ , the transverse momentum distribution function has a peak at  $p_\perp = 0 [m]$ , and the behavior of pair production governed by the tunneling process for  $\gamma < 1$  appears as shown in Figure 17(i)-(l). At  $t \approx 22[m^{-1}]$ , the width of the momentum spectra changes with time. The half-width of the  $p_\perp$ -distribution is determined by the field strength at that time, which is explicitly confirmed by Fig. 17(c)-(l).

As the particle reaches the REPP stage, the spectrum shows a prominent peak at zero transverse

momentum, accompanied by weakly pronounced peaks at  $p_{\perp} \approx \pm 0.67[m]$  and  $p_{\perp} \approx \pm 0.84[m]$  as seen in the Fig. 17(i). As the electric field decays to 98.6% of its maximum value, the width of the  $p_{\perp}$  distribution becomes of the order of  $1[m]$ , and the substructure in TMS disappears ( see Fig.17 (j)). At this stage, the TMS shows a smooth Gaussian-like distribution, with the maximum value  $f(p_{\perp}, t)$  occurring at  $p_{\perp} = 0$  as shown in Fig.17(k). In the absence of an electric field, the spectrum exhibits a single peak Gaussian-like structure that remains unchanged, and also the distribution function  $f(p_{\perp})$  can be well understood by assuming that particle creation is exponentially suppressed with  $\exp(-\frac{m^2+p_{\perp}^2}{eE_0})$  see Fig. 17(l) momentum spectrum shows a Gaussian distribution. This contrast highlights the dynamic evolution of substructures in the initial stages, contrasting with the smooth Gaussian-like structure observed in the REPP stage.

Similar kinds of non-trivial features in the transverse momentum distribution are observed, depending on the details of the electric field parameters discussed by Bechler et al.'s work [103], in which the TMS of generated particles reveals a fascinating characteristic—off-axis maxima above the one-photon threshold frequency (or high frequency). The authors further discuss the significant changes in energy distribution between created particles' longitudinal and transverse motion. This raises questions about the feasibility of pair formation through tunneling theory, given the substantial distribution function values at non-zero transverse momentum but for low frequencies. In our case, we can see that the asymptotic distribution function is described as the Schwinger-like formula, as we see later in section IV E 1. Also, the transverse momentum distribution function shows a maximum value where the transverse momentum becomes negligible. An intriguing aspect is that the tunneling time of particles is altered due to the increase in transverse momentum. This observation is substantiated by the fact that the occurrence of the transient stage is influenced by the momentum values  $(p_{\parallel}, p_{\perp})$ , as explained in section IV A.

Now, we can establish the specific time scales associated with the substructure observed in the TMS of created quasi-particles. By analyzing the peak locations in the transverse distribution function  $f(p_{\perp}, t)$ , we identify three distinct time scales. Initially, after the time interval  $T_1 \approx 0.28 \frac{\tau^{0.1}}{E_0^2}$ , the smooth spectrum begins to reveal an interference pattern, manifesting as a multi-peak structure centered around a non-zero momentum. As time progresses, the spectrum undergoes continuous changes, characterized by oscillatory behavior around  $p_{\perp} = 0$ . This is seen as dips and valleys splitting into multiple peaks. These oscillations persist only up to the time scale  $T_2 \approx 0.11 \frac{\tau^{0.7}}{E_0^{5/2}}$ , indicating a multiphoton signature of particle creation at finite times. After  $T_2$ , the spectrum simplifies, with a dominant peak appearing at  $p_{\perp} = 0$ , accompanied by smaller side peaks. The maximum peak remains at  $p_{\perp} = 0$ , while the small peaks at finite momenta gradually diminish

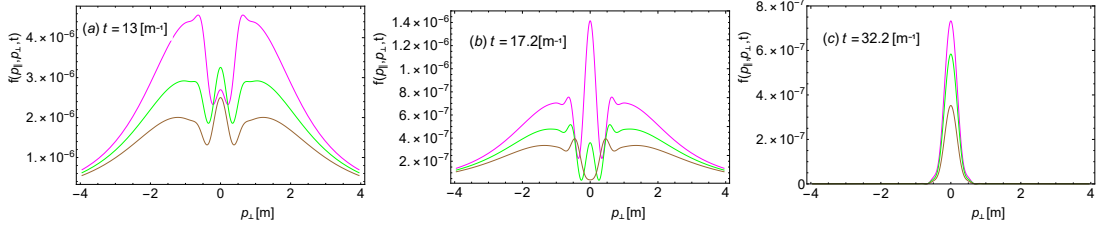


Figure 18: TMS of created particles for different values of the longitudinal momentum  $p_{\parallel}$  ( $p_{\parallel} = 0.1$  (magenta),  $p_{\parallel} = 0.3$  (green), and  $p_{\parallel} = 0.5$  (brown)). The field parameters are  $E_0 = 0.2E_c$  and  $\tau = 10 [m^{-1}]$ .

over the time scale  $T_3 \approx 0.66 \frac{\tau^{0.5}}{E_0^{9/2}}$ . At this time, the system reaches the REPP stage, where the quasi-particle behaves like a real particle.

Next, we investigate the impact of longitudinal momentum on TMS at finite time. We observe the interesting feature that different longitudinal values manifest distinct substructures in the spectrum at a given time, as explicitly verified from Figs. 18(a)-(b). The most common feature observed is that the magnitude of the distribution function decreases for higher longitudinal momentum. Before particles reach the on-shell condition, the spectra of created particles at times  $t > 3\tau$  exhibit a dramatic change in structure, contingent on the value of  $p_{\parallel}$ . For  $p_{\parallel} = 0.1[m]$  and  $p_{\parallel} = 0.3[m]$ , the maximum peak value occurs at vanishing transverse momentum. In contrast, for  $p_{\parallel} = 0.5[m]$ , the maximum peak is observed at non-vanishing transverse momentum, as shown in Fig. 18(b). At this finite time, we observe the sharing of longitudinal and transverse motion. The qualitative change in the shape of the spectrum, due to the influence of longitudinal momentum, can be understood mathematically. Specifically, it requires more time for the quasi-particle to evolve into a real particle with the inclusion of longitudinal momentum when analyzing the TMS of quasi-particles at finite time. In this sense, we can say that the motion of the longitudinal and transverse directions is strongly coupled, and its impact is easily seen in Figs.18. These concerns can be understood by examining the highly oscillating phase kernel  $\cos \Theta_p(t)$  present in the quantum kinetic equation (QKE) [53]. This kernel depends on the quasi-energy  $\omega(p_{\parallel}, p_{\perp}, t)$ , which connects the longitudinal and transverse motions of the created particles. At the REPP stage, the substructure in the spectrum disappears, and the peak height for higher longitudinal momentum value is consistently lower, shown in Fig. 18(c).

### 1. Approximate expression for transverse momentum distribution function

In this subsection, we discuss the mathematical origin of the substructures that appear in the TMS. Using the approximate analytical expression of the single-particle distribution function in

momentum space, which is derived in section III C. We find the approximate expression for the transverse momentum distribution function is given by:

$$f(p_{\perp}, y) \approx |N^+(p_{\perp})|^2 \left( C_0(p_{\perp}, y) + (1-y)C_1(p_{\perp}, y) + (1-y)^2 C_2(p_{\perp}, y) \right), \quad (107)$$

with,

$$\begin{aligned} C_0(p_{\perp}, y) &= 4y^2 |\Gamma_2|^2 \left( 1 + p_{\perp}^2 + E_0 \tau (E_0 \tau + \sqrt{1 + p_{\perp}^2 + E_0^2 \tau^2}) \right), \\ C_1(p_{\perp}, y) &= -\frac{4y |\Gamma_1 \bar{\Gamma}_2| E_0 \tau (1 + p_{\perp}^2)}{\sqrt{1 + p_{\perp}^2 + E_0^2 \tau^2}} \cos(\Upsilon), \\ C_2(p_{\perp}, y) &= 4|\Gamma_1|^2 E_0^2 \tau^2 (1 + p_{\perp}^2) \frac{\sqrt{1 + p_{\perp}^2 + E_0^2 \tau^2} - E_0 \tau}{(1 + p_{\perp}^2 + E_0^2 \tau^2)^{3/2}} \\ &\quad - 8|\Gamma_1 \bar{\Gamma}_2| E_0 \tau \cos(\Upsilon) \left( \frac{(1 + p_{\perp}^2)(1 + p_{\perp}^2 + E_0 \tau \sqrt{1 + p_{\perp}^2 + E_0^2 \tau^2})}{(1 + p_{\perp}^2 + E_0^2 \tau^2)^{3/2}} \right. \\ &\quad \left. - y \left( 5E_0 \tau - \frac{E_0^2 \tau^2}{\sqrt{1 + p_{\perp}^2 + E_0^2 \tau^2}} + 2\sqrt{1 + p_{\perp}^2 + E_0^2 \tau^2} + \frac{E_0^4 \tau^2 [3 + \tau^2 (1 + p_{\perp}^2 + E_0^2 \tau^2)]}{(1 + p_{\perp}^2 + E_0^2 \tau^2)^{3/2}} \right) \right. \\ &\quad \left. + E_0^3 \tau^3 \frac{(-1 + \tau^2 (1 + p_{\perp}^2 + E_0^2 \tau^2))}{1 + p_{\perp}^2 + E_0^2 \tau^2} \right) - \frac{y^2 (1 + E_0^2 \tau^4)}{4 + \tau^2 (1 + p_{\perp}^2 + E_0^2 \tau^2)} (4 + E_0 \tau^3 \sqrt{1 + p_{\perp}^2 + E_0^2 \tau^2}) \\ &\quad (E_0 \tau + \sqrt{1 + p_{\perp}^2 + E_0^2 \tau^2}). \end{aligned} \quad (108)$$

Fig. 19 shows the time evolution of individual terms present in Eq. (107) as a function of transverse momentum. The profile of  $(1-y)^2 C_2(p_{\perp}, y)$  exhibits substructure, with its maximum peak located at  $p_{\perp} \approx \pm 0.65$  [m] and a valley near  $p_{\perp} \approx \pm 0.25$  [m], as observed at  $t = 13$  [ $m^{-1}$ ] (see Fig. 19(a)). Similarly, the feature shown by  $(1-y)C_1(p_{\perp}, y)$  has peaks at  $p_{\perp} = \pm 0.25$  [m], but its peak value is much smaller compared to  $(1-y)^2 C_2(p_{\perp}, y)$ . As time progresses, this substructure can change according to Eq. (108). Therefore, as seen in Fig. 19(b) at  $t = 17$  [ $m^{-1}$ ], the profiles of  $(1-y)^2 C_2(p_{\perp}, y)$  and  $(1-y)C_1(p_{\perp}, y)$  change with time, with the peak magnitude of  $(1-y)^2 C_2(p_{\perp}, y)$  still dominating over the other terms. The change in the shape of  $(1-y)^2 C_2(p_{\perp}, y)$  and  $(1-y)C_1(p_{\perp}, y)$  can be understood as  $\cos(\Upsilon)$  function that presents in the relation Eq.(108).

Furthermore, we can approximate the functions  $C_1(p_{\perp}, y)$  and  $C_2(p_{\perp}, y)$  to analyze the qualitative

impact on the transverse momentum distribution function. Using the condition  $E_0\tau > 1$ ,

$$C_1(p_\perp, y) \approx \exp\left(\frac{p_\perp^2}{2}\tau\left(\frac{2E_0^2\tau}{1+E_0^2\tau^2} - \frac{E_0 + \pi}{\sqrt{1+E_0^2\tau^2}}\right)\right) \cos(\Upsilon) \frac{2yE_0(1+E_0\tau(E_0\tau + \sqrt{1+E_0^2\tau^2}))}{(1+E_0^2\tau^2)^{3/2}} e^{\pi\tau(E_0\tau - \sqrt{1+E_0^2\tau^2})}, \quad (109)$$

$$C_2(p_\perp, y) \approx 4E_0^2\tau^2(1+p_\perp^2) \frac{(-E_0\tau + \sqrt{1+p_\perp^2 + E_0^2\tau^2})}{(1+p_\perp^2 + E_0^2\tau^2)^{3/2}} |\Gamma_1|^2 + \frac{4E_0 e^{-\Lambda \frac{p_\perp^2}{2}} \cos(\Upsilon)}{\tau(1+E_0^2\tau^2)^{7/2}} \left(3E_0^4\tau^5(3+8E_0^2) + 13E_0^6\tau^7 + 6E_0^8\tau^9 + 12E_0\sqrt{1+E_0^2\tau^2} + 4E_0\tau^2(1+7E_0^2)\sqrt{1+E_0^2\tau^2} + 8E_0^3\tau^4(1+3E_0^2)\sqrt{1+E_0^2\tau^2} + 10E_0^5\tau^6\sqrt{1+E_0^2\tau^2} + 6E_0^7\tau^8\sqrt{1+E_0^2\tau^2}\right), \quad (110)$$

with,

$$\Lambda = (\tau(48E_0^2 - 1) + E_0^2\tau^3(136E_0^2 - 5) + E_0^4\tau^5(9 + 88E_0^2) + 29E_0^6\tau^7 + 16E_0^8\tau^9 + 24E_0\sqrt{1+E_0^2\tau^2} + 64E_0^3\tau^2\sqrt{1+E_0^2\tau^2} + 8E_0^3\tau^4(11E_0^2 - 1)\sqrt{1+E_0^2\tau^2} + 8E_0^5\tau^6\sqrt{1+E_0^2\tau^2} + 16E_0^7\tau^8\sqrt{1+E_0^2\tau^2}) / ((1+E_0^2\tau^2)(\tau + 16E_0^2\tau + E_0^2\tau^3(3+40E_0^2) + 3E_0^4\tau^5(3+8E_0^2) + 13E_0^6\tau^7 + 6E_0^8\tau^9 + 12E_0\sqrt{1+E_0^2\tau^2} + 4E_0\tau^2(1+7E_0^2)\sqrt{1+E_0^2\tau^2} + 8E_0^3\tau^4(1+3E_0^2)\sqrt{1+E_0^2\tau^2} + 10E_0^5\tau^6\sqrt{1+E_0^2\tau^2} + 6E_0^7\tau^8\sqrt{1+E_0^2\tau^2})). \quad (111)$$

From Eq.(109) and (110), we easily see that  $C_1(p_\perp, y)$  and  $C_2(p_\perp, y)$  shows Gaussian-like profile with the cosine function and its behavior depends on the field parameters. We now analyze the  $C_2(p_\perp, y)$  function that shows the complicated substructure that changes with time. From Eq.(110) first term shows a complicated substructure having two peaks at  $p_\perp \approx \pm 1.5[m]$  and dip at the  $p_\perp \approx 0$ . This structure does not change with time but the second term plays crucial role whose depends the shape of profile on the time since  $\cos(\Upsilon)$  factor and its gives multi-peak substructure behavior. To further analyze the substructure behavior of the spectra, we reconsider the argument  $\Upsilon$  as outlined in section IV B 1. For this purpose, we approximate  $\Upsilon$  by including terms up to  $p_\perp^2$



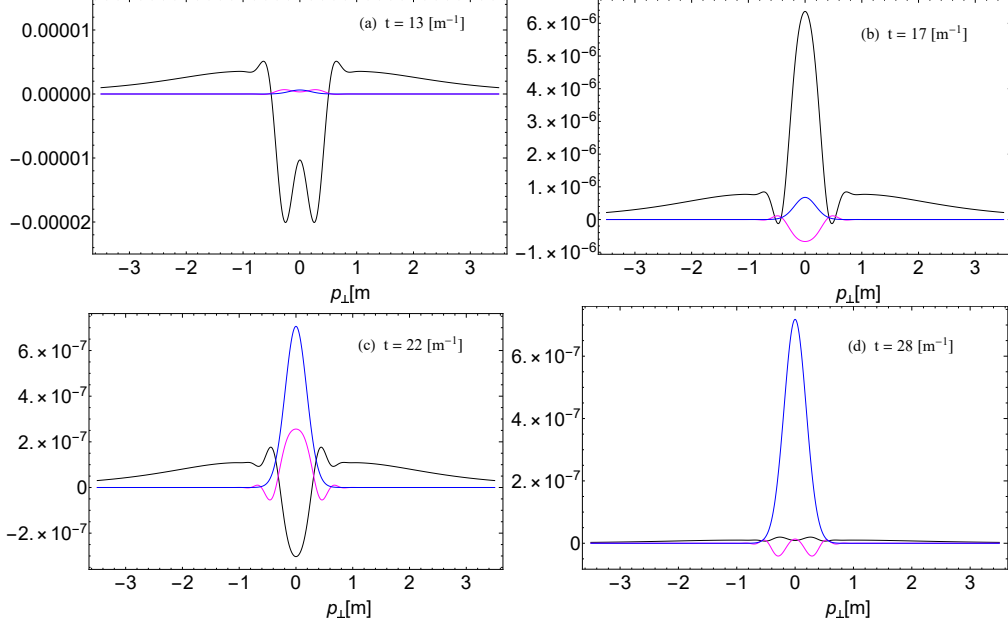


Figure 19: The zeroth, first, and second-order terms as a function of the transverse momentum for different times. Blue curve:  $C_0(p_\perp, y)$ , Magenta curve:  $(1-y)C_1(p_\perp, y)$ , and Black curve:  $(1-y)^2 C_2(p_\perp, y)$ . The field parameters are  $E_0 = 0.2E_c$  and  $\tau = 10 [m^{-1}]$ .

and disregarding higher-order terms.

$$\begin{aligned}
\Upsilon \approx & E_0 \tau^2 \ln(1 + (E_0 \tau + 2E_0 \tau \sqrt{1 + E_0^2 \tau^2})) + \ln\left(\frac{(1-y)}{\sqrt{1 + E_0^2 \tau^2}}\right) \tau \sqrt{1 + E_0^2 \tau^2} \\
& + \frac{p_\perp^2 \tau}{2 \sqrt{1 + E_0^2 \tau^2}} \ln\left(\frac{(1-y)}{1 + E_0^2 \tau^2}\right)
\end{aligned} \tag{112}$$

It shows that the behavior is symmetric about the origin, which can be understood as the presence of only the  $p_\perp^2$ - term and the absence of the linear term in  $p_\perp$ , in comparison to the longitudinal momentum case as discussed in section IV B 1. One more thing we notice is that at  $p_\perp = 0$ , the behavior of the  $\cos(\Upsilon)$  function changes drastically with time due to the presence of the time-dependent term  $\ln(1-y)$ . The oscillation frequency also depends on  $p_\perp^2$ , which means the frequency increases as the transverse momentum value increases. However, the coefficient of  $\cos(\Upsilon)$  function plays a role here, giving a Gaussian envelope to the cosine function as discussed previously section IV B 1. Within the width of the Gaussian profile, the oscillations survive and are seen in the spectrum.

Fig.19(c) shows that the  $C_0(p_\perp, y)$  term dominates over the other terms. We still observe substructure in the terms,  $(1-y)C_1(p_\perp, y)$  and  $(1-y)^2 C_2(p_\perp, y)$ . Although their magnitudes decrease

drastically, these terms still impact  $f(p_{\perp}, t)$  at this time. The term  $C_0(p_{\perp}, y)$  shows a smooth Gaussian profile with a peak at  $p_{\perp} = 0$ , and its shape does not change with time. At  $t = 32 [m^{-1}]$ , the first and second-order terms are suppressed, and the features of the spectra can be explained by the zeroth-order term alone. Therefore, by closely analyzing the different terms  $C_0$ ,  $(1 - y)C_1$ , and  $(1 - y)^2C_2$  as defined in Eq. 108, we can observe the following: Initially, the TMS behavior is qualitatively explained by the first and second-order terms. Up to  $t \approx 2\tau$ , the function  $(1 - y)^2C_2$  continues to qualitatively account for the non-zero peak and substructure near the transient region. This substructure arises from the time-dependent  $\cos(\Upsilon)$  function. As time progresses, the magnitudes of  $(1 - y)^2C_2$  and  $(1 - y)C_1$  decrease and are eventually suppressed as  $y \rightarrow 1$ . Compared to the other terms in the distribution function, this suppression causes the substructure to nearly disappear (see Fig. 17).

In the late-time limit,  $f(p_{\perp}, y \rightarrow 1)$  is governed mainly by the zeroth-order term,  $C_0(p_{\perp}, y)$ . As a result, the spectra only show a single peak with a smooth profile. To demonstrate this, we can find the asymptotic expression for the transverse momentum distribution function in the limit  $y \rightarrow 1$ . From Eq. (107), we can write it as:

$$f(p_{\perp}, y \rightarrow 1) \approx |N^+(p_{\perp})|^2 C_0(p_{\perp}) \quad (113)$$

By lengthy calculation, as we do for the longitudinal momentum case, we found an expression for the transverse momentum distribution function for asymptotic time as follows:

$$f(p_{\perp}) \approx 2e^{2\pi\tau(E_0\tau - \sqrt{1+E_0^2\tau^2})} \exp\left(\frac{-\pi p_{\perp}^2 \tau}{\sqrt{1 + E_0^2\tau^2}}\right). \quad (114)$$

the above Eq. (114) clearly shows that in the REPP stage, the transverse distribution function has an invariable Gauss-like distribution whose half-width is defined by the field strength,  $E_0$ , and pulse duration  $\tau$ .

## V. CONCLUSION

We have conducted a detailed analysis of the electron-positron pair production from the vacuum under the influence of a time-dependent Sauter pulse electric field. We calculate the single-particle distribution function with the help of the exact analytic solution for the mode function. We develop an analytical theory that is valid for the finite times  $t > \tau$ . In particular, we find an analytical expression for the distribution function in the power series of the small parameter  $(1 - y)$ . The

interesting dynamical features of the momentum distribution function at finite times are attributed to the function that appears in this expansion. We have further elaborated on this aspect of the finite-time behavior of the longitudinal and transverse momentum spectra.

We analyzed the temporal evolution of the single-particle distribution function. Our investigation reveals that the process of transition from initially virtual particles to real particles occurs in three distinct stages, which crucially depend on the longitudinal and transverse modes. Moreover, we have quantified the initiation of the REPP stage, determined by the momentum value, with higher momenta resulting in narrower oscillations in the transient region. We meticulously examined the LMS and TMS to understand the momentum-dependent behavior during these stages. In the LMS, one interesting feature at the beginning of the REPP stage is that the spectrum exhibits an oscillating structure as imprints of a quantum signature at the finite time where the electric field is nearly zero. The two-peaked structure in which the central Gaussian-peak structure has onset oscillation, and this quantum interference pattern evolves and fades away. Based on this observation, we identified three distinct time scales associated with this behavior. Additionally, we investigated the impact of different electric field strengths ( $E_0$ ) on the duration of the interference pattern's formation and disappearance. In the multiphoton regime, for  $\gamma = 2.5$ , we explored the time evolution of LMS in different stages of pair production, and the spectrum shows the splitting of a smooth uni-modal structure into a multi-modal Gaussian structure near the REPP region, after which it merges into a single peak Gaussian profile at the asymptotic time limit.

Utilizing the approximate expressions for the momentum distribution function, we unveiled that the LMS structure mainly comprises three distinct functional behaviors. The second-order term dominantly governs the early times, while combining the first and zeroth-order terms leads to the central peak structure with onset oscillation. The first-order term contributes to oscillations, owing to the presence of a Gaussian envelope with oscillation, but its amplitude diminishes with time, resulting in a smooth spectrum profile in late time.

Furthermore, we examined the role of vacuum polarization,  $u(p_{\parallel}, t)$ , and its counterpart,  $v(p_{\parallel}, t)$ , by plotting their time evolution. In the REPP region, both  $u(p_{\parallel}, t)$  and  $v(p_{\parallel}, t)$  exhibit nearly identical oscillations with the same amplitude, and this oscillation amplitude decays for higher  $p_{\parallel}$  values. This observation implies that the qualitative nature of the vacuum polarization function is significantly influenced by the longitudinal momentum. To elucidate this further, we plotted the LMS of  $u(p_{\parallel}, t)$  and  $v(p_{\parallel}, t)$ . These plots reveal two distinct patterns emerging at the start of the REPP stage. One pattern exhibits a Gaussian-like structure, while the other displays a deformed oscillating profile within the Gaussian envelope. These oscillations, exhibiting varying amplitudes,

were confined to a small window of longitudinal momentum ( $-1 < p_{\parallel} < 1$ ). Over time, the regular oscillations of  $u(p_{\parallel}, t)$  and  $v(p_{\parallel}, t)$  became balanced, as explicitly observed in the plot of the LMS of the created particles for late time, where the oscillating behavior was absent due to the equilibrium between  $u(p_{\parallel}, t)$  and  $v(p_{\parallel}, t)$ . As we recognize the pivotal roles of  $u(p_{\parallel}, t)$  and  $v(p_{\parallel}, t)$  functions in accelerating (creation of  $e^{-}$ ) and decelerating (annihilation of  $e^{-}$ ) electrons, respectively, the observed oscillations in the  $f(p_{\parallel}, t)$  at finite times can be attributed to the characteristic behavior imprints of these functions, resulting from the acceleration and deceleration of electrons in momentum representation, which manifests as the observed oscillating structure. Next, we also discuss the influence of transverse momentum on LMS, which diminishes the value of  $f(p_{\parallel})$  and smooths out the oscillation for higher  $p_{\perp}$  values. Moreover, we emphasized that these oscillations, seen in the late REPP stage as transverse momentum increases and also impact the formation time of pairs.

Finally, we study the dynamics of TMS, uncovering interesting results that have received limited attention from other authors, particularly in the context of the Sauter pulsed electric field. We observe fluctuating substructures that undergo regular changes in the QEPP and transient region depending on momentum value. This behavior of substructures during this stage is also influenced by longitudinal momentum, resulting in distinct substructures in the spectrum at a given time. This finding indicates that the longitudinal and transverse momentum is related to each other during particle-antiparticle formation quantitatively and qualitatively. At the beginning of the REPP region, that substructure disappears. The shape of the spectrum becomes an invariable Gauss-like profile and is not affected by the longitudinal momentum but its peak value still depends on it during the REPP stage. This contrast highlights the dynamic evolution of substructures in earlier stages, contrasting with the stable Gaussian-like structure observed in the REPP stage. A similar intriguing behavior in the transverse momentum distribution has been observed in the works by Krajewska et al. [102] and Bechler et al. [103], depending on the specifics of the electric field parameters. These studies highlight a fascinating characteristic of the transverse distribution function peak that occurs at non-zero  $p_{\perp}$  value depending on the frequency. This observation prompts questions about the feasibility of pair formation through tunneling theory, particularly considering the significant distribution function values at non-zero transverse momentum for low frequencies. For our case, the spectrum also shows the occurrence of peak at non-zero transverse momentum signifies the creation of pairs through the multiphoton process at finite times. Although studying the LMS and TMS of created quasi-particles at various dynamical stages shows a critical dependence on longitudinal and transverse momentum, it also brings attention to the intriguing physics

behind the behavior of the vacuum in this finite-time scenario for the pair production process.

## VI. ACKNOWLEDGMENTS

Deepak gratefully acknowledge the financial support from Homi Bhabha National Institute (HBNI) for carrying out this research work.

### Appendix A: Appendixes

#### 1. Normalization of Analytic Mode function

The normalization constants  $N^{(\pm)}$  are chosen such that

$$\psi_{\mathbf{p}}^{(\pm)}(y) = \phi_{\mathbf{p}}^{(\pm)}(y), y \rightarrow 0. \quad (\text{A1})$$

Accordingly we have to investigate the behaviour of the mode functions  $\psi_{\mathbf{p}}^{(\pm)}(y)$  in this limit

$$\begin{aligned} \psi_{\mathbf{p}}^{(+)}(y) &= N^{(+)} y^k (1-y)^l {}_2\mathcal{F}_1(a, b, c; y) \\ &= N^{(+)} e^{k \ln(y)} e^{l \ln(1-y)} {}_2\mathcal{F}_1(a, b, c; y) \\ &\stackrel{y \rightarrow 0}{=} N^{(+)} e^{k \ln(y)} = N^{(+)} y^k \end{aligned} \quad (\text{A2})$$

as  ${}_2\mathcal{F}_1(a, b, c; y \rightarrow 0) = 1$ . A similar calculation can be done for  $\psi_{\mathbf{p}}^{(-)}(y)$ , which results in

$$\psi_{\mathbf{p}}^{(-)}(y) \stackrel{y \rightarrow 0}{=} N^{(+)} e^{k \ln(y)} = N^{(-)}(\mathbf{p}) y^{-k} \quad (\text{A3})$$

It is possible to calculate  $\phi_{\mathbf{p}}^{(\pm)}(y)$  in the same limit. From the definition of the functions, we have

$$\phi_{\mathbf{p}}^{(\pm)}(y) = \frac{e^{\mp i \Theta_{\mathbf{p}}(y)}}{\sqrt{2\omega(\mathbf{p}, y)(\omega(\mathbf{p}, y) \mp P(p_{\parallel}, t))}} \quad (\text{A4})$$

with the transformed dynamical phase  $\Theta_{\mathbf{p}}(y)$ . Using the  $\partial_t = \frac{2}{\tau} y(1-y) \partial_y$  we find

$$\Theta_{\mathbf{p}}(t) = \int_{t_0}^t dt' \omega(\mathbf{p}, t'), \quad (\text{A5})$$

which takes the form

$$\Theta_{\mathbf{p}}(y) = \frac{2}{\tau} \int_{y_0}^y dy' \frac{\omega(\mathbf{p}, y')}{y' (1 - y')} \quad (\text{A6})$$

gives the dynamical phases accumulated between the initial and final states.

The integration can be performed analytically

$$\begin{aligned} \int \frac{\omega(\mathbf{p}, y)}{y' (1 - y')} dy &= -2E_0\tau \ln(p_{\parallel} + yE_0\tau - E_0\tau(1 - y) + \omega(\mathbf{p}, y)) \\ &+ \omega_0(\ln(y) - \ln(1 + p_{\perp}^2 + (p_{\parallel} - E_0\tau)(p_{\parallel} + (2y - 1)E_0\tau) + \omega_0\omega(\mathbf{p}, y))) \\ &- \omega_1(\ln(1 - y) - \ln(1 + p_{\perp}^2 + (p_{\parallel} + E_0\tau)(p_{\parallel} + (2y - 1)E_0\tau) + \omega_1\omega(\mathbf{p}, y))) \end{aligned} \quad (\text{A7})$$

In the limit  $y \rightarrow 0$ , the dynamical phase splits into a regular part  $\tilde{\Theta}_{\mathbf{p}}(y = 0)$  as well as into a divergent part

$$\Theta_{\mathbf{p}}(y) \stackrel{y \rightarrow 0}{\approx} \frac{\tau}{2} \omega_0 \ln y + \tilde{\Theta}_{\mathbf{p}}(0) \quad (\text{A8})$$

The mode functions  $\phi_{\mathbf{p}}^{(\pm)}(y)$  reads

$$\phi_{\mathbf{p}}^{(\pm)}(y) = \frac{e^{\mp i\tilde{\Theta}_{\mathbf{p}}(0)}}{\sqrt{2\omega(\mathbf{p}, 0)(\omega(\mathbf{p}, 0) \mp P(p_{\parallel}, 0))}} e^{\mp i\frac{\tau}{2}\omega_0 \ln(y)} \quad (\text{A9})$$

Denoting  $P_0 = P(p_{\parallel}, 0)$ ,  $\omega_0 = \omega(\mathbf{p}, 0)$ . Comparison of (A2),(A3) and (A9) and fixes the normalization constants

$$N^{(+)}(\mathbf{p}) = \frac{e^{-i\tilde{\Theta}_{\mathbf{p}}(0)}}{\sqrt{2\omega_0(\omega_0 - P_0)}} \quad (\text{A10})$$

$$N^{(-)}(\mathbf{p}) = \frac{e^{i\tilde{\Theta}_{\mathbf{p}}(0)}}{\sqrt{2\omega_0(\omega_0 + P_0)}} \quad (\text{A11})$$

## 2. Evaluation simple analytical expression for $f(\mathbf{p}, t)$

To investigate the behavior of the distribution functions in the limit  $t \gg \tau$ , we employ approximations based on the suitable expressions of the Gamma and the Gauss-hypergeometric functions. These approximations enable us to deduce a simplified analytical expression for particle distribution functions. First, we start with approximating the Gauss-hypergeometric function as  $y \rightarrow 1$ .

It is crucial to ensure smooth convergence towards the limit of  ${}_2\mathcal{F}_1(a, b, c; y \rightarrow 1)$ . This task is complicated by the intricate nature of the parameters  $a$ ,  $b$ , and  $c$  in this specific context, which makes it essential to exercise caution when dealing with this limit. Therefore, it is beneficial to transform the argument by substituting  $y$  with  $(1 - y)$ . This transition can be achieved using the following mathematical identity.

$$\begin{aligned} {}_2\mathcal{F}_1(a, b, c; z) &= \frac{\Gamma(c)\Gamma(c-a-b)}{\Gamma(c-a)\Gamma(c-b)} {}_2\mathcal{F}_1(a, b, a+b-c+1; 1-z) \\ &\quad + (1-z)^{c-a-b} \frac{\Gamma(c)\Gamma(a+b-c)}{\Gamma(a)\Gamma(b)} {}_2\mathcal{F}_1(c-a, c-b, c-a-b+1; 1-z). \end{aligned} \quad \left| \arg(1-z) \right| < \pi \quad (\text{A12})$$

In general Gauss-hypergeometric function,

$${}_2\mathcal{F}_1(a, b, c; z) = 1 + \frac{ab}{c}z + \frac{a(a+1)b(b+1)}{c(c+1)} \frac{z^2}{2!} + \frac{a(a+1)(a+2)b(b+1)(b+2)}{c(c+1)(c+2)} \frac{z^3}{3!} + \dots \quad (\text{A13})$$

The series continues with additional terms involving higher powers of  $z$ . Each term in the series involves the parameters  $a$ ,  $b$ , and  $c$  as well as the variable  $z$  raised to a specific power.

Using the above relations Eq. (A12) and (A13), we approximate the Gauss-hypergeometric functions  $f_1$  and  $f_2$  present in the relation of the particle distribution function (see Eq.(59)) as follows:

$$\begin{aligned} f_1 &= {}_2\mathcal{F}_1(1+a, 1+b; 1+c; y) \\ &= \frac{\Gamma(1+c)\Gamma(c-a-b-1)}{\Gamma(c-a)\Gamma(c-b)} {}_2\mathcal{F}_1(1+a, 1+b, 2+a+b-c; 1-y) \\ &\quad + \frac{\Gamma(1+c)\Gamma(1+a+b-c)}{\Gamma(1+a)\Gamma(1+b)} (1-y)^{(c-a-b-1)} {}_2\mathcal{F}_1(c-a, c-b, c-a-b; 1-y) \\ &= \left( \frac{c\Gamma(c)\Gamma(c-a-b-1)}{\Gamma(c-a)\Gamma(c-b)} \right) \left( 1 + \frac{(a+1)(b+1)}{(2+a+b-c)}(1-y) \right. \\ &\quad \left. + \frac{(a+1)(a+2)(b+1)(b+2)}{(2+a+b-c)(2+a+b-c+1)} \frac{(1-y)^2}{2!} + \dots \right) \\ &\quad + (1-y)^{(c-a-b-1)}(a+b-c) \left( \frac{c\Gamma(c)\Gamma(a+b-c)}{a\Gamma(a)b\Gamma(b)} \right) \left( 1 + \frac{(c-a)(c-b)}{(c-a-b)}(1-y) \right. \\ &\quad \left. + \frac{(c-a)(c-a+1)(c-b)(c-b+1)}{(c-a-b)(c-a-b+1)} \frac{(1-y)^2}{2!} + \dots \right) \end{aligned} \quad (\text{A14})$$

Similarly,

$$\begin{aligned}
f_2 &= \frac{\Gamma(c)\Gamma(c-a-b)}{\Gamma(c-a)\Gamma(c-b)} {}_2\mathcal{F}_1(a, b, 1-c+a+b; 1-y) \\
&+ (1-y)^{(c-a-b)} \frac{\Gamma(c)\Gamma(a+b-c)}{\Gamma(a)\Gamma(b)} {}_2\mathcal{F}_1(c-a, c-b, 1+c-a-b; 1-y) \\
&= \frac{\Gamma(c)\Gamma(c-a-b)}{\Gamma(c-a)\Gamma(c-b)} \left( 1 + \frac{ab}{1+a+b-c}(1-y) + \frac{(a+1)(b+1)}{(2+a+b-c)} \frac{(1-y)^2}{2!} + \dots \right) \\
&+ (1-y)^{(c-a-b)} \frac{\Gamma(c)\Gamma(a+b-c)}{\Gamma(a)\Gamma(b)} \left( 1 + \frac{(c-a)(c-b)}{(1+c-a-b)}(1-y) + \dots \right) \tag{A15}
\end{aligned}$$

Here,  $y$  is a variable that changes with time according to Eq. (47). To compute an approximate expression for the particle distribution function that depends on finite time, we can truncate the power series of the Gauss-hypergeometric functions  $f_1$  and  $f_2$  given by Eqs. (A14) and (A15) respectively, up to a specific order. The order of truncation will depend on the desired accuracy and the characteristics of the finite-time behavior under consideration.

Let's start by approximating the different terms present in the particle distribution relation Eq. (70) and (71), considering only up to the second-order terms and neglecting higher-order terms.

Therefore,

$$\begin{aligned}
\frac{2y}{\tau}(1-y)\frac{ab}{c}f_1 &\approx \frac{2}{\tau}y(a+b-c)\Gamma_2(1-y)^{(c-a-b)} + (1-y)\frac{2y}{\tau} \left( ab\Gamma_1 - (c-a)(c-b)\Gamma_2(1-y)^{(c-a-b)} \right) \\
&+ (1-y)^2 \frac{2y}{\tau} \left( \Gamma_1 \frac{a(1+a)b(1+b)}{(2+a+b-c)} + \Gamma_2(1-y)^{(c-a-b)} \frac{(c-a)(c-b)(c-a+1)(c-b+1)}{(a+b-c-1)} \right) \tag{A16}
\end{aligned}$$

where we have used

$$\Gamma_1 = \frac{\Gamma(c)\Gamma(c-a-b-1)}{\Gamma(c-a)\Gamma(c-b)}, \tag{A17}$$

$$\Gamma_2 = \frac{\Gamma(c)\Gamma(a+b-c)}{\Gamma(a)\Gamma(b)}. \tag{A18}$$

Similarly,

$$\begin{aligned}
(\omega(\mathbf{p}, y) - (1-y)\omega_0 - y\omega_1)f_2 &= (\omega(\mathbf{p}, y) - (1-y)\omega_0 - y\omega_1) \left( \Gamma_1(c-a-b-1) \right. \\
&\left. \left( 1 + (1-y)\frac{ab}{(1+a+b-c)} \right) + (1-y)^{(c-a-b)}\Gamma_2 \left( 1 + (1-y)\frac{(c-a)(c-b)}{(1+c-a-b)} \right) \right) \tag{A19}
\end{aligned}$$



Also, it is possible to write down the time-dependent quasi-energy  $\omega(\mathbf{p}, y)$  as the following series expansion near  $y \rightarrow 1$  :

$$\omega(\mathbf{p}, y) \approx \omega_1 - (1-y) \frac{2E_0\tau}{\omega_1} P_1 + (1-y)^2 \frac{2E_0^2\tau^2}{\omega_1^3} \epsilon_\perp^2(p_\perp) \quad (\text{A20})$$

up to the second order and neglect the other higher order terms.

Therefore,

$$\begin{aligned} (\omega(\mathbf{p}, y) - (1-y)\omega_0 - y\omega_1) f_2 \approx & (1-y) \left( (\omega_1 - \omega_0) - \frac{2E_0\tau}{\omega_1} P_1 \right) \left( \Gamma_1(c-a-b-1) + e^{-i\tau\omega_1 \ln(1-y)} \Gamma_2 \right) \\ & + (1-y)^2 \left( \Gamma_1(c-a-b-1) \left( \frac{2E_0^2\tau^2 \epsilon_\perp^2}{\omega_1^3} + \frac{ab(\omega_1(\omega_1 - \omega_0) - 2P_1 E_0\tau)}{\omega_1(1+a+b-c)} \right) \right. \\ & \left. + \Gamma_2 e^{-i\tau\omega_1 \ln(1-y)} \left( \frac{2E_0^2\tau^2 \epsilon_\perp^2}{\omega_1^3} + \left( (\omega_1 - \omega_0) - \frac{2E_0\tau}{\omega_1} P_1 \right) \frac{(c-a)(c-b)}{(1+c-a-b)} \right) \right) \end{aligned} \quad (\text{A21})$$

Using the above relation, we get

$$\begin{aligned} & \left| \frac{2}{\tau} y(1-y) \frac{ab}{c} f_1 + i(\omega(\mathbf{p}, y) - (1-y)\omega_0 - y\omega_1) f_2 \right|^2 \\ \approx & \left| \frac{2}{\tau} y(a+b-c) \Gamma_2 e^{-i\tau\omega_1 \ln(1-y)} + (1-y) \left[ \Gamma_1 \left( \frac{2}{\tau} yab + i(c-a-b-1) \left( \omega_1 - \omega_0 - \frac{2E_0\tau P_1}{\omega_1} \right) \right) \right. \right. \\ & \left. \left. + \Gamma_2 e^{-i\tau\omega_1 \ln(1-y)} \left( \frac{2}{\tau} y(a+b-c) \frac{(c-a)(c-b)}{(c-a-b)} + i \left( \omega_1 - \omega_0 - \frac{2E_0\tau P_1}{\omega_1} \right) \right) \right] + (1-y)^2 \left[ \Gamma_1 \left( \frac{2}{\tau} yab \right. \right. \right. \\ & \left. \left. \frac{(1+a)(1+b)}{(2+a+b-c)} + i \left( \frac{2E_0^2\tau^2 \epsilon_\perp^2}{\omega_1^3} + \frac{ab}{(1+a+b-c)} \left( \omega_1 - \omega_0 - \frac{2E_0\tau P_1}{\omega_1} \right) \right) (c-a-b-1) \right) \right. \\ & \left. \left. + \Gamma_2 e^{-i\tau\omega_1 \ln(1-y)} \left( \frac{2}{\tau} y(a+b-c) \frac{(c-a)(c-b)(c-a+1)(c-b+1)}{(c-a-b)(c-a-b+1)} + \frac{2E_0^2\tau^2 \epsilon_\perp^2}{\omega_1^3} \right. \right. \right. \\ & \left. \left. \left. + \left( \omega_1 - \omega_0 - \frac{2E_0\tau P_1}{\omega_1} \right) \frac{(c-a)(c-b)}{(1+c-a-b)} \right) \right] \right|^2 \end{aligned} \quad (\text{A22})$$

We introduce it here in anticipation of encountering the Gamma function  $\Gamma(z)$  in the subsequent content. The Gamma function typically obeys the following relationship:

$$\Gamma(1+z) = z\Gamma(z), \quad \Gamma(1-z)\Gamma(z) = \frac{\pi}{\sin(\pi z)}, \quad (\text{A23})$$

from which we can derive the following useful relations,

$$|\Gamma(iz)|^2 = \frac{\pi}{z \sinh(\pi z)}, \quad |\Gamma(1 + iz)|^2 = \frac{\pi z}{\sinh(\pi z)}, \quad \left|\Gamma\left(\frac{1}{2} + iz\right)\right|^2 = \frac{\pi}{\cosh(\pi z)}. \quad (\text{A24})$$

Using the mathematical identities (A24), we can compute  $|\Gamma_1|^2$  and  $|\Gamma_2|^2$  as

$$\begin{aligned} |\Gamma_1|^2 &= \left| \frac{\Gamma(c)\Gamma(c-a-b-1)}{\Gamma(c-a)\Gamma(c-b)} \right|^2 \\ &= \frac{\omega_0(\omega_1 + \omega_0 + 2E_0\tau)}{\omega_1(\omega_1 + \omega_0 - 2E_0\tau)(1 + \tau^2\omega_1^2)} \left( \frac{\sinh\left(\frac{\pi\tau}{2}(\omega_0 + \omega_1 - 2E_0\tau)\right) \sinh\left(\frac{\pi\tau}{2}(\omega_0 + \omega_1 + 2E_0\tau)\right)}{\sinh(\pi\tau\omega_0) \sinh(\pi\tau\omega_1)} \right), \\ |\Gamma_2|^2 &= \left| \frac{\Gamma(c)\Gamma(a+b-c)}{\Gamma(a)\Gamma(b)} \right|^2 \\ &= \frac{\omega_0(\omega_0 - \omega_1 + 2E_0\tau)}{\omega_1(\omega_1 - \omega_0 + 2E_0\tau)(1 + \tau^2\omega_1^2)} \left( \frac{\sinh\left(\frac{\pi\tau}{2}(\omega_0 - \omega_1 + 2E_0\tau)\right) \sinh\left(\frac{\pi\tau}{2}(-\omega_0 + \omega_1 + 2E_0\tau)\right)}{\sinh(\pi\tau\omega_0) \sinh(\pi\tau\omega_1)} \right). \end{aligned} \quad (\text{A25})$$

When computing expressions like  $\Gamma_1\overline{\Gamma_2}$ , approximate methods prove advantageous. A frequently utilized technique entails utilizing Stirling's formula for the Gamma function, offering a simpler yet effective approach to assess the desired expression.

$$\Gamma(z) \approx z^{z-1/2} e^{-z} \sqrt{2\pi} \quad (\text{A26})$$

Then, we derive the set of equations employing Stirling's formula for the Gamma function, which are used to determine the Gamma function in the computation of the particle distribution function.

$$\begin{aligned} \Gamma(1 + ix) &\sim \sqrt{2\pi} e^{\left(\frac{1}{2}\ln(x) - \frac{\pi}{2}x\right) + i(x(\ln(x)-1) + \frac{\pi}{4})} \\ \Gamma(-ix) &\sim \sqrt{2\pi} e^{\left(\frac{\pi}{2}x - \frac{1}{2}\ln(x)\right) + i(x(1-\ln(x)) - \frac{\pi}{4})} \\ \Gamma(ix) &\sim \sqrt{2\pi} e^{\left(-\frac{\pi}{2}x - \frac{1}{2}\ln(x)\right) + i(x(\ln(x)-1) - \frac{\pi}{4})} \end{aligned} \quad (\text{A27})$$

So,

$$\Gamma_1\overline{\Gamma_2} = \left( \frac{\Gamma(c)\Gamma(c-a-b-1)}{\Gamma(c-a)\Gamma(c-b)} \right) \overline{\left( \frac{\Gamma(c)\Gamma(a+b-c)}{\Gamma(a)\Gamma(b)} \right)} \quad (\text{A28})$$

Subsequently, following certain algebraic manipulations, we obtain :

$$\Gamma_1\overline{\Gamma_2} \approx |\Gamma_1\overline{\Gamma_2}| e^{i\varphi} \quad (\text{A29})$$

Here,

$$|\Gamma_1 \bar{\Gamma}_2| = \frac{\omega_0}{2\omega_1} \frac{\exp(\pi\tau/2(\omega_0 - \omega_1 + 2E_0\tau))}{\sinh(\pi\tau\omega_0) \sqrt{1 + \omega_1^2\tau^2}} \sqrt{\frac{((\omega_0 + 2E_0\tau)^2 - \omega_1^2)}{(\omega_1^2 - (2E_0\tau - \omega_0)^2)}}, \quad (\text{A30})$$

$$\begin{aligned} \varrho = & \frac{\tau}{2}(\omega_0 + \omega_1 - 2E_0\tau) \ln(\tau(\omega_0 + \omega_1 - 2E_0\tau)) + (-\omega_0 + \omega_1 - 2E_0\tau) \ln(\tau(\omega_0 - \omega_1 + 2E_0\tau)) \\ & + (-\omega_0 + \omega_1 + 2E_0\tau) \ln(\tau(-\omega_0 + \omega_1 + 2E_0\tau)) + (\omega_0 + \omega_1 + 2E_0\tau) \ln(\tau(\omega_0 + \omega_1 + 2E_0\tau)) \\ & + \pi - \tan^{-1}(\tau\omega_1) - 2\tau\omega_1 \ln(2\omega_1\tau). \end{aligned} \quad (\text{A31})$$

Now, we use these approximations of the Gamma function to derive an approximate expression for the particle distribution function (59), which can then be re-expressed using Eq.(A22) as follows:

$$\begin{aligned} f(\mathbf{p}, y) \approx & |N^+(\mathbf{p})|^2 \left[ \frac{2}{\tau} y(a+b-c) \Gamma_2 e^{-i\tau\omega_1 \ln(1-y)} + (1-y) \left[ \Gamma_1 \left( \frac{2}{\tau} yab + i(c-a-b-1)(\omega_1 - \omega_0 - \frac{2E_0\tau P_1}{\omega_1}) \right) \right. \right. \\ & \left. \left. + \Gamma_2 e^{-i\tau\omega_1 \ln(1-y)} \left( \frac{2}{\tau} y(a+b-c) \frac{(c-a)(c-b)}{(c-a-b)} + i(\omega_1 - \omega_0 - \frac{2E_0\tau P_1}{\omega_1}) \right) \right] + (1-y)^2 \left[ \Gamma_1 \left( \frac{2}{\tau} yab \right. \right. \right. \\ & \left. \left. \frac{(1+a)(1+b)}{(2+a+b-c)} + i \left( \frac{2E_0^2\tau^2\epsilon_\perp^2}{\omega_1^3} + \frac{ab}{(1+a+b-c)} (\omega_1 - \omega_0 - \frac{2E_0\tau P_1}{\omega_1}) \right) (c-a-b-1) \right) \right. \\ & \left. \left. + \Gamma_2 e^{-i\tau\omega_1 \ln(1-y)} \left( \frac{2}{\tau} y(a+b-c) \frac{(c-a)(c-b)(c-a+1)(c-b+1)}{(c-a-b)(c-a-b+1)} + \frac{2E_0^2\tau^2\epsilon_\perp^2}{\omega_1^3} \right. \right. \right. \\ & \left. \left. \left. + (\omega_1 - \omega_0 - \frac{2E_0\tau P_1}{\omega_1}) \frac{(c-a)(c-b)}{(1+c-a-b)} \right) \right] \right] \left( 1 + \frac{P(p_{\parallel}, y)}{\omega(\mathbf{p}, y)} \right) \end{aligned} \quad (\text{A32})$$

We aim to express  $f(\mathbf{p}, y)$  in a series involving  $(1-y)$ . We can then consider truncating higher-order terms to simplify the analysis while still capturing essential features. In this context, we focus exclusively on terms up to the  $(1-y)^2$  order, disregarding higher-order terms in Eq. (A32). This approach is sufficient to explain the interesting results discussed in the later section IV. To accomplish this, we again approximate the quantity  $\left(1 + \frac{P(p_{\parallel}, y)}{\omega(\mathbf{p}, y)}\right)$  using the Taylor series expansion near  $y \rightarrow 1$ . This yields:

$$1 + \frac{P(p_{\parallel}, y)}{\omega(\mathbf{p}, y)} \approx \Omega_0 + (1-y)\Omega_1 + (1-y)^2\Omega_2 \quad (\text{A33})$$

with,

$$\Omega_0 = 1 + \frac{P_1}{\omega_1}; \quad (\text{A34})$$

$$\Omega_1 = \frac{-2E_0\tau}{\omega_1^3} \epsilon_{\perp}^2(p_{\perp}); \quad (\text{A35})$$

$$\Omega_2 = \frac{-6E_0^2\tau^2}{\omega_1^5} P_1 \epsilon_{\perp}^2(p_{\perp}). \quad (\text{A36})$$

Therefore, we can express the particle distribution function approximately in terms of the small parameter  $(1 - y)$  up to the second order. The expression is given by:

$$f(\mathbf{p}, y) \approx |N^+(\mathbf{p})|^2 \left( C_0(\mathbf{p}, y) + (1 - y)C_1(\mathbf{p}, y) + (1 - y)^2 C_2(\mathbf{p}, y) \right) \quad (\text{A37})$$

where,

$$C_0(\mathbf{p}, y) = 4y^2 \Omega_0 \omega_1^2 |\Gamma_2|^2 \quad (\text{A38})$$

$$C_1(\mathbf{p}, y) = 4y \Omega_0 |\Gamma_1 \overline{\Gamma_2}| E_0 \tau (P_1 - \omega_1) \cos(\Upsilon) + 4y |\Gamma_2|^2 (2\Omega_0 (\omega_1^2 - \omega_0 \omega_1 + (\omega_1 - P_1) E_0 \tau) + \Omega_1 \omega_1^2 y) \quad (\text{A39})$$

$$\begin{aligned}
\mathbf{C}_2(\mathbf{p}, y) = & \Omega_0(P_1 - \omega_1)^2 \frac{4E_0^2 \tau^2}{\omega_1^2} |\Gamma_1|^2 + |\Gamma_2|^2 \left[ 8\Omega_1 y (2E_0 \tau (\omega_1 - P_1) - \omega_0 \omega_1 + \omega_1^2) - 8\Omega_0 y (\omega_1 + P_1) \right. \\
& (\omega_1 - \omega_0 + 2E_0 \tau) + 4\Omega_2 y^2 \omega_1^2 + \Omega_0 \left( \frac{4}{\omega_1^2} (\omega_1^2 + E_0 \tau (\omega_1 - P_1))^2 + \frac{\tau^2}{4} ((\omega_0 + \omega_1)^2 - 4E_0^2 \tau^2)^2 y^2 \right) \\
& + \frac{y \Omega_0}{2\omega_1^2 (1 + \tau^2 \omega_1^2)} \left( 2\omega_1^2 \tau^2 ((\omega_0 - \omega_1) \omega_1 + 2E_0 \tau P_1) (\omega_0^2 - (\omega_1 + 2E_0 \tau)^2) \right. \\
& + y \omega_1^3 (16(\omega_0 + \omega_1) + 32E_0 \tau - 4(2\omega_0 - 3\omega_1)(\omega_0 + \omega_1)^2 \tau^2 + 8E_0 \tau^3 \omega_1 (2\omega_0 + 3\omega_1) \\
& - \tau^4 (\omega_1 (\omega_0 + \omega_1)^4 - 16E_0^2 (2\omega_0 + \omega_1)) + 32E_0^3 \tau^5 + 8E_0^2 \tau^6 \omega_1 (\omega_0 + \omega_1)^2 - 16E_0^4 \tau^8 \omega_1) \\
& \left. + 16E_0^2 \tau^2 \epsilon_{\perp}^2 (1 + \tau^2 \omega_1^2) \right] + \frac{|\Gamma_1 \overline{\Gamma_2}| \cos(\Upsilon)}{2\omega_1^2 (4 + \omega_1^2 \tau^2)} \left( -16E_0^4 \Omega_0 \omega_1^4 \tau^8 y^2 \right. \\
& + 16E_0^3 \Omega_0 \omega_1^2 \tau^5 y (P_1 (4 + \omega_1^2 \tau^2) - 4\omega_1 y) + \Omega_0 \omega_1^2 (-\omega_0 + \omega_1) y (2(-8(\omega_1 + P_1) \\
& + (\omega_0 - \omega_1)^2 \omega_1 \tau^2) (4 + \omega_1^2 \tau^2) + \omega_1 (32 - 4(\omega_0 - \omega_1)(4\omega_0 + \omega_1) \tau^2 + (\omega_0 - \omega_1)^3 \omega_1 \tau^4) y) \\
& + 8E_0^2 \Omega_0 \tau^2 (-2(\omega_1 - P_1)^2 (4 + \omega_1^2 \tau^2) - (4 + \omega_1^2 \tau^2) (-2P_1^2 + \omega_1^2 (2 + \omega_1 (-\omega_0 + \omega_1) \tau^2)) y \\
& + \omega_1^3 \tau^2 (-8\omega_0 + 6\omega_1 + (\omega_0 - \omega_1)^2 \omega_1 \tau^2) y^2) + 4E_0 \omega_1^2 \tau (-4\Omega_0 (\omega_1 - P_1) (4 + \omega_1^2 \tau^2) \\
& - (4 + \omega_1^2 \tau^2) (4\Omega_1 (\omega_1 - P_1) - 8\Omega_0 (\omega_1 + P_1) + \Omega_0 (\omega_0 - \omega_1)^2 P_1 \tau^2) y \\
& \left. - 4\Omega_0 \omega_1 (4 + (-\omega_0^2 + \omega_1^2) \tau^2) y^2) \right) + \frac{|\Gamma_1 \overline{\Gamma_2}| \Omega_0 \tau y}{(\omega_1 (4 + \omega_1^2 \tau^2))} \left( 2(4 + \omega_1^2 \tau^2) (\omega_1^3 (2 + \omega_1) \right. \\
& - E_0 \omega_1^2 (\omega_1 + 3P_1) \tau + 4E_0^2 (\omega_1^2 + \omega_1 (-2 + P_1) - P_1^2) \tau^2 + 4E_0^3 (-\omega_1 + P_1) \tau^3) \\
& + \omega_0^4 \omega_1^2 \tau^2 y - \omega_1^2 (\omega_1 - 2E_0 \tau) (12\omega_1 + 8E_0 \tau + 3\omega_1^3 \tau^2 + 2E_0 \omega_1^2 \tau^3 - 4E_0^2 \omega_1 \tau^4 + 8E_0^3 \tau^5) y \\
& + 4\omega_0 \omega_1^2 (4 + \omega_1^2 \tau^2) (-2 + \omega_1 y) + 2\omega_0^2 ((\omega_1 (2 + \omega_1) + E_0 (\omega_1 - P_1) \tau) (4 + \omega_1^2 \tau^2) \\
& \left. - y \omega_1^2 (10 + 3\omega_1^2 \tau^2 - 2E_0 \omega_1 \tau^3 + 4E_0^2 \tau^4)) \right) \sin(\Upsilon) \tag{A40}
\end{aligned}$$

$$\begin{aligned}
\mathbf{C}_2(\mathbf{p}, y) = & \Omega_0(P_1 - \omega_1)^2 \frac{4E_0^2 \tau^2}{\omega_1^2} |\Gamma_1|^2 + |\Gamma_2|^2 \left[ 8\Omega_1 y (2E_0 \tau (\omega_1 - P_1) - \omega_0 \omega_1 + \omega_1^2) \right. \\
& \left. + 4\Omega_2 y^2 \omega_1^2 + \frac{\Omega_0}{4\omega_1^2 (1 + \tau^2 \omega_1^2)} \sigma_0 \right] + \frac{|\Gamma_1 \overline{\Gamma_2}|}{2\omega_1^2 (4 + \omega_1^2 \tau^2)} (\cos(\Upsilon) \sigma_1 + \sin(\Upsilon) \sigma_2) \tag{A41}
\end{aligned}$$

Here,

$$\Upsilon = \varrho + \tau\omega_1 \ln(1 - y), \quad (\text{A42})$$

$$\begin{aligned} \sigma_0 = & \left( 16(\omega_1^2 + E_0(\omega_1 - P_1)\tau)^2(1 + \omega_1^2\tau^2) - \right. \\ & 4(-8(\omega_0 - \omega_1)\omega_1^2(\omega_1 + P_1) + 16E_0\omega_1^2(\omega_1 + P_1)\tau + \\ & (8E_0^2(-\omega_1^2 + P_1^2) - (\omega_0 - \omega_1)\omega_1^3(\omega_0^2 + \omega_1(7\omega_1 + 8P_1)))\tau^2 + \\ & 2E_0\omega_1^2(\omega_0 + 3\omega_1)(2\omega_1^2 - \omega_0P_1 + 3\omega_1P_1)\tau^3 + \\ & 4E_0^2\omega_1^2((\omega_0 - 3\omega_1)\omega_1 + 2\omega_1P_1 + 2P_1^2)\tau^4 + 8E_0^3\omega_1^2P_1\tau^5)y + \\ & \omega_1^2(32\omega_1(\omega_0 + \omega_1) + 64E_0\omega_1\tau + (\omega_0 + \omega_1)^2(\omega_0^2 - 14\omega_0\omega_1 + 25\omega_1^2)\tau^2 + \\ & 16E_0\omega_1^2(2\omega_0 + 3\omega_1)\tau^3 - (\omega_1^2(\omega_0 + \omega_1)^4 + 8E_0^2(\omega_0^2 - 6\omega_0\omega_1 - 3\omega_1^2))\tau^4 + \\ & \left. 64E_0^3\omega_1\tau^5 + 8E_0^2(2E_0^2 + \omega_1^2(\omega_0 + \omega_1)^2)\tau^6 - 16E_0^4\omega_1^2\tau^8)y^2 \right), \quad (\text{A43}) \end{aligned}$$

$$\begin{aligned} \sigma_1 = & 16E_0^3\Omega_0\omega_1^2\tau^5y(P_1(4 + \omega_1^2\tau^2) - 4\omega_1y) - 16E_0^4\Omega_0\omega_1^4\tau^8y^2 + \Omega_0\omega_1^2(-\omega_0 + \omega_1)y(2(-8(\omega_1 + P_1) \\ & + (\omega_0 - \omega_1)^2\omega_1\tau^2)(4 + \omega_1^2\tau^2) + \omega_1(32 - 4(\omega_0 - \omega_1)(4\omega_0 + \omega_1)\tau^2 + (\omega_0 - \omega_1)^3\omega_1\tau^4)y) \\ & + 8E_0^2\Omega_0\tau^2(-2(\omega_1 - P_1)^2(4 + \omega_1^2\tau^2) - (4 + \omega_1^2\tau^2)(-2P_1^2 + \omega_1^2(2 + \omega_1(-\omega_0 + \omega_1)\tau^2)))y \\ & + \omega_1^3\tau^2(-8\omega_0 + 6\omega_1 + (\omega_0 - \omega_1)^2\omega_1\tau^2)y^2) + 4E_0\omega_1^2\tau(-4\Omega_0(\omega_1 - P_1)(4 + \omega_1^2\tau^2) \\ & - (4 + \omega_1^2\tau^2)(4\Omega_1(\omega_1 - P_1) - 8\Omega_0(\omega_1 + P_1) + \Omega_0(\omega_0 - \omega_1)^2P_1\tau^2)y \\ & - 4\Omega_0\omega_1(4 + (-\omega_0^2 + \omega_1^2)\tau^2)y^2) \quad (\text{A44}) \end{aligned}$$

$$\begin{aligned} \sigma_2 = & 2(4 + \omega_1^2\tau^2)(\omega_1^3(2 + \omega_1) - E_0\omega_1^2(\omega_1 + 3P_1)\tau \\ & + 4E_0^2(\omega_1^2 + \omega_1(-2 + P_1) - P_1^2)\tau^2 + 4E_0^3(-\omega_1 + P_1)\tau^3) \\ & + \omega_0^4\omega_1^2\tau^2y - \omega_1^2(\omega_1 - 2E_0\tau)(12\omega_1 + 8E_0\tau + 3\omega_1^3\tau^2 + 2E_0\omega_1^2\tau^3 - 4E_0^2\omega_1\tau^4 + 8E_0^3\tau^5)y \\ & + 4\omega_0\omega_1^2(4 + \omega_1^2\tau^2)(-2 + \omega_1y) + 2\omega_0^2((\omega_1(2 + \omega_1) + E_0(\omega_1 - P_1)\tau)(4 + \omega_1^2\tau^2) \\ & - y\omega_1^2(10 + 3\omega_1^2\tau^2 - 2E_0\omega_1\tau^3 + 4E_0^2\tau^4)) \quad (\text{A45}) \end{aligned}$$

### 3. Research Data

This section is included to provide complete clarity on the numerically generated simulation data. As outlined in Section IV B, we solved the Dirac equation for homogeneous electric fields in Section III to determine the relevant time scales for understanding the dynamics of pair production in a time-dependent electric field.

a. *Longitudinal Momentum spectrum*

As discussed in the section on the LMS of created particles, we provide a quantitative estimation to identify the relevant time scales for the dynamics of the longitudinal momentum distribution function, which exhibits distinct behaviors and substructures. The time scales for various values of the electric field parameters are summarized in Tables.

Specifically, one table is provided for each time scale: time scale  $t_{cp}$  is analyzed in Table IV, time scale  $t_{sep}$  in Table V, and time scale  $t_{dis}$  in Table VI.

	0.2	0.3	0.4
7	15.272	9.68	6.2
9	22	12.2	8.3
11	25.64	15.84	11.19
13	30.19	18.56	12.03
15	38.5	21.5	12.05
17	40	22	12
19	44	23.4	14
21	51.3	28.5	15
23	57.9	33.6	18

Table IV: Numerical data regarding the time scale  $t_{cp}$  (Central Peak Formation in distribution function) obtained by evaluating the function  $f(p_{\parallel}, t)$  for a homogeneous Sauter pulse,  $E(t) = E_0 \text{sech}^2\left(\frac{t}{\tau}\right)$ , at different times. The field strengths  $E_0$  are given in the first row in terms of the critical field strength  $E_c$  and the pulse lengths  $\tau$  along the first column in units of [ $m^{-1}$ ].

	0.2	0.3	0.4
7	18.143	12.63	9.5
9	25.1	16.92	12.64
11	31.94	21.09	15.58
13	38.56	25.36	18.67
15	45.4	29.65	21.8
17	51.5	33.5	24.6
19	57.9	37.53	27.4
21	64.2	41.8	31
23	70.6	45.6	33

Table V: Numerical data regarding the time scale  $t_{sep}$  (Peak Separation): At this time, the central peak becomes dominant or the time after the two peaks become distinctly separated. Data obtained by evaluating the function  $f(p_{\parallel}, t)$  for a homogeneous Sauter pulse,  $E(t) = E_0 \text{sech}^2\left(\frac{t}{\tau}\right)$ , at different times. The field strengths  $E_0$  are given in the first row in terms of the critical field strength  $E_c$  and the pulse lengths  $\tau$  along the first column in units of [ $m^{-1}$ ].

	0.2	0.3	0.4
7	35.143	27.263	24.5
9	47	34.2	30.11
11	56.64	40.29	34.88
13	63.56	47.36	38.56
15	77.8	58	42.2
17	80.5	55.5	43.26
19	88.9	59.52	47.74
21	97.2	68.9	51.2
23	112.6	79.8	76

Table VI: Numerical data regarding the time scale  $t_{dis}$  (Disappearance of Oscillation): This indicates the time when the oscillations within the central peak fade away or the time after the primary peak (or the left-side peak) ceases to exist. Data obtained by evaluating the function  $f(p_{\parallel}, t)$  for a homogeneous Sauter pulse,  $E(t) = E_0 \text{sech}^2\left(\frac{t}{\tau}\right)$ , at different times. The field strengths  $E_0$  are given in the first row in terms of the critical field strength  $E_c$  and the pulse lengths  $\tau$  along the first column in units of [ $m^{-1}$ ].

*b. Transverse Momentum spectrum*

As discussed in the section on TMS of created particles, we provide a quantitative estimation to determine the relevant time scales for the dynamics of the transverse momentum distribution function, which exhibits different behaviors and substructure. We present the time scale for different values of the electric field parameters. It is these data sets and the quality of the fits that have been tabulated here. Specifically, we have generated one table for each time scale; time scale  $T_1$  is analyzed in Tab.VII, time scale  $T_2$  is analyzed in Tab. VIII, and time scale  $T_3$  is analyzed in Tab. IX, respectively.

	0.2	0.3	0.4	0.2	0.3	0.4
7	7.2	2.4	1.98	0.013	0.339	0.075
10	6.9	4.3	2.6	0.048	0.240	0.284
13	6.8	2.6	1.95	0.076	0.273	0.034
16	9	4	1.88	0.179	0.165	0.011
19	6.75	2.3	1.92	0.103	0.464	0.001

Table VII: Numerical data regarding the time scale  $T_1$  (smooth spectrum begins to reveal an interference pattern, manifesting as a multi-peak structure centered around a non-zero momentum) obtained by evaluating the function  $f(p_{\parallel}, t)$  for a homogeneous Sauter pulse,  $E(t) = E_0 \text{sech}^2\left(\frac{t}{\tau}\right)$ , at different times. The field strengths  $E_0$  are given in the first row in terms of the critical field strength  $E_c$  and the pulse lengths  $\tau$  along the first column in units of [ $m^{-1}$ ]. The absolute values obtained are shown on the left and in units of [ $m^{-1}$ ], as are the relative deviations from our fit  $0.28\tau^{0.05}E_0^{-1.96}$  on the right.



	0.2	0.3	0.4	0.2	0.3	0.4
7	15.5	6.8	4.3	0.044	0.141	0.298
10	17.4	6.7	4.5	0.062	0.087	0.162
13	22.7	8.9	4.39	0.041	0.035	0.010
16	21.6	9.3	4.78	0.146	0.050	0.055
19	30	11.1	4.5	0.081	0.021	0.247

Table VIII: Numerical data regarding the time scale  $T_2$  (multi-peak structure in TMS) obtained by evaluating the function  $f(p_{\parallel}, t)$  for a homogeneous Sauter pulse,  $E(t) = E_0 \text{sech}^2\left(\frac{t}{\tau}\right)$ , at different times. The field strengths  $E_0$  are given in the first row in terms of the critical field strength  $E_c$  and the pulse lengths  $\tau$  along the first column in units of [ $m^{-1}$ ]. The absolute values obtained are shown on the left and in units of [ $m^{-1}$ ], as are the relative deviations from our fit  $0.11\tau^{0.63}E_0^{-2.3}$  on the right.

	0.2	0.3	0.4	0.2	0.3	0.4
7	26	18	10.2	0.143	0.201	0.156
10	35.4	19.5	10.4	0.002	0.123	0.017
13	43	18	10.2	0.067	0.078	0.137
16	47	15	9.2	0.057	0.430	0.393
19	45	29	14.8	0.069	0.196	0.058

Table IX: Numerical data regarding the time scale  $T_1$  (small peaks at finite momenta gradually diminish over this time scale in the particle distribution related real particle) obtained by evaluating the function  $f(p_{\parallel}, t)$  for a homogeneous Sauter pulse,  $E(t) = E_0 \text{sech}^2\left(\frac{t}{\tau}\right)$ , at different times. The field strengths  $E_0$  are given in the first row in terms of the critical field strength  $E_c$  and the pulse lengths  $\tau$  along the first column in units of [ $m^{-1}$ ]. The absolute values obtained are shown on the left and in units of [ $m^{-1}$ ], as are the relative deviations from our fit  $0.66\tau^{0.49}E_0^{-1.79}$  on the right.

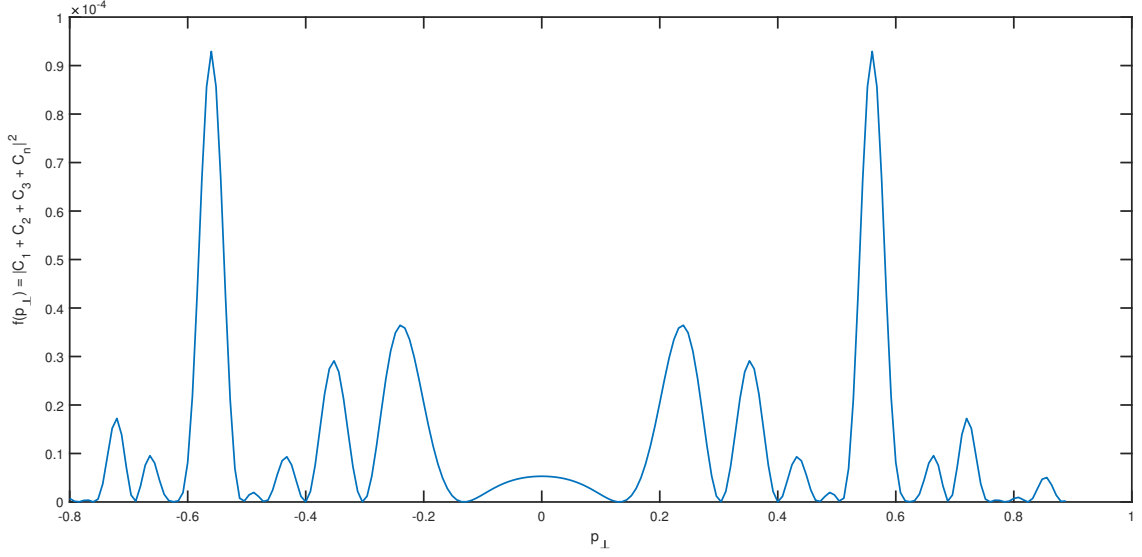


Figure 20: Total Probability of pair production at time  $t = 15[m^{-1}]$ , where  $-3 < \nu < 3$ ,  $E_0 = 0.2E_c$ , and  $\tau = 10[m^{-1}]$ .

#### 4. Fourier analysis

To analyze the transverse momentum spectrum at finite time using the Fourier analysis, we decompose the time-dependent electric field  $E(t)$  into cosine and sine components.

$$E(t) = \frac{1}{(2\pi)} \int \tilde{E}(\nu) e^{i\nu t} d\nu \quad (\text{A46})$$

where,

$$\tilde{E}(\nu) = \int_{t_{in}=-5\tau}^{t_{out}} E(t) e^{-i\nu t} dt \quad (\text{A47})$$

We replace the continuous integration with a discrete one to analyze the behavior of the electric field in a two-level system of pair production [102].

$$E(t) = \sum_i \tilde{E}(\nu_i) e^{i\nu_i t} \quad (\text{A48})$$

We calculate the frequency  $\nu$  using the Eq. (A47) at some time, and the total probability can be compute by absolute sum of different amplitude of pair production due to different  $\nu_i$  at the finite

time  $t = t_{\text{out}}$  and plot the total probability as the function of  $p_{\perp}$  as shown in Fig.20.

- 
- [1] P. A. M. Dirac, Proc. Roy. Soc. Lond. A **117**, 610 (1928).
  - [2] F. Sauter, Z. Phys. **69**, 742 (1931).
  - [3] W. Heisenberg and H. Euler, Z. Phys. **98**, 714 (1936), physics/0605038.
  - [4] J. S. Schwinger, Phys. Rev. **82**, 664 (1951).
  - [5] F. Sauter, Z. Phys. **73**, 547 (1932).
  - [6] W. Greiner, B. Müller, and J. Rafelski, *Quantum Electrodynamics of Strong Fields* (Springer Berlin Heidelberg, Berlin, Heidelberg, 1985).
  - [7] L. Parker, Phys. Rev. Lett. **21**, 562 (1968).
  - [8] S. W. Hawking, Commun. Math. Phys. **43**, 199 (1975), [Erratum: Commun.Math.Phys. 46, 206 (1976)].
  - [9] M. K. Parikh and F. Wilczek, Phys. Rev. Lett. **85**, 5042 (2000), hep-th/9907001.
  - [10] W. G. Unruh, Phys. Rev. D **14**, 870 (1976).
  - [11] S. P. Kim, Int. J. Mod. Phys. D **25**, 1645005 (2016), 1602.05336.
  - [12] V. S. Popov, Zh. Eksp. Teor. Fiz. **61**, 1334 (1971).
  - [13] M. S. Marinov and V. S. Popov, Fortsch. Phys. **25**, 373 (1977).
  - [14] L. V. Keldysh, J. Exp. Theor. Phys. **20**, 1307 (1965).
  - [15] A. I. Nikishov, Zh. Eksp. Teor. Fiz. **57**, 1210 (1969).
  - [16] N. B. Narozhnyi and A. I. Nikishov, Yad. Fiz. **11**, 1072 (1970).
  - [17] A. Nikishov, arXiv preprint hep-th/0111137 (2001).
  - [18] E. Brezin and C. Itzykson, Phys. Rev. D **2**, 1191 (1970).
  - [19] V. G. Bagrov, D. M. Gitman, and S. M. Shvartsman, Zh. Eksp. Teor. Fiz. **68**, 392 (1975).
  - [20] V. M. Mostepanenko and V. M. Frolov, Yad. Fiz. **19**, 885 (1974).
  - [21] N. B. Narozhnyi and A. I. Nikishov, Zh. Eksp. Teor. Fiz., v. 65, no. 3, pp. 862-874 (1973), URL <https://www.osti.gov/biblio/4400849>.
  - [22] J. Andruszkow et al. (TESLA), Phys. Rev. Lett. **85**, 3825 (2000), physics/0006010.
  - [23] T. Heinzl and A. Ilderton, Eur. Phys. J. D **55**, 359 (2009), 0811.1960.
  - [24] G. V. Dunne, Eur. Phys. J. D **55**, 327 (2009), 0812.3163.
  - [25] E. Khazanov and et al., High Power Laser Science and Engineering p. 1–77 (2023).
  - [26] D. Allor, T. D. Cohen, and D. A. McGady, Phys. Rev. D **78**, 096009 (2008), 0708.1471.

- [27] G. L. Klimchitskaya and V. M. Mostepanenko, Phys. Rev. D **87**, 125011 (2013), 1305.5700.
- [28] F. Fillion-Gourdeau and S. MacLean, Phys. Rev. B **92**, 035401 (2015).
- [29] B. S. DeWitt, Phys. Rept. **19**, 295 (1975).
- [30] E. Mottola, Phys. Rev. D **31**, 754 (1985).
- [31] T. N. Tomaras, N. C. Tsamis, and R. P. Woodard, JHEP **11**, 008 (2001), hep-th/0108090.
- [32] T. N. Tomaras, N. C. Tsamis, and R. P. Woodard, Phys. Rev. D **62**, 125005 (2000), hep-ph/0007166.
- [33] S. P. Gavrilov and D. M. Gitman, Phys. Rev. D **53**, 7162 (1996), hep-th/9603152.
- [34] J. Hallin and P. Liljenberg, Phys. Rev. D **52**, 1150 (1995), hep-th/9412188.
- [35] H. M. Fried and R. P. Woodard, Phys. Lett. B **524**, 233 (2002), hep-th/0110180.
- [36] J. Avan, H. M. Fried, and Y. Gabellini, Phys. Rev. D **67**, 016003 (2003), hep-th/0208053.
- [37] A. Ilderton, JHEP **09**, 166 (2014), 1406.1513.
- [38] P. Zhuang and U. W. Heinz, Annals Phys. **245**, 311 (1996), nucl-th/9502034.
- [39] F. Hebenstreit, A. Ilderton, and M. Marklund, Phys. Rev. D **84**, 125022 (2011), 1109.3712.
- [40] F. Hebenstreit, A. Ilderton, M. Marklund, and J. Zamanian, Phys. Rev. D **83**, 065007 (2011), 1011.1923.
- [41] S. A. Smolyansky, A. V. Prozorkevich, S. M. Schmidt, D. Blaschke, G. Roepke, and V. D. Toneev, Int. J. Mod. Phys. E **7**, 515 (1998), nucl-th/9709057.
- [42] I. K. Affleck, O. Alvarez, and N. S. Manton, Nucl. Phys. B **197**, 509 (1982).
- [43] S. P. Kim and D. N. Page, Phys. Rev. D **65**, 105002 (2002), hep-th/0005078.
- [44] R. Alkofer, M. B. Hecht, C. D. Roberts, S. M. Schmidt, and D. V. Vinnik, Phys. Rev. Lett. **87**, 193902 (2001), nucl-th/0108046.
- [45] C. D. Roberts, S. M. Schmidt, and D. V. Vinnik, Phys. Rev. Lett. **89**, 153901 (2002), nucl-th/0206004.
- [46] A. Di Piazza, Phys. Rev. D **70**, 053013 (2004).
- [47] M. Melike, X. Bai-Song, and D. Sayipjama, Communications in Theoretical Physics **57**, 422 (2012).
- [48] A. Ilderton, Phys. Rev. D **105**, 016021 (2022), 2108.13885.
- [49] T. C. Adorno, S. P. Gavrilov, and D. M. Gitman, Int. J. Mod. Phys. A **32**, 1750105 (2017), 1512.01288.
- [50] D. Blaschke, L. Juchnowski, A. Panferov, and S. Smolyansky, Phys. Part. Nucl. **46**, 797 (2015), 1412.6372.
- [51] D. B. Blaschke, S. A. Smolyansky, A. Panferov, and L. Juchnowski, in *Quantum Field Theory at the Limits: from Strong Fields to Heavy Quarks* (2017), pp. 1–23, 1704.04147.
- [52] C. Banerjee and M. P. Singh, Phys. Rev. D **105**, 076021 (2022), 1807.06951.

- [53] C. Banerjee and M. P. Singh, Phys. Rev. D **100**, 056016 (2019), 1809.06901.
- [54] M. A. Zubkov, Pisma Zh. Eksp. Teor. Fiz. **95**, 540 (2012), 1204.0138.
- [55] S. P. Gavrilov, D. M. Gitman, and N. Yokomizo, Phys. Rev. D **86**, 125022 (2012), 1207.1749.
- [56] P. Solinas, A. Amoretti, and F. Giazotto, Phys. Rev. Lett. **126**, 117001 (2021), 2007.08323.
- [57] V. Kasper, F. Hebenstreit, M. Oberthaler, and J. Berges, Phys. Lett. B **760**, 742 (2016), 1506.01238.
- [58] J. C. Halimeh, M. Aidelsburger, F. Grusdt, P. Hauke, and B. Yang, Nature Phys. **21**, 25 (2025), 2310.12201.
- [59] R. Schützhold (2025), 2501.03785.
- [60] G. V. Dunne and T. Hall, Phys. Rev. D **58**, 105022 (1998), hep-th/9807031.
- [61] A. B. Balantekin, J. E. Seger, and S. H. Fricke, Int. J. Mod. Phys. A **6**, 695 (1991).
- [62] A. I. Nikishov, Phys. Atom. Nucl. **67**, 1478 (2004), hep-th/0304174.
- [63] P. Levai and V. Skokov, Phys. Rev. D **82**, 074014 (2010), 0909.2323.
- [64] S. A. Smolyansky, A. D. Panferov, D. B. Blaschke, L. Juchnowski, B. Kämpfer, and A. Otto, Russ. Phys. J. **59**, 1731 (2017), 1607.08775.
- [65] A. Otto, T. Nusch, D. Seipt, B. Kämpfer, D. Blaschke, A. D. Panferov, S. A. Smolyansky, and A. I. Titov, J. Plasma Phys. **82**, 655820301 (2016), 1604.00196.
- [66] T. Nusch, A. Otto, D. Seipt, B. Kämpfer, A. I. Titov, D. Blaschke, A. D. Panferov, and S. A. Smolyansky, FIAS Interdisc. Sci. Ser. pp. 253–262 (2017), 1604.00201.
- [67] D. Sah and M. P. Singh, arXiv e-prints arXiv:2301.06545 (2023), 2301.06545.
- [68] D. Sah and M. P. Singh, Springer Proc. Phys. **304**, 1023 (2024).
- [69] M. Diez, R. Alkofer, and C. Kohlfürst, Phys. Lett. B **844**, 138063 (2023), 2211.07510.
- [70] A. A. Grib, S. G. Mamayev, and V. M. Mostepanenko, *Vacuum quantum effects in strong fields* (Friedman Laboratory Publ. St. Petersburg, St. Petersburg, 1994).
- [71] A. A. Grib, V. M. Mostepanenko, and V. M. Frolov, Theoretical and Mathematical Physics **13**, 1207 (1972), ISSN 1573-9333, URL <https://doi.org/10.1007/BF01036146>.
- [72] L. H. Ryder, *Quantum Field Theory* (Cambridge University Press, 1996), ISBN 978-0-521-47814-4, 978-1-139-63239-3, 978-0-521-23764-2.
- [73] R. P. Feynman and M. Gell-Mann, Phys. Rev. **109**, 193 (1958).
- [74] S. M. Schmidt, D. Blaschke, G. Ropke, S. A. Smolyansky, A. V. Prozorkevich, and V. D. Toneev, Int. J. Mod. Phys. E **7**, 709 (1998), hep-ph/9809227.
- [75] K. Nakajima, AIP Conf. Proc. **737**, 614 (2004).
- [76] D. B. Blaschke, A. V. Prozorkevich, G. Ropke, C. D. Roberts, S. M. Schmidt, D. S. Shkirmanov, and

- S. A. Smolyansky, Eur. Phys. J. D **55**, 341 (2009), 0811.3570.
- [77] F. Hebenstreit, R. Alkofer, and H. Gies, Phys. Rev. D **82**, 105026 (2010), 1007.1099.
- [78] C. Kohlfurst, M. Mitter, G. von Winckel, F. Hebenstreit, and R. Alkofer, Phys. Rev. D **88**, 045028 (2013), 1212.1385.
- [79] R. Dabrowski and G. V. Dunne, Phys. Rev. D **94**, 065005 (2016), 1606.00902.
- [80] F. Gelis and N. Tanji, Prog. Part. Nucl. Phys. **87**, 1 (2016), 1510.05451.
- [81] I. Bialynicki-Birula and L. Rudnicki, Phys. Rev. D **83**, 065020 (2011), 1103.2666.
- [82] M. Abramowitz and I. A. Stegun, *Handbook of Mathematical Functions with Formulas, Graphs, and Mathematical Tables* (Dover, New York, 1964), ninth dover printing ed.
- [83] D. B. Blaschke, V. V. Dmitriev, G. Ropke, and S. A. Smolyansky, Phys. Rev. D **84**, 085028 (2011), 1105.5397.
- [84] A. M. Fedotov, E. G. Gelfer, K. Y. Korolev, and S. A. Smolyansky, Phys. Rev. D **83**, 025011 (2011), 1008.2098.
- [85] S. A. Smolyansky, D. B. Blaschke, A. V. Chertilin, G. Roepke, and A. V. Tarakanov (2010), 1012.0559.
- [86] D. B. Blaschke, A. V. Prozorkevich, C. D. Roberts, S. M. Schmidt, and S. A. Smolyansky, Phys. Rev. Lett. **96**, 140402 (2006), nucl-th/0511085.
- [87] D. B. Blaschke, G. Ropke, S. M. Schmidt, S. A. Smolyansky, and A. V. Tarakanov, Contrib. Plasma Phys. **51**, 451 (2011), 1006.1098.
- [88] D. B. Blaschke, G. Ropke, V. V. Dmitriev, S. A. Smolyansky, and A. V. Tarakanov (2011), 1101.6021.
- [89] A. Di Piazza, K. Z. Hatsagortsyan, and C. H. Keitel, Phys. Rev. Lett. **97**, 083603 (2006), hep-ph/0602039.
- [90] N. D. Birrell and P. C. W. Davies, *Quantum Fields in Curved Space*, Cambridge Monographs on Mathematical Physics (Cambridge University Press, 1982).
- [91] G. Gregori, D. Blaschke, P. Rajeev, H. Chen, R. Clarke, T. Huffman, C. Murphy, A. Prozorkevich, C. Roberts, G. Röpke, et al., High Energy Density Physics **6**, 166 (2010).
- [92] M. Baudisch, A. Marini, J. D. Cox, T. Zhu, F. Silva, S. Teichmann, M. Massicotte, F. Koppens, L. S. Levitov, F. J. García de Abajo, et al., Nature Communications **9**, 1018 (2018).
- [93] I. Gierz, J. C. Petersen, M. Mitrano, C. Cacho, I. E. Turcu, E. Springate, A. Stöhr, A. Köhler, U. Starke, and A. Cavalleri, Nature materials **12**, 1119 (2013).
- [94] B. Shen, Z. Bu, J. Xu, T. Xu, L. Ji, R. Li, and Z. Xu, Plasma Physics and Controlled Fusion **60**, 044002 (2018).

- [95] J. Kawanaka, K. Tsubakimoto, H. Yoshida, K. Fujioka, Y. Fujimoto, S. Tokita, T. Jitsuno, N. Miyanaga, and G.-E. D. Team, in *Journal of Physics: Conference Series* (IOP Publishing, 2016), vol. 688, p. 012044.
- [96] K. Tanaka, K. Spohr, D. Balabanski, S. Balascuta, L. Capponi, M. Cernaianu, M. Cuciuc, A. Cuciuc, I. Dancus, A. Dhal, et al., *Matter and Radiation at Extremes* **5** (2020).
- [97] S. A. Smolyansky, D. V. Churochkin, V. V. Dmitriev, A. D. Panferov, and B. Kämpfer, *EPJ Web Conf.* **138**, 06004 (2017).
- [98] S. M. Schmidt, D. Blaschke, G. Ropke, A. V. Prozorkevich, S. A. Smolyansky, and V. D. Toneev, *Phys. Rev. D* **59**, 094005 (1999), hep-ph/9810452.
- [99] C. K. Dumlu and G. V. Dunne, *Phys. Rev. D* **83**, 065028 (2011), 1102.2899.
- [100] H. K. Avetissian, A. K. Avetissian, G. F. Mkrtchian, and K. V. Sedrakian, *Phys. Rev. E* **66**, 016502 (2002).
- [101] H. Taya, H. Fujii, and K. Itakura, *Phys. Rev. D* **90**, 014039 (2014), 1405.6182.
- [102] K. Krajewska and J. Z. Kamiński, *Phys. Rev. A* **100**, 012104 (2019), 1811.07528.
- [103] A. Bechler, F. Cajiao Vélez, K. Krajewska, and J. Z. Kamiński, *Acta Phys. Polon. A* **143**, S18 (2023), 2306.07668.